Gennady L. Gutsev
Kalayu G. Belay
Lavrenty G. Gutsev
Charles A. Weatherford

Modification of Magnetic Properties of Iron Clusters by Doping and Adsorption

From a Few Atoms to Nanoclusters

Springer

SpringerBriefs in Molecular Science

Electrical and Magnetic Properties of Atoms, Molecules, and Clusters

Series editor

George Maroulis, Patras, Greece

More information about this series at http://www.springer.com/series/11647

Gennady L. Gutsev · Kalayu G. Belay
Lavrenty G. Gutsev · Charles A. Weatherford

Modification of Magnetic Properties of Iron Clusters by Doping and Adsorption

From a Few Atoms to Nanoclusters

Gennady L. Gutsev
Department of Physics
Florida A&M University
Tallahassee, FL
USA

Kalayu G. Belay
Department of Physics
Florida A&M University
Tallahassee, FL
USA

Lavrenty G. Gutsev
Department of Chemistry and Biochemistry
Florida State University
Tallahassee, FL
USA

Charles A. Weatherford
Department of Physics
Florida A&M University
Tallahassee, FL
USA

Contents

Modification of Magnetic Properties of Iron Clusters by Doping and Adsorption: From a Few Atoms to Nanoclusters

Abstract Electronic and geometrical structure of neutral and charged iron clusters Fe_n, Fe_n^-, and Fe_n^+ (n = 2–20) will be discussed. Computational results will be compared to experimental data, in particular, to the recent data obtained from the magnetic moment measurements of Fe_n^+. We consider iron cluster oxides, single Fe atom oxides FeO_n for n up to 12, and FeX_n superhalogens. We present the results of computational simulations of gas-phase interactions between small iron clusters and OH, N_2, CO, NO, O_2, and H_2O. Competition between surface chemisorption and cage formation in $Fe_{12}O_{12}$ clusters will be discussed. The magnetic quenching found in $Fe_{12}O_{12}$ will be qualitatively explained using the natural bond orbital analysis performed on Fe_2O_2. Special attention will be paid to the structural patterns of carbon chemisorbed on the surface of a ground-state Fe_{13} cluster.

1 Introduction

Iron plays an extremely important role in nature as well as in human society. In nature, it catalyzes the vital processes of photosynthesis in plants and the generation of atomic oxygen in mammals. It is hard to overestimate the role of iron in industry and we presently mention just one example. For more than a century bulk iron has been used in the production of ammonia because of its capability of breaking the triple bond in molecular N_2. With recent advances in nanoscience, special attention has been paid to applications using nanoparticles with sizes up to hundreds of nanometers and clusters whose size is smaller than 1–2 nm. Iron nanoparticles are widely used in the fabrication of memory devices and the improvement of the data capacity of such devices is related to the decreasing size of iron particles which then leads to an increasing density of data.

Iron belongs to a small group of magnetic atoms which consists of Fe, Co, Ni, Ru, and Gd. The magnetic behavior of iron clusters is rather complicated as may be demonstrated by molecular beam deflection (Stern-Gerlach) measurements for iron clusters composed of 25 to $\sim$700 atoms in the 80–1000 K temperature range [1].

All clusters are found to be ferromagnetic and the magnetic moment per atom approaches the bulk limit of 2.15 μ_B as the cluster size increases. It was further noted that there are low-spin ferrimagnetic states of Fe_n in the $20 \leq n \leq 200$ range along with the high-spin ferromagnetic states found previously [2]. The total magnetic moments of these low-spin states are $\sim n\mu_B$ whereas the total magnetic moments of the high spin states are $\sim 3n\ \mu_B$.

For smaller iron clusters in the range of $n = 10$–25, Stern-Gerlach deflection experiments have been performed and it was found that the magnetic moments show large oscillations when $n < 15$, while they are close to $3\ \mu_B$ for the larger clusters. A separation of the total magnetic moment into its spin and orbital constituents was recently done [3] for Fe_n^+ clusters ($n = 2$–20) using X-ray magnetic circular dichroism (XMCD) spectroscopy. It was found that the orbital magnetic moment amounts to 8–15 % of the total magnetic moment, i.e., the major contribution to the total magnetic moments of the clusters comes from the total spin magnetic moment.

Noncollinearity of local spin magnetic moments in iron clusters was a subject of several studies. The conclusions derived from the results of these studies are often controversial. Whereas Oda et al. [4] found non-collinear magnetic moments for Fe_3 and Fe_5 in the series Fe_n with $n = 2$–5, Hobbs et al. [5] have not found any stable non-collinear state for Fe_3. Recently, Roy et al. [6] have studied non-collinear behavior in neutral Fe_n and anionic Fe_n^- clusters with $n = 2$–8, and concluded that "while our studies predict collinear ground states for most clusters, we do find non-collinear states energetically close to the ground states in most cases." Rollmann et al. [7] performed computations of Fe_n in a wider range of $2 \leq n \leq 15$ and found that geometric distortions do restore the collinearity of the local spin magnetic moments in all cases considered. Therefore, one can anticipate that non-collinear effects are small for larger iron clusters.

Nanoparticles of iron, cobalt, and nickel are widely used as catalysts in the production of carbon nanotube with iron generally being considered the best. Carbon single-walled nanotubes (SWNT) exhibit many unique and useful physical and chemical properties. Carbon nanotube manufacturing methods include laser vaporization of metal-doped carbon electrodes, chemical vapor deposition (CVD) and HiPco (high-pressure CO) process. In the latter process, SWNTs grow from CO feedstock under high-pressure, high temperature conditions. Catalyzing iron clusters are formed in situ by thermal decomposition of iron pentacarbonyl Fe $(CO)_5$, and SWNTs are believed to nucleate and grow via the CO Boudouard disproportionation reaction.

A promising area for iron catalyst applications is production of hydrogen from water using solar energy. Proposed methods are based on the use of iron oxide surfaces and water in redox reactions such as $Fe_3O_4 \rightarrow 3FeO + 1/2O_2$ followed by $H_2O + 3FeO \rightarrow Fe_3O_4 + H_2$. Bare iron clusters appear to be promising for hydrogen production as well since [8] "the H_2O reactions with bare iron clusters are characterized by complex adsorbate decomposition and hydrogen desorption processes."

Theoretical studies of the bare 3*d*-metal clusters and their interactions with various species would help in the understanding of processes which are important for technological applications and improve our knowledge on the microscopic nature of events behind such processes. With this purpose in mind, we review recent theoretical work pertaining to bare iron clusters and their interactions with a number of *sp*-species. The results discussed below were obtained using the density functional theory with the generalized gradient approximation. Among the density functional methods, the BPW91/6-311 + G* method with a basis set of triple-ζ quality was tested against experimental data and was proven to be quite reliable. Therefore, it was used more often than other methods, and the data shown below are obtained using this method if not stated otherwise.

2 Peculiarities of the Fe–Fe Bonding

A ground-state iron atom is not reactive and has to be promoted into an excited state Fe* in order to be able to participate in chemical reactions. According to the promotion scheme displayed in Fig. 1, a 4*s*-electron is transferred into a vacant β-3*d* atomic orbital (AO) and the resulting experimental promotion energy is 0.87 eV. Two excited Fe* atoms in the ^5F states can react to form a Fe_2 dimer.

In order to gain insight into the nature of chemical bonding in the Fe_2 dimer, we use the results of Natural Bond Orbital (NBO) analysis [9] which operates in terms of natural atomic orbitals (NAO). In order to explore the dependence of chemical bonding in the Fe_2 dimer on charge, we consider also bonding patterns of negatively and positively charged Fe_2^- and Fe_2^+ ions [10]. The schemes of bonding orbitals and localized spin-orbitals (LSO) in the ground states of all three species are presented in Fig. 2. The energy scale corresponds to orbital energies obtained using the NBO NAOs. The central panels present bonding orbitals (or single-electron bonds) in both spin representations while the uttermost left and right panels show the LSOs of the "left" and "right" atoms of the neutral and charged Fe_2 dimer. Note that the energies of molecular orbitals (MO) in α- and β-spin representations are different since we are using the unrestricted Hartree-Fock (UHF) approach and;

Fig. 1 A Fe → Fe*
promotion scheme
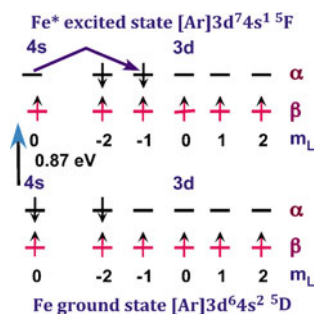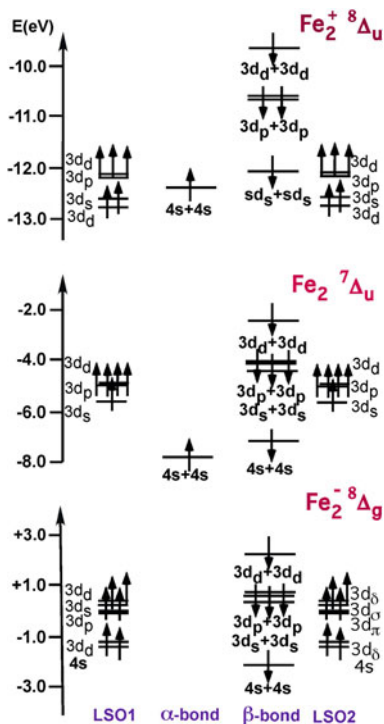
therefore, the usual notion of a chemical bond as corresponding to a bonding MO occupied by two spin-coupled electrons is unsuitable for describing bonding in the high-spin states of clusters the iron dimer in particular.

As can be seen in Fig. 2, there is a single $4s + 4s$ bonding MO in the α-spin representation in the ground states of Fe_2 and Fe_2^+ and no α-bonds at all in the Fe_2^- anion, whereas all α-$3d$ AOs of both Fe atoms are chemically inert. These AOs occupy LSOs which are formed if the bonding $3d_m + 3d_m$ and antibonding $3d_m - 3d_m$ MOs ($m = -2, -1, 0, 1, 2$) of the dimer are occupied. In the case of the β-spin representation, there are a number of single bonds which are formed from two β-$3d$ AOs of each iron atom. In a sense, only the $4s + 4s$ bonding orbital occupied by two electrons corresponds to a classical chemical bond. Both attachment and detachment of an electron affects this bond. Detachment of an electron results in the hybridization of $4s$ and $3d_0$ AOs whereas the attachment of an electron to an antibonding $4s - 4s$ MO results in the addition of one $4s$ LSO on each atom. The inertness of $3d$ AOs in the α-spin representation is the major source of the following magnetic phenomena in iron clusters: ferromagnetism, ferrimagnetism, and antiferromagnetism. The total spin is defined mainly by the difference between the number of α-LSOs and the number of single bonds in the β-spin representation. The main trends in the structures of small neutral and singly charged iron clusters have been found [11] to be quite similar to those of the iron dimer. The neutral Fe

atom has the spin multiplicity $2S + 1$ of 5 which corresponds to a total spin of 2. One can expect the total spin of a Fe$_n$ cluster to be about 2 times n if the α-$3d$ subshells are chemically inert in the clusters. However, the total spins of the lowest total energy states of Fe$_n$ clusters with $n = 2$–6 were found to be 3, 5, 7, 8, and 10, respectively, which are somewhat different from the expected values of 4, 6, 8, 10, and 12.

The reason for the decrease in the total spin is related to redistributions of $4s$ electrons between two spin representations. For example, the effective electronic configuration of a Fe atom in Fe$_6$ cluster in its ground state with a nearly octahedral geometrical configuration is $3d^{6.86}4s^{1.03}4p^{0.06}$, as obtained from the NBO analysis. This electronic configuration is close to that of a free-standing atom in its excited state (see Fig. 1). This configuration splits into its spin-components $3d^{4.98}4s^{0.65}4p^{0.02}$ (α) and $3d^{1.88}4s^{0.39}4p^{0.04}$ (β). That is, the contribution to the total spin moment from spins of electrons occupying $3d$ AOs of each atom of the cluster are nearly the same as of that in a free standing iron atom, whereas contributions from electrons occupying $4s$ AOs are reduced to 0.26 e per atom because $4s$ electrons participate in bonding in both spin representations. Note that the promotion to vacant $4p$ orbitals in small Fe clusters is negligible. This can be related to two major factors: (1) availability of bonding $4s$-based MOs and (2) the costly promotion to virtual $4p$ states. When the number of atoms increases, the availability of bonding $4s$-based MOs decreases whereas the energy required for the $4s \rightarrow 4p$ promotions is compensated by the energy gained due to formation of bonding orbitals consisting of $4p$ AOs. Since the bonding orbitals possess many-center character, one should use special techniques, such as the electron localization function to describe the bonding patterns in iron clusters [12].

The total magnetic moment is defined in the Russell-Saunders scheme as $\boldsymbol{\mu} = (\mathbf{L} + 2\mathbf{S})\,\mu_B$, where μ_B is the Bohr magneton, and $\mathbf{L}$ and $\mathbf{S}$ are the total angular and spin moments, respectively. The value of the total spin magnetic moment, $M = 2S\,\mu_B$, is computed as $[N_\alpha - N_\beta]\,\mu_B$, where N_α and N_β are the numbers of the majority spin and minority spin electrons, respectively. The local spin magnetic moments on atoms are considered to be equal to the excess spin densities obtained using the NAO populations. The total spin magnetic moment of a Fe atom is 4 μ_B and it is reduced to a local spin magnetic moment of 3 μ_B per Fe atom in the ground-state Fe$_2$ dimer. The latter total spin magnetic moment per iron atom is appreciably higher than the total magnetic moment in iron bulk which is 2.15 μ_B per atom.

3 Oxides and Superhalogens with a Single Fe Center

Since the formal valence of a Fe atom is seven, the atom can attach up to 4 separated oxygen atoms because oxygen atoms are divalent. Oxidation reduces [13] the total spin magnetic moment of FeO$_n$ species from 4 μ_B in FeO to 0 μ_B in FeO$_4$. This reduction in the moment value is related with the involvement of 3d electrons in chemical bonding in *both* spin representations. In the case of *sp*-compounds,

singlet states usually possess small electron affinities because their valence shells are saturated. This is not the case for FeO_4. Since its electron affinity (3.9 eV) exceeds the largest atomic electron affinity of elements in the Periodic Table, that of a Cl atom (3.6 eV), FeO_4 can thus be attributed [14] to the class of superhalogens. Formally, CO can be considered divalent if one assumes that C is tetravalent; however, FeCO in its ground $^3\Sigma^-$ state has [15] a total spin magnetic moment of $2~\mu_B$. When one compares this value with the value obtained for FeO, one can conclude that a total spin magnetic moment of FeX_n species depends not simply on the valence of the X ligand.
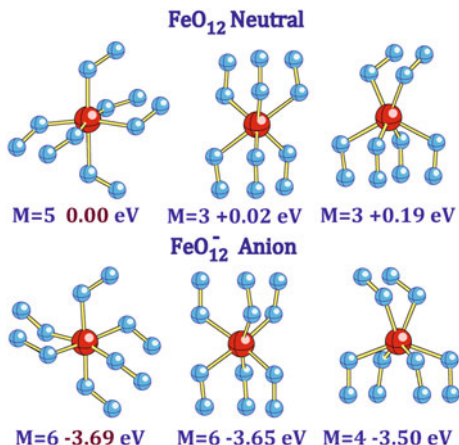
There are three forms of interactions of O_2 with a Fe atom: dissociative (oxo), side-on (peroxo), and end-on (superoxo) attachments. Judging by the valence of the atoms, four oxygen atoms can be attached to a Fe atom in the oxo form; however, it is not clear how many O_2 can be attached to a Fe atom in these three forms. The different forms of oxygen attachment to a Fe atom can be seen in Fig. 3 where geometrically stable isomers of FeO_5 and FeO_7 are shown. As can be seen, the number of possible topologies including the ones with the ozone-type oxygen arrangement increases rapidly and reaches [16] a maximum at $n = 8$ after which it decreases as n grows.

Total spin magnetic moments of the lowest total energy states of FeO_n are quenched for $n = 4, 5, 6, 7$ and 8. The largest number of oxygen atoms that can be attached to Fe in the peroxo form is 12 (see Fig. 4), which was experimentally confirmed later [17]. Both $Fe(O_2)_6$ and $Fe(O_2)_6^-$ (see Fig. 4) are geometrically stable and are also stable with respect to the loss of an oxygen atom. The total spin magnetic moment of the lowest total energy state of $Fe(O_2)_6$ is $4~\mu_B$, i.e., it is the same as the total spin magnetic moment of an Fe atom. The adiabatic electron affinity (EA_{ad}) of all FeO_n for $n > 3$ are somewhat larger than the EA of a chlorine atoms; therefore, all of these iron oxides are superhalogens.

Fig. 3 Isomers of FeO_5 and FeO_7; total energies are given with respect to the total energy of the corresponding ground state and M denotes the spin multiplicity $2S + 1$
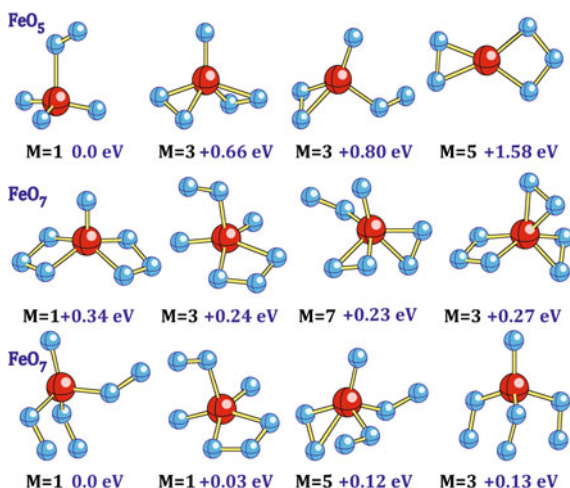
Fig. 4 Isomers of FeO$_{12}$ and FeO$_{12}^-$; total energies are given with respect to the total energy of the corresponding ground state and M denotes the spin multiplicity $2S + 1$

FeO$_{12}$ Neutral

M=5 0.00 eV   M=3 +0.02 eV   M=3 +0.19 eV

FeO$_{12}^-$ Anion

M=6 -3.69 eV   M=6 -3.65 eV   M=4 -3.50 eV

Since most of our computations are performed using density functional theory (DFT) within the unrestricted Hartree-Fock (UHF) approach, a natural question arises about spin contamination of wavefunctions obtained from such computations. The spin contamination is defined by the deviation of the total spin angular momentum expectation value $<S^2>$ from the exact value of $S(S + 1)$. S^2 is a two-particle property and is defined for a N-electron system as

$$<S^2> \ = \frac{N(N-4)}{4} + \int \Gamma(\mathbf{r}_1 s_1, \mathbf{r}_2 s_2 | \mathbf{r}_1 s_2, \mathbf{r}_2 s_1) d\mathbf{x}_1 d\mathbf{x}_2 \qquad (1)$$

where $\mathbf{x_i} = (\mathbf{r}_i, \sigma_i)$ is the combined spatial $\mathbf{r}_i$ and spin σ_i coordinate of electron i and $\Gamma(\mathbf{x}_1', \mathbf{x}_2' | \mathbf{x}_1, \mathbf{x}_2)$ is the two-particle density matrix normalized to $N(N-1)/2$

$$\Gamma(\mathbf{x}'_1, \mathbf{x}'_2 | \mathbf{x}_1, \mathbf{x}_2) \ = \frac{N(N-1)}{2} \int \Psi(\mathbf{x}'_1, \ldots, \mathbf{x}'_N | \mathbf{x}_1, \ldots, \mathbf{x}_N) d\mathbf{x}_3 \ldots d\mathbf{x}_N \qquad (2)$$

This two-particle density matrix can be expanded in terms of one-particle density matrices as

$$\Gamma(\mathbf{x}'_1, \mathbf{x}'_2 | \mathbf{x}_1, \mathbf{x}_2) = [\gamma(\mathbf{x}'_1 | \mathbf{x}_1) \gamma(\mathbf{x}'_2 | \mathbf{x}_2) - \gamma(\mathbf{x}'_1 | \mathbf{x}_2) \gamma(\mathbf{x}'_2 | \mathbf{x}_1)] + \Im(\mathbf{x}'_1, \mathbf{x}'_2 | \mathbf{x}_1, \mathbf{x}_2) \qquad (3)$$

where $\Im(\mathbf{x}'_1, \mathbf{x}'_2 | \mathbf{x}_1, \mathbf{x}_2)$ is an unknown modification term.

Density functional theory operates with one-particle electronic densities built from Kohn-Sham (KS) orbitals. These KS orbitals can be used for constructing an unrestricted (UKS) determinant wave function by analogy with a UHF wave function. However, such a UKS wave function corresponds to a fictitious

non-interacting system with the same charge density not a real interacting system. Therefore, the determination of $<S^2>$ using UKS determinant wave functions may not reflect the true spin contamination. Several models of estimating the $\mathfrak{I}$ contribution from Eq. (3) have been discussed and applied for atoms and diatomic molecules. This is a very difficult problem, since it is practically equivalent to the unsolved problem of a wave function reconstruction from known electronic densities.

In most *sp*-systems, the spin contamination computed from UKS determinants is usually rather small. As concerns FeO_{12}, which possesses geometrically stable isomers up to $2S + 1 = 13$, the state with $2S + 1 = 13$ has $<S^2> = 42.027$ and its projection is $<S^2>A = 42.000$ which matches the exact value of $S(S + 1) = 42$. A state with $2S + 1 = 7$ has $<S^2> = 13.375$ and a projection of $<S^2>A = 12.560$ which can be compared to the exact value of 12. That is, there is a significant difference when compared to the previous high-spin case. The Mulliken population analysis shows that all local spin densities are coupled parallel in the $2S + 1 = 13$ state, while the excess spin density at Fe is coupled antiparallel to the excess spin densities at oxygen atoms in the $2S + 1 = 7$ state. The deviation of $<S^2>$ from the exact value is the largest in a singlet state where $<S^2> = 3.588$ (the exact value is 0) and the projection makes it even worse $<S^2>A = 12.264$, which is in accordance with Wittbrodt and Schlegel's warning [18] which stated that the spin projection of UKS determinant wave functions can yield poor results.

A fluorine atom has the valence electron configuration of $2s^2 2p^5$ and is the most electronegative atom in the Periodic Table. One could expect, by analogy with the oxidation of a Fe atom, that the total spin magnetic moment of FeF_n will decrease as n increases and one would thus expect FeF_7 to be a singlet; however, no such behavior follows from the results [19] of DFT computations presented in Fig. 5. As shown in the figure, the spin multiplicities of states in both the neutral and anion series remains high up to $n = 6$. It is interesting that the spin multiplicity of FeF is higher by one that that of a free-standing Fe atom, which is related with the transfer of a Fe $3d$ electron (see Fig. 1) to the F atom to make its valence shell closed.

In order to gain insight as to why FeF_6 has a total spin magnetic moment of 4 μ_B let us consider the FeF_6 neutral species whose ground state is ^5A_g with a Jahn-Teller distorted octahedral geometry of C_i symmetry. According to the NBO analysis, the total spin magnetic moment of the Fe atom is 2.07 μ_B, which is the difference in populations in the α ($3d^{4.08} 4s^{0.14} 4p^{0.02}$) and β ($3d^{2.03} 4s^{0.14}$) spin representations, and each F atom carries the total spin magnetic moment of 0.32 μ_B which is due to donation and back-donation contributions. The EA_{ad} values of FeF_4, FeF_5, and FeF_6 computed using different DFT and hybrid HF-DFT methods are 6.1–6.5, 6.7–7.1, and 7.5–7.8 eV, respectively; therefore, all of them are superhalogens. Taking into account that all of these species carry the total spin magnetic moments of 3 μ_B (FeF_5) or 4 μ_B (FeF_4 and FeF_6), these neutrals are magnetic superhalogens.

**Fig. 5** Ground states of FeF_n and FeF_n^- for $n = 1$–6. Bond lengths are in ångströms
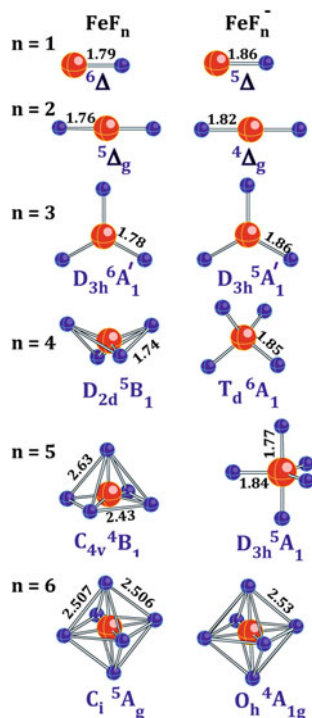
4 Interactions of Small Iron Clusters with C and O Atoms

The structures and total spin magnetic moments of neutral and singly positively and negatively charged Fe_n ($n = 2$–6) clusters have been studied [20] using both DFT and HF-DFT methods and the results were found to be in good agreement with experimental data. The geometrical structures of lowest total energy states found for these clusters are shown in Fig. 6.

As can be observed in the figure, the total spin increases from $S = 3$ in Fe_2 to 10 in Fe_6. Also, the Fe_{n-1}–Fe_n spin increments are 2 for all pairs except for the Fe_4–Fe_5 pair, where it increases by one, i.e., it is smaller than the total spin $S = 2$ which is expected when a Fe atom added. However, the spin dependence is small in this cases and the Fe_5 states with $2S = 14$ and $2S = 16$ as well as the Fe_6 states with $2S = 21$ and $2S = 23$ are nearly degenerate in total energy.

The attachment and detachment of an electron to/from a Fe_n cluster is mainly of the one-electron type, i.e., when the spin of a final state is different from that of the initial state by the spin of an electron. According to Fig. 6, the only exception is Fe_4^+, whose total spin is smaller than that of its neutral parent by 3/2. The results of computations on adiabatic electron affinities and ionization energies as well as experimental data are presented in Table 1. Agreement with the experimental EA_{ad}

Fig. 6 Ground states of Fe_n^+, Fe_n and Fe_n^- for $n = 2$–6. Bond lengths are in Å and local spin magnetic moments are in μ_B
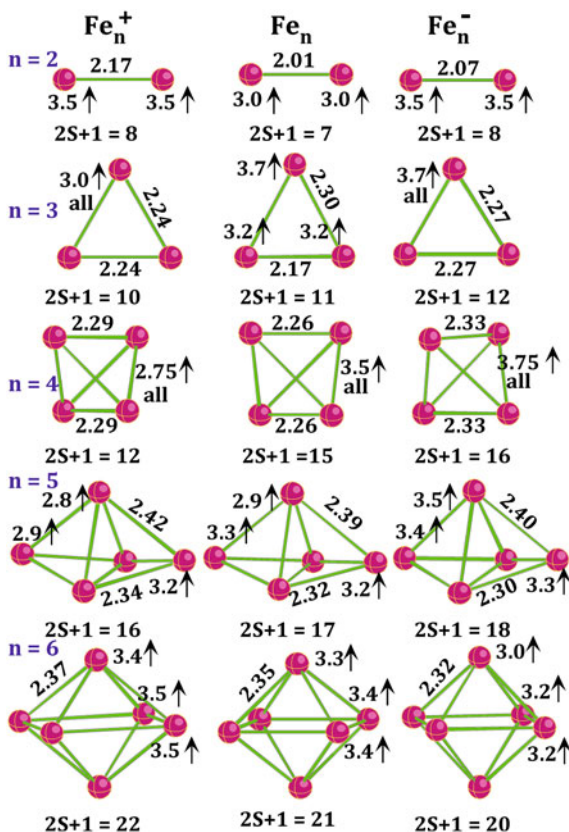
Table 1 Comparison of theoretical and experimental electron affinities and ionization energies of iron clusters

		Fe_2	Fe_3	Fe_4	Fe_5	Fe_6
EA_{ad}, eV	Theory	0.94	1.47	1.76	1.84	1.61
	Expl[a]	0.902 ± 0.008	1.47 ± 0.08	1.72 ± 0.08	1.81 ± 0.08	1.51 ± 0.08
IE_{ad}, eV	Theory	6.68	5.82	5.71	6.04	6.15
	Expl[b]	6.3 ± 0.1	6.45 ± 0.05	6.4 ± 0.1	5.95 ± 0.05	5.9 ± 0.1

All values are in eV
[a]See Ref. [21]
[b]See Ref. [22]

values is very good, but is somewhat worse for the experimental adiabatic ionization energies (IE_{ad}) which tend to be less reliable than the experimental EA_{ad} values.

We begin the study of interactions of iron clusters and *sp*-atoms carbon. Geometrical structures of the lowest total energy states found [23] for the Fe_nC clusters ($n = 1$–6) along with their ions are presented in Fig. 7. The attachment of a

Fig. 7 Ground states of Fe$_n$C$^+$, Fe$_n$C and Fe$_n$C$^-$ for $n = 1$–6. Bond lengths are in Å and local spin magnetic moments are in μ_B. Local spin magnetic moments whose magnitude is smaller than 0.1 μ_B are not shown
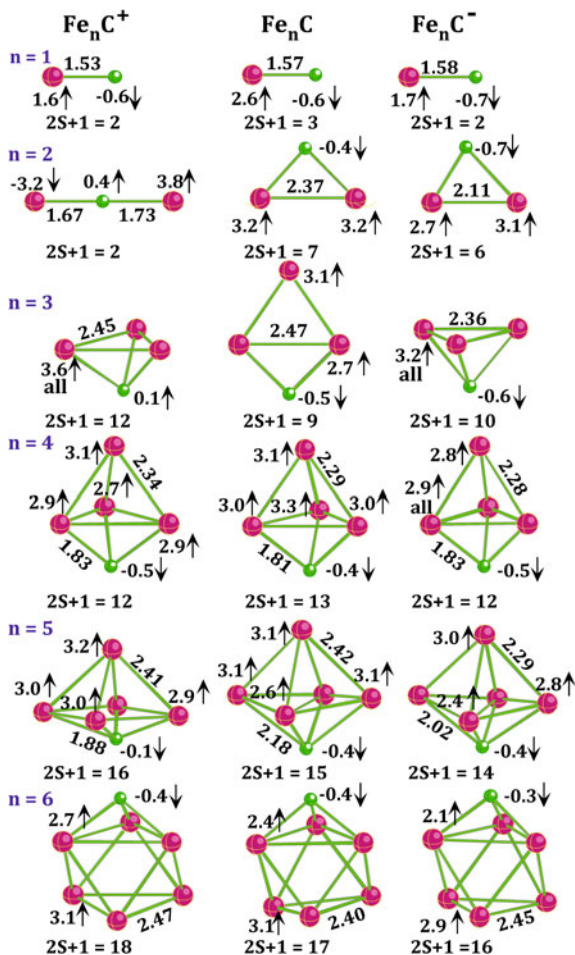
carbon atom to a Fe atom quenches the total spin magnetic moment of the Fe atom by 3 μ_B. The ground states of FeC$^+$, FeC, and FeC$^-$ have the Fe and C total spins antiferromagnetically coupled due to spin polarization (asymmetric bonding in spin-up and spin-down representations). The number of unpaired electrons of the neutral and charged ground states differ by one, thus satisfying the empirical "±1 rule" which corresponds to an assumption that detachment and attachment of an electron from/to a ground-state neutral are one-electron processes. The total spin magnetic moment of Fe$_2$C is unquenched with respect to that of Fe$_2$, whereas the total spin magnetic moment of Fe$_2$C$^-$ is quenched by 2 μ_B with respect to that of Fe$_2^-$. The largest quenching is found for Fe$_2$C$^+$, whose total magnetic moment vanishes and its ground state is a ferrimagnetic doublet. This state of the Fe$_2$C$^+$ cation presents an interesting case of superexchange spin coupling in bridged transition metal compounds. In order to understand its nature, let us resort to a description of its

electronic structure in terms of the NBO analysis. The NAO electronic configurations of atoms in Fe_2C^+ have different spin-up and spin-down constituents:

$$\text{spin-up } (\alpha) : C\left(2s^{0.85}2p^{1.63}\right),\ Fe_1\left(4s^{0.04}3d^{2.30}\right),\ Fe_2\left(4s^{0.34}3d^{4.82}\right)$$
$$\text{spin-down } (\beta) : C\left(2s^{0.87}2p^{1.25}\right),\ Fe_1\left(4s^{0.27}3d^{4.70}\right),\ Fe_2\left(4s^{0.05}3d^{1.86}\right)$$

The NBO analysis suggests that the superexchange coupling in Fe_2C^+ is related to the specific bonding pattern of Fe_1–C–Fe_2; the half-filled 3d-shells of both iron atoms are localized and coupled antiparallel to each other, meanwhile the π-bonding orbitals undergo a strong spin polarization such that those in one spin representation are between the carbon and first Fe while those in the other spin representation are between the carbon and the second Fe atom. In the neutral case, such a singlet state also has a similar electronic configuration with oppositely aligned local spin magnetic moments on Fe atoms of $\pm 3.4\ \mu_B$, but this state is above the ground state by 0.47 eV.

A carbon atom attachment to an iron cluster does not change the iron cluster topology and C atoms are three coordinate in all cases except for Fe_3C. The attachment always leads to the decrease in a total spin magnetic moment with respect to the total spin magnetic moment of the initial iron cluster. For example, the decrease in the total spin magnetic moment of the Fe_6C series is $4\ \mu_B$ independent of the cluster charge.

As concerns binding energies in the neutral Fe_nC clusters, it was found that the C–Fe_n binding energies are almost as twice as large as the Fe–$Fe_{n-1}C$ binding energies. The latter energies are higher by 0.2–0.5 eV than the corresponding Fe–Fe_{n-1} binding energies; that is, an addition of a carbon atom to an iron cluster leads to the strengthening of all bonds in the cluster. Attachment and detachment of an electron appreciably modify the binding energies of the smaller species, whereas the change in binding energies due to attachment or detachment of an electron in larger clusters (such as Fe_5C and Fe_6C) is smaller.

When considering interactions of oxygen with small iron atoms, it is convenient to start with a discussion on the similarities and differences in the structure of iron monocarbides and monoxides [24]. The ground states of FeO^+, FeO, and FeO^- are $^6\Sigma^+$, $^5\Delta$, and $^4\Delta$, respectively, whereas the ground states of FeC^+, FeC, and FeC^- are $^2\Delta$, $^3\Delta$, and $^2\Delta$, respectively. All ground states in the FeO series are ferromagnetic, while they are ferrimagnetic in the FeC series. Comparing these two series, one can conclude that the change in the total spin magnetic moment of a single Fe atom depends strongly on the nature of the atom attached.

Geometrical and electronic structures of neutral and anionic Fe_nO clusters have been studied [25] both experimentally and theoretically for $n = 2$–6, and the optimized geometrical structures are shown in Fig. 8. Comparison of Figs. 6 and 8 shows that the total spin magnetic moments $2S\ \mu_B$ are the same for each n value in both the neutral Fe_n and Fe_nO species, the sole exception being the neutral Fe_4–Fe_4O pair. This is in sharp contrast with the previous case of a carbon atom attachment to the Fe_n clusters of the corresponding size where the total spin

Fig. 8 Ground states of Fe_nO and Fe_nO^- for $n = 2$–6. Bond lengths are in Å and local spin magnetic moments are in μ_B
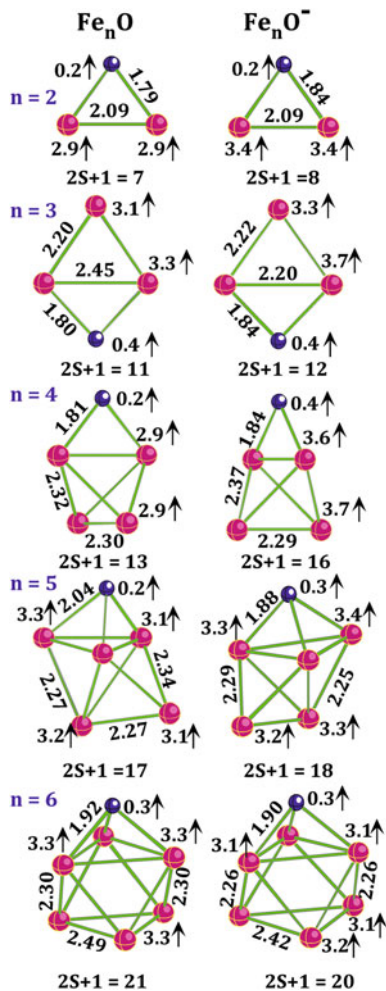
magnetic moments of the iron clusters are quenched, due to carbon atom chemisorption, by as much as 4 μ_B (see Fig. 7). It is worth noting that the BPW91 method used in our calculations on iron oxides demonstrates good performance which can be seen in Table 2.

The Fe_n–O binding energies were found to be much higher than the Fe_{n-1}–Fe binding energies, although they are somewhat smaller than the Fe_n–C binding

Table 2 Comparison of the experimental and theoretical EA_{ad} (in eV) of iron cluster monoxides

	FeO	Fe_2O	Fe_3O	Fe_4O	Fe_5O	Fe_6O
Theory	1.26	1.30	1.34	1.60	1.63	1.53
Experiment	1.50 ± 0.02	1.60 ± 0.02	1.44 ± 0.02	1.70 ± 0.02	1.85 ± 0.02	1.70 ± 0.02

Table 3 Binding energies (in eV) of neutral and negatively charged Fe_6, Fe_6C, and Fe_6O clusters

Neutral		Anion	
Channel	Theory	Channel	Theory
$Fe_6 \rightarrow Fe_5 + Fe$	3.74	$Fe_6^- \rightarrow Fe_5^- + Fe$	3.51
$Fe_6C \rightarrow Fe_5C + Fe$	3.26	$Fe_6C^- \rightarrow Fe_5C^- + Fe$	3.02
$Fe_6O \rightarrow Fe_5O + Fe$	3.64	$Fe_6O^- \rightarrow Fe_5O^- + Fe$	3.54
$Fe_6O \rightarrow Fe_6 + O$	5.70	$Fe_6O^- \rightarrow Fe_6^- + O$	5.67
$Fe_6C \rightarrow Fe_6 + C$	6.51	$Fe_6C^- \rightarrow Fe_6^- + C$	6.11

energies for a given n. In order to show the difference in binding energies of Fe, C and O atoms, we present the results obtained for the Fe_6 and Fe_6^- clusters and their monocarbides and monoxides (see Table 3).

5 Interactions of Small Iron Clusters with OH, NO, CO, and H₂O

Fe$_n$ + OH. Both experimental and theoretical studies have shown that water readily dissociates on iron surfaces and produces hydroxyl species on the surface even at low water exposure. The hydroxyl anion OH^- is believed to play the central role in aqueous corrosion of iron and other $3d$-metals. This anion can also serve as a charge carrier in batteries and fuel cells. Several corrosion mechanisms were proposed, one of which is described by the following set reactions:

$$Fe + OH^- \Leftrightarrow Fe(OH)_{ads} + e^-$$
$$Fe(OH)_{ads} + OH^- \Leftrightarrow FeO_{ads} + H_2O + e^-$$
$$FeO_{ads} + OH^- \Leftrightarrow HFeO_2^-$$
$$HFeO_2^- + H_2O \Leftrightarrow Fe(OH)_2 + OH^-$$
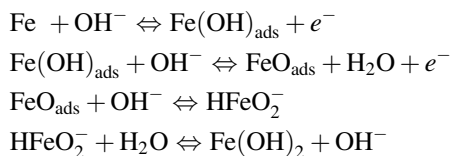
In order to gain insight into the interaction of OH with iron particles Fe_n, we consider the results of computations performed [26] for neutral and charged clusters: Fe_nOH, Fe_nOH^-, and Fe_nOH^+ ($n = 1$–4), where OH is attached either associatively or dissociatively. The optimized lowest total energy states in all three series are presented in Fig. 9. As can be seen, except for a few cases, the OH attachment is dissociative, and depends on the cluster charge. In the $n = 3$ series, OH is attached associatively in the Fe_3OH^+ cluster, whereas, in the $n = 4$ series, it is attached associatively in the Fe_4OH^- cluster. The dissociative OFe_nH structure is expected to be favored with increasing size of the iron cluster because of the increasing contribution of the Fe atoms to the chemical bonding with chemisorbed O and H atoms.

Fig. 9 Ground states of Fe$_n$OH$^+$, Fe$_n$OH, and Fe$_n$OH$^-$ (n = 1–4). Bond lengths are in Å and local spin magnetic moments are in μ_B
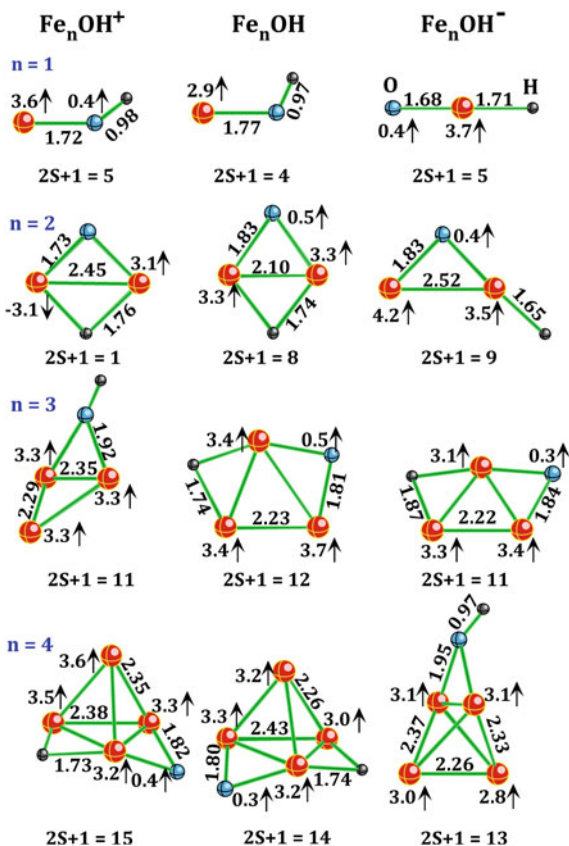
Our computed fragmentation energies of ground-state Fe$_n$OH and their ions are presented in Table 4. Experimental values of D$_0$(Fe–OH) = 3.33 ± 0.17 eV and D$_0$(Fe$^+$–OH) = 3.73 ± 0.10 eV compare quite well to our values of 3.53 and 3.98 eV, respectively. As can be seen in Table 4, the lowest energy decay channel corresponds to the loss of an H atom independent of charge when n > 2. Binding energies of OH and OH$^-$ are rather high, being about 4.5 eV in Fe$_3$OH and Fe$_4$OH and about 4.2 eV in Fe$_3$OH$^-$ and Fe$_4$OH$^-$, and the binding energies of O are similar to those in Fe$_n$O being around 5.5–6.5 eV.

Table 4 Fragmentation energies (D$_0$, eV) of Fe$_n$OH, Fe$_n$OH$^-$, and Fe$_n$OH$^+$

Neutral	D$_0$	Anion	D$_0$	Cation	D$_0$
FeOH → Fe + OH	3.53[a]	FeOH$^-$ → Fe + OH$^-$	2.97	FeOH$^+$→Fe$^+$ + OH	3.98[a]
OFe₂H → Fe + FeOH	2.53	OFe₂H$^-$ → Fe + FeOH$^-$	2.70	OFe₂H$^+$→ Fe₂O$^+$ + H	2.73
OFe₃H → Fe₃O + H	2.70	OFe₃H$^-$ → Fe₃O$^-$ + H	2.87	Fe₃OH$^+$→ Fe₃O$^+$ + H	2.92
OFe₄H → Fe₄O + H	2.94	OFe₄H$^-$ → Fe₄O$^-$ + H	2.89	Fe₄OH$^+$→ Fe₄O$^+$ + H	2.74

[a]Experiment: D$_0$(Fe–OH) = 3.33 ± 0.17 eV and D$_0$(Fe$^+$–OH) = 3.73 ± 0.10 eV

Fe_n + NO. The interaction of nitrogen monoxide with surfaces and clusters of *d*-metals has been intensively studied because NO is involved in many technologically important processes, such as ammonia oxidation and emissions control. Of special interest to environmental chemistry is the reduction of NO (a major atmospheric pollutant) by CO, as exemplified by the reaction

$$NO + CO \rightarrow 1/2N_2 + CO_2 \tag{4}$$
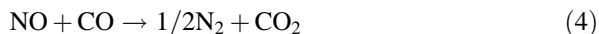
Such a reduction is accomplished in car exhausts using three-way catalysts composed of Rh, Pd, and Pt. Iron is a very good catalyst; therefore, one can expect that iron clusters can also catalyze reaction (4).

By analogy with the previous case, we consider associative and dissociative attachment of NO to the neutral and charged Fe_n clusters in the range of $1 \leq n \leq 6$. Optimized geometrical structures of the lowest total energy states found are presented in Fig. 10. As can be seen, NO dissociates on an iron cluster independent of the cluster size and charge. The states whose geometrical structures correspond to the associative attachment of NO are geometrically stable and are appreciably higher in total energy than the states with the dissociative attachment. For example, the most stable states of Fe_5NO and Fe_6NO isomers are above the ground state of OFe_5N and OFe_6N by 1.85 and 2.13 eV, respectively. Dissociative attachment of NO always quenches the total spin magnetic moment of the iron clusters independent of charge. Moreover, more than half of the states presented in Fig. 10 are ferrimagnetic (these states are marked as "AF" in the figure to indicate that there are flips of total local spin magnetic moments).

The lowest energy dissociation channels of the Fe_nNO and its ions are presented in Table 5. These channels correspond to the abstraction of a neutral Fe atom except for the $OFeN^-$, $FeNO^+$, OFe_2N^+, and OFe_3N^+ species whose dissociations yield the NO radical (dissociation of FeNO produces both Fe and NO). This means that the N and O atoms are bound more strongly to each other in these cases. Note that the binding energy of the Fe atom generally increases as the cluster size grows.

Fe_n + CO. Iron clusters are known to catalyze the growth of multi- and single-walled carbon nanotubes (SWNT). Using a gas-phase reactor, Smalley with coworkers [27] have fabricated SWNTs of different diameters from $Fe(CO)_5$ in the presence of a CO flow. Under high-pressure, high-temperature conditions $Fe(CO)_5$ decomposes and forms iron clusters which serve as catalytic centers. The usage of CO as feedstock appears to be related to the reactions $M–CO + CO \rightarrow M–C + CO_2$ (where M is a catalyst cluster) which is analogical to the Boudouard disproportionation reaction of producing atomic carbon from vibrationally excited carbon monoxide $CO(v) + CO(w) \rightarrow C + CO_2$. However, the kinetics of iron-catalyzed growth of SWNTs is rather complicated and reaction mechanisms are not well understood.

In order to understand why CO, possessing the bond strength of 11.1 eV, can be used as feedstock we estimated [28] the energetics of the Boudouard-like disproportionation reactions $Fe_nCO + CO \rightarrow Fe_nC + CO_2$, $Fe_nCO^- + CO \rightarrow Fe_nC^- + CO_2$, and $Fe_nCO^+ + CO \rightarrow Fe_nC^+ + CO_2$ (n = 2–6). We optimized the geometrical

Fig. 10 Ground states of Fe_nNO^+, Fe_nNO, and Fe_nNO^-, ($n = 1$–6). Bond lengths are in Å and local spin magnetic moments are in μ_B
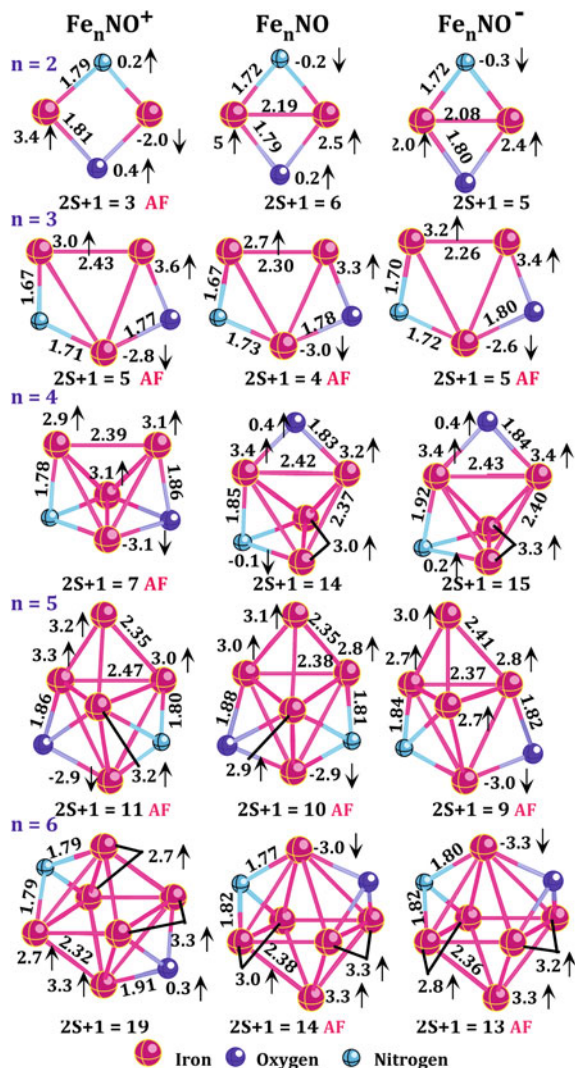
structures and spin multiplicities for the neutral and singly charged Fe_nCO for $n = 2$–6, shown in Fig. 11.

As can be seen in Fig. 11, the CO attachment is associative and does not generally change the spin multiplicities of bare iron clusters. The energies of the Boudouard-like disproportionation reactions are presented in Table 6. A plus sign indicates the reaction is endothermic. As can be seen, the effectiveness of iron clusters grows rapidly with n, and already Fe_4 shows a slight exothermicity which remains nearly constant for larger Fe_5 and Fe_6. The cationic channel $Fe_6CO^+ + CO \rightarrow Fe_6C^+ + CO_2$ has the highest exothermicity among all the

Table 5 Fragmentation energies (D_0, eV) of FeNO, FeNO$^+$ and neutral and charged OFe$_n$N

Neutral		Anion		Cation	
Channel	D_0	Channel	D_0	Channel	D_0
FeNO → Fe + NO	2.31	OFeN$^-$ → Fe$^-$ + NO	3.75	FeNO$^+$ → Fe$^+$ + NO	2.90
OFe$_2$N → FeNO + Fe	3.33	OFe$_2$N$^-$ → NFeO$^-$ + Fe	2.74	OFe$_2$N$^+$ → Fe$_2^+$ + NO	2.70
OFe$_3$N → OFe$_2$N + Fe	3.38	OFe$_3$N$^-$ → OFe$_2$N$^-$ + Fe	3.66	OFe$_3$N$^+$ → Fe$_3^+$ + NO	3.49
OFe$_4$N → OFe$_3$N + Fe	3.21	OFe$_4$N$^-$ → OFe$_3$N$^-$ + Fe	3.08	OFe$_4$N$^+$ → OFe$_3$N$^+$+Fe	3.66
OFe$_5$N → OFe$_4$N + Fe	3.16	OFe$_5$N$^-$ → OFe$_4$N$^-$ + Fe	3.22	OFe$_5$N$^+$ → OFe$_4$N$^+$ + Fe	3.49
OFe$_6$N → OFe$_5$N + Fe	3.59	OFe$_6$N$^-$ → OFe$_5$N$^-$ + Fe	3.50	OFe$_6$N$^+$ → OFe$_5$N$^+$ + Fe	3.89

Fig. 11 Ground states of Fe$_n$CO$^+$, Fe$_n$CO, and Fe$_n$CO$^-$, (n = 2–6). Bond lengths are in Å and local spin magnetic moments are in μ_B
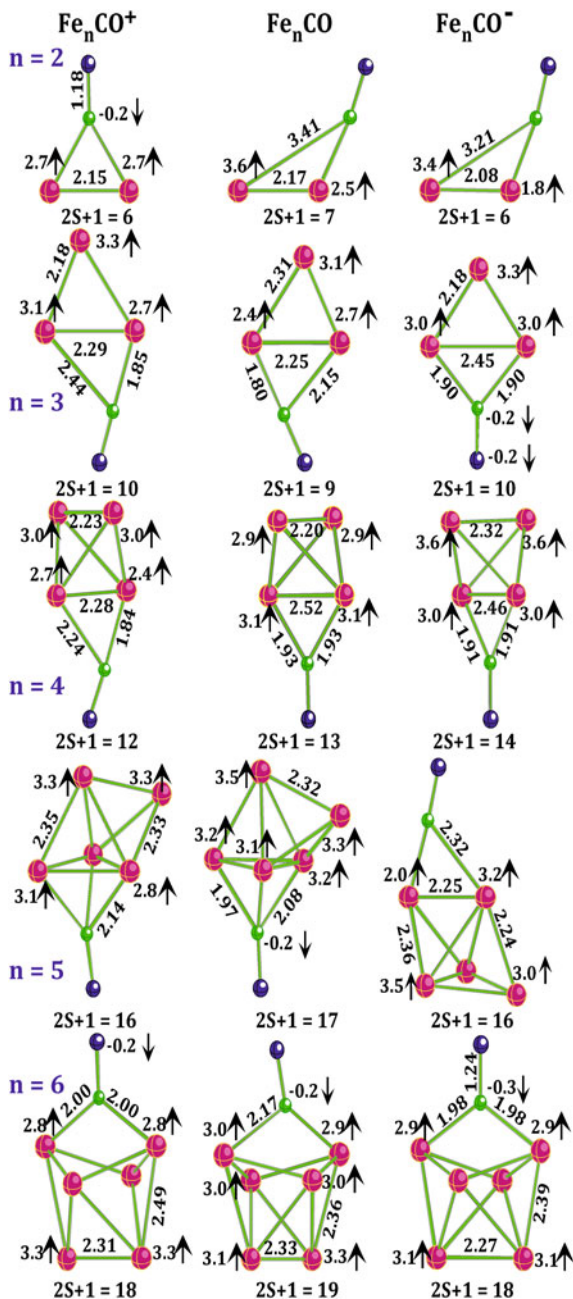
channels considered, while anionic channels are less favorable due to the fact that the electron affinities of Fe$_n$CO clusters are larger than those of Fe$_n$C, thus stabilizing the reactants relative to the products.

Table 6 Energetics of the $Fe_nCO + CO \rightarrow Fe_nC + CO_2$ neutral and ionic channels

| n	Neutral $Fe_nCO + CO \rightarrow Fe_nC + CO_2$	Anion $Fe_nCO^- + CO \rightarrow Fe_nC^- + CO_2$	Cation $Fe_nCO^+ + CO \rightarrow Fe_nC^+ + CO_2$
1	+1.59	+1.52	+2.40
2	+1.10	+1.01	+0.88
3	+0.55	+0.59	+0.79
4	−0.08	+0.58	+0.34
5	+0.12	+0.21	−0.11
6	−0.08	+0.52	−0.42

All values are in eV

Since the Fe_n–CO binding energies are relatively independent of the cluster size, the change in reaction energy with cluster size is due to the change in the Fe_nC–O bond. The Fe_nC–O bond energies are much smaller than that of free CO because the carbon atom forms a strong bond with the iron clusters. Unlike the Fe_n–CO bond energies, which are relatively independent of the cluster size, there is a decrease in the Fe_nC–O bond strength from $n = 1$ to $n = 4$, and then it gradually varies from $n = 4$ to $n = 6$. Another way to look at the weakening of the Fe_nC–O bond is as that of the strengthening of the Fe_n–C bonds which is supported by experimental results for the Fe_n–C$^+$ species.

Whereas the reaction energies are of interest, the barrier heights are critical in evaluating the reaction rates; therefore, we have determined the transition state for the $FeCO + CO \rightarrow FeC + CO_2$ and $Fe_4CO + CO \rightarrow Fe_4C + CO_2$ reactions. Figure 12 shows the geometries of the transition states found along with energetics of the corresponding reaction channels. The FeC⋯OCO transition state is a planar $^3A'$ state, while transition state of Fe_4C⋯OCO ($2S = 13$) has no symmetry. The barrier is significantly reduced when the number of iron atoms increases from one to four, as shown in Fig. 12, namely, from 3.5 to 1.3 eV.

It follows from Fig. 12, that an iron cluster serves as the third body for the Boudouard reaction and the CO dissociation is due to the relatively strong Fe_n–C and O–CO bonds.

By analogy with reaction (4), let us consider this and similar reactions which can take place in the presence of a Fe_n catalyst. In particular, it is interesting to estimate the energetics of different fragmentation channels which lead to the formation of CO_2, NCO, N_2O, and NO_2 products. Some results obtained for the neutral species are presented in Table 7. The most exothermic channel corresponds to the formation of CO_2 by the reaction $Fe_nCO + NO \rightarrow Fe_nN + CO_2$ but not by the reaction $OFe_nN + CO \rightarrow Fe_nN + CO_2$. For example, the $OFe_6N + CO \rightarrow Fe_6N + CO_2$ channel is weakly endothermic (+0.22 eV) while the complimentary channel $Fe_6CO + NO \rightarrow Fe_6N + CO_2$ is highly exothermic (−3.05 eV). Even a larger energy difference was found previously for complimentary channels involving N_2 and O_2 as well as CO and O_2 in their interactions with a Fe_4 cluster. Thus, the reaction energy depends on the order of molecular attachment to a metal cluster which was also observed [29] in experiments involving the oxidation of CO by O_2 on Au/TiO$_2$ catalysts.
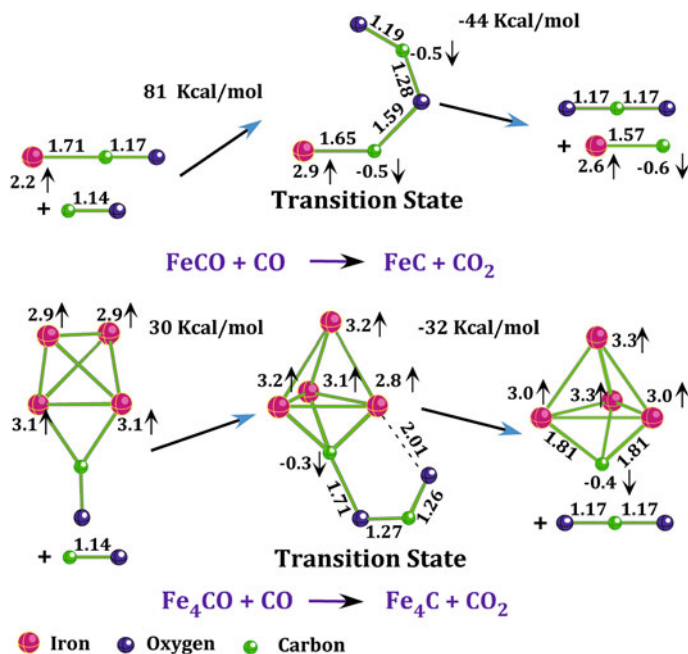
Fig. 12 Transition states for the reactions FeCO + CO → FeC + CO$_2$ and Fe$_4$CO + CO → Fe$_4$C + CO$_2$. Bond lengths are in Å and local spin magnetic moments are in μ_B

Table 7 Energetics of different reactions involving CO and NO with FeNO, OFe$_n$N, and Fe$_n$CO (n = 1–6)

Channel	eV	Channel	eV
FeNO + CO → FeC + NO$_2$	4.81	OFe$_4$N + CO → Fe$_4$C + NO$_2$	4.91
→FeN + CO$_2$	**−0.42**	→Fe$_4$N + CO$_2$	**−0.28**
FeCO + NO → FeC + NO$_2$	3.80	Fe$_4$CO + NO → Fe$_4$C + NO$_2$	2.00
→FeN + CO$_2$	**−1.47**	→Fe$_4$N + CO$_2$	**−3.12**
OFe$_2$N + CO → Fe$_2$C + NO$_2$	5.31	OFe$_5$N + CO → Fe$_5$C + NO$_2$	4.90
→Fe$_2$N + CO$_2$	**−0.14**	→Fe$_5$N + CO$_2$	**−0.15**
Fe$_2$CO + NO → Fe$_2$C + NO$_2$	3.24	Fe$_5$CO + NO → Fe$_5$C + NO$_2$	2.21
→Fe$_2$N + CO$_2$	**−2.26**	→Fe$_5$N + CO$_2$	**−2.84**
OFe$_2$N + NO → Fe$_2$N + NO$_2$	1.93	OFe$_5$N + NO → Fe$_5$N + NO$_2$	2.13
→Fe$_2$O + N$_2$O	**−0.86**	→Fe$_5$O + N$_2$O	0.09
OFe$_3$N + CO → Fe$_3$C + NO$_2$	5.42	OFe$_6$N + CO → Fe$_6$C + NO$_2$	5.20
→Fe$_3$N + CO$_2$	**−0.16**	→Fe$_6$N + CO$_2$	0.22
Fe$_3$CO + NO → Fe$_3$C + NO$_2$	2.65	Fe$_6$CO + NO → Fe$_6$C + NO$_2$	1.93
→Fe$_3$N + CO$_2$	**−2.92**	→Fe$_6$N + CO$_2$	**−3.05**
OFe$_3$N + NO → Fe$_3$N + NO$_2$	2.12	OFe$_6$N + NO → Fe$_6$N + NO$_2$	2.50
→Fe$_3$O + N$_2$O	**−0.45**	→Fe$_6$O + N$_2$O	0.05

Exothermic reactions have a minus sign and are in bold font. All values are in eV

The difference between the reaction energies of complimentary channels is related to the number and strength of the bonds being broken and formed. In order to form $Fe_6N + CO_2$ from $OFe_6N + CO$, one needs to break the $O–Fe_6N$ bond and form the $O–CO$ bond, which are nearly equal in the strength. This is in contrast to forming $Fe_6N + CO_2$ from $Fe_6CO + NO$, where one needs to break a weak $Fe_6–CO$ and a strong $N–O$ bond, followed by the formation of two strong $Fe_6–N$ and two $O–CO$ bonds, which makes the channel highly exothermic. If instead of the OFe_6N isomer, one starts with Fe_6NO, where the NO bonding is more similar to the CO bonding in Fe_6CO, the reaction of $Fe_6NO + CO \rightarrow Fe_6N + CO_2$ would be exothermic by -1.91 eV. The higher exothermicity of the $Fe_6CO + NO \rightarrow Fe_6N + CO_2$ channel with respect to that of the $Fe_6NO + CO \rightarrow Fe_6N + CO_2$ channel is related to a smaller binding energy (1.18 eV) of CO to Fe_6 when compared to the NO binding energy in OFe_6N.

Of course, the energy required for a reaction to take place includes the barrier energies defined by transitions states and accounting for these energies has to equalize the energies of decay channels with the same initial reactants and final products.

Oxidation of C and CO on iron clusters is found [30] to be highly exothermic independent of the cluster size or charge, whereas the removal of oxygen from a Fe_nO cluster with CO is weakly endo- or exothermic in dependence on the iron cluster size as shown in Table 8. The table presents the energetics of the following reactions for the neutral clusters:

$$Fe_nC + O_2 \rightarrow Fe_n + CO_2$$
$$Fe_nCO + O_2 \rightarrow Fe_nO + CO_2$$
$$Fe_nO + CO \rightarrow Fe_n + CO_2$$
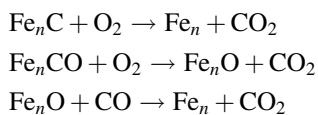
For comparison, the previously described energetics of the $Fe_nCO + CO \rightarrow Fe_nC + CO_2$ channel are also shown. As can be seen, the endothermicity depends on the cluster size for each particular reaction.

Transition states were optimized for the $FeCO + O_2 \rightarrow FeO + CO_2$ and $Fe_4CO + O_2 \rightarrow Fe_4O + CO_2$ reactions (see Fig. 13). In both cases, the transition state energies are below those of the reactants, which suggests that the reactions should be quite rapid. The $Fe_nO + CO \rightarrow Fe_n + CO_2$ for ($n = 3–6$) and $Fe_4O_2 + 2CO \rightarrow Fe_4 + 2CO_2$ reactions are exothermic or slightly endothermic, which leads us to the conjecture that iron clusters at high temperature with an excess of CO, as in the HiPco process, will eliminate the oxygen and restore the cluster for a continued CNT growth. Thus, one can conclude that small amounts of residual oxygen or water should not significantly affect the HiPco process.

$Fe_n + H_2O$. Not much is known about the interactions of water with iron particles. We performed optimizations of the geometrical structure and spin multiplicity of the Fe_nH_2O both in the neutral and singly charged forms for $n = 1–4$.

Table 8 Energetics of different processes involving neutral iron clusters

n	Fe$_n$CO + CO → Fe$_n$C + CO$_2$	Fe$_n$C + O$_2$ → Fe$_n$ + CO$_2$	Fe$_n$CO + O$_2$ → Fe$_n$O + CO$_2$	Fe$_n$O + CO → Fe$_n$ + CO$_2$
1	+1.59	−6.52	−4.20	−0.72
2	+1.10	−5.94	−4.52	−0.32
3	+0.55	−4.98	−4.76	+0.15
4	−0.08	−4.32	−4.48	+0.10
5	+0.12	−4.42	−4.16	−0.14
6	−0.08	−4.90	−4.78	−0.24
Free	CO + CO → C + CO$_2$	C + O$_2$ → CO$_2$	CO + O$_2$ → CO$_2$ + O	O + CO → CO$_2$
Theory	+5.23	−11.41	−0.22	−5.96
Exper.	+5.66	−11.31	−0.20	−5.45

All values are in eV
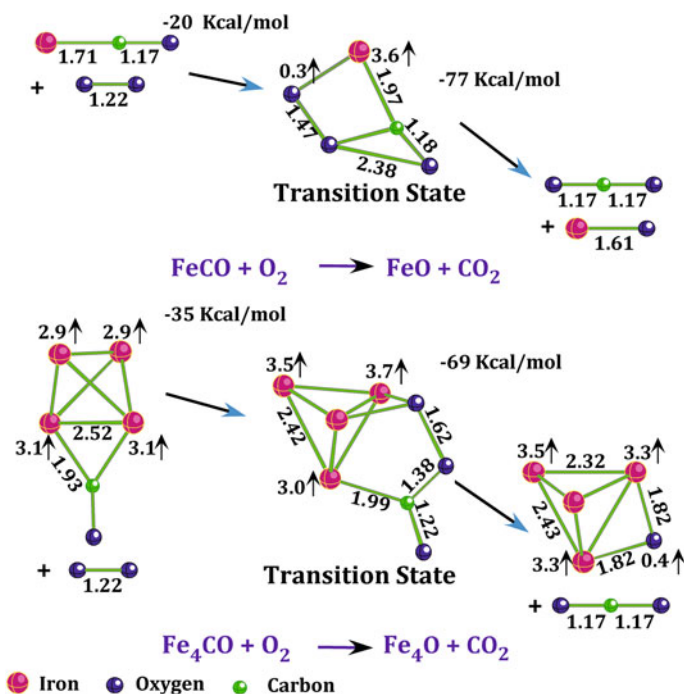
Fig. 13 Transition states of the FeCO + O_2 → Fe + CO_2 and Fe_4CO + O_2 → Fe_4 + CO_2 reactions. Bond lengths are in Å and total spin magnetic moments at atoms are in μ_B. The sum of total energies of the ground-state reactants is taken as zero

As can be seen from Fig. 14, only Fe^+ attaches a water molecule associatively whereas the ground states of FeH_2O, FeH_2O^-, and $Fe_2H_2O^+$ contain the OH group which corresponds to a half-dissociated water molecule. In all other cases, the ground states correspond to fully dissociated water.

The fragmentation energies for different channels of ground-state neutral and ionic Fe_nH_2O are presented in Table 9. Our value of 1.68 eV computed for the Fe^+–H_2O dissociation energy is in agreement with the experimental value of 1.33 ± 0.05 eV deduced from collision induced dissociation experiments. As can be seen from the table, the lowest energy fragmentation channel for all species, except for FeH_2O^+ and $Fe_4H_2O^+$, corresponds to desorption of molecular hydrogen. The next most favorable channel corresponds to the loss of water. The energy for the loss of an H atom is somewhat higher, while the loss of OH requires appreciably higher energies.

Summarising all previous results on the total spin magnetic moments of iron clusters interacting with atoms, diatomics, and H_2O, we present the following chart describing the changes in the total spin magnetic moments:
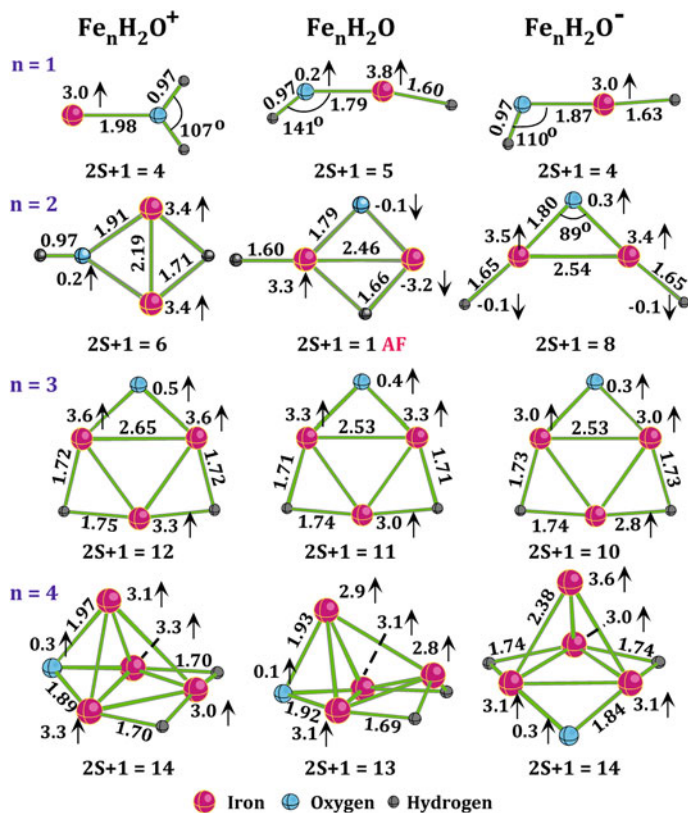
Fig. 14 Geometrical configurations of the lowest total energy isomers of $Fe_nH_2O^+$, Fe_nH_2O, and $Fe_nH_2O^-$. Bond lengths are in Å, total spin magnetic moments of atoms are in μ_B

Bare iron clusters : $6(Fe_2)$, $10(Fe_3)$, $14(Fe_4)$, $16(Fe_5)$, $20(Fe_6)$

Monocarbide iron clusters : $6(Fe_2C)$, $8(Fe_3C)$, $12(Fe_4C)$, $14(Fe_5C)$, $16(Fe_6C)$

Monooxide iron clusters : $6(Fe_2O)$, $10(Fe_3O)$, $12(Fe_4O)$, $16(Fe_5O)$, $20(Fe_6O)$

Monocarbonyl iron clusters : $6(Fe_2CO)$, $8(Fe_3CO)$, $12(Fe_4CO)$, $16(Fe_5CO)$, $18(Fe_6CO)$

Mononitrosyl iron clusters : $5(Fe_2NO)$, $3(Fe_3NO)$, $13(Fe_4NO)$, $9(Fe_5NO)$, $13(Fe_6NO)$

Monohydroxyl iron clusters : $7(Fe_2OH)$, $11(Fe_3OH)$, $13(Fe_4OH)$

Fe_n-H_2O clusters : $0(Fe_2H_2O)$, $10(Fe_3H_2O)$, $12(Fe_4H_2O)$

As can be seen, the attachment of a single atom may not quench the total spin magnetic moments of an iron cluster at all, whereas the attachment of the diatomics and a water molecule results in a quenched total spin magnetic moment except for Fe_2CO, Fe_5CO, and Fe_3H_2O which retain the bare iron cluster moments. The only case of enhancement of the total spin magnetic moment is presented in the Fe_2OH cluster.

Table 9 Fragmentation energies $(D_0,$ eV) of the neutral and charged Fe_nH_2O species

Neutral	D_0	Anion	D_0	Cation	D_0
$FeH_2O \rightarrow FeO + H_2$	**1.37**	$FeH_2O^- \rightarrow FeO^- + H_2$	**1.31**	$FeH_2O^+ \rightarrow FeO^+ + H_2$	2.54
$\rightarrow Fe + H_2O$	1.55	$\rightarrow Fe^- + H_2O$	2.13	$\rightarrow Fe^+ + H_2O$	**1.68**
$Fe_2H_2O \rightarrow Fe_2O + H_2$	**0.64**	$Fe_2H_2O^- \rightarrow Fe_2O^- + H_2$	**1.52**	$Fe_2H_2O^+ \rightarrow Fe_2O^+ + H_2$	**1.21**
$\rightarrow Fe_2 + H_2O$	1.20	$\rightarrow Fe_2^- + H_2O$	2.43	$\rightarrow Fe_2^+ + H_2O$	1.47
$Fe_3H_2O \rightarrow Fe_3O + H_2$	**1.71**	$Fe_3H_2O^- \rightarrow Fe_3O^- + H_2$	**1.46**	$Fe_3H_2O^+ \rightarrow Fe_3O^+ + H_2$	**1.29**
$\rightarrow Fe_3 + H_2O$	2.95	$\rightarrow Fe_3^- + H_2O$	2.57	$\rightarrow Fe_3^+ + H_2O$	1.62
$Fe_4H_2O \rightarrow Fe_4O + H_2$	**1.42**	$Fe_4H_2O^- \rightarrow Fe_4O^- + H_2$	**1.52**	$Fe_4H_2O^+ \rightarrow Fe_4O^+ + H_2$	2.19
$\rightarrow Fe_4 + H_2O$	2.38	$\rightarrow Fe_4^- + H_2O$	2.31	$\rightarrow Fe_4^+ + H_2O$	**1.91**

6 Structure and Magnetic Properties of Larger Neutral and Charged Iron Clusters

A recent theoretical study [31] extends our previous study of neutral and singly negatively and positively charged iron Fe_n clusters from $n = 2$–6 to n values up to 20. The latter value corresponds to the maximum cluster size used in the experimental study of the Fe_n^+ clusters. The vertical and adiabatic ionization energies of the neutral species and the vertical and adiabatic energies of an extra electron detachment from the anionic species have been computed and compared to experiment.

We compute the adiabatic electron affinity (EA_{ad}) of a neutral as

$$EA_{ad}(Fe_n) = E_{tot}^{el}(Fe_n) + E_0(Fe_n) - [E_{tot}^{el}(Fe_n^-) + E_0(Fe_n^-)] \tag{5}$$

where $E_{tot}^{el}(Fe_n)$ and $E_{tot}^{el}(Fe_n^-)$ are the total electronic energies of the lowest energy states of Fe_n and Fe_n^-, and E_0 is the zero-point vibrational energy computed within the harmonic approximation. The adiabatic ionization energy is computed in a similar way

$$IE_{ad}(Fe_n) = E_{tot}^{el}(Fe_n^+) + E_0(Fe_n^+) - [E_{tot}^{el}(Fe_n) + E_0(Fe_n)] \tag{6}$$

The vertical ionization energies (VIE) are computed for two possible one-electron detachment channels corresponding to the cation states whose spin multiplicities differ from the spin multiplicity of the neutral parent by ± 1 at the geometry of the neutral lowest total energy state:

$$VIE_{\pm}(Fe_n) = E_{tot}^{el}(Fe_n^+, (2S+1) \pm 1) - E_{tot}^{el}(Fe_n, 2S+1) \tag{7}$$

The vertical electron detachment energies of an anion are computed at the geometry of the anion lowest total energy state:

$$VDE_{\pm}(Fe_n^-) = E_{tot}^{el}(Fe_n, 2S+1) - E_{tot}^{el}(Fe_n^-, (2S+1) \pm 1) \tag{8}$$

The energy of a Fe atom abstraction from Fe_{n+1} is computed as

$$D_0(Fe_n - Fe) = E_{tot}^{el}(Fe_n) + E_0(Fe_n) + E_{tot}(Fe) - [E_{tot}^{el}(Fe_{n+1}) + E_0(Fe_{n+1})] \tag{9}$$

Atomization energy of a Fe_n cluster is computed as

$$E_{atom}(n) = [E_{tot}^{el}(Fe_n) + E_0(Fe_n) - nE_{tot}(Fe)]/n \tag{10}$$

Local spin magnetic moments on atoms, which are identified with the excess spin densities on atoms, are obtained using the Natural Atomic Orbital (NAO) population analysis.

Geometrical Configurations

For each cluster, a number of trial geometric configurations including those obtained in the previous work have been tested. Each geometry optimization was followed by harmonic frequency computations in order to confirm the stationary character of the state obtained. If an optimization arrived at a transition state, optimizations which followed the imaginary frequency modes were performed until all imaginary frequencies were eliminated. The geometrical structures obtained for the lowest total energy states of Fe_n^+, Fe_n, and Fe_n^- ($n = 7$–20) are presented in Figs. 15, 16, 17, 18, where each state is specified by its spin multiplicity $M = 2S + 1$. The neutral geometrical configurations found are similar to those in the previous work except for Fe_{17}, whose lowest total energy state geometrical configuration, found in this work, is similar to that found in a salt.

The structural patterns in the lowest total energy states in the neutral Fe_n series can be described as follows: from $n = 7$ to $n = 12$, the structures are formed by stripping off atoms from a slightly distorted icosahedral Fe_{13} cluster; for $n = 14$, a six-member ring replaces a five-member ring; for $n = 15$, the second six-member

Fig. 15 Geometrical configurations of the lowest total energy isomers of Fe_n^+, Fe_n, and Fe_n^- ($n = 7$–10). Bond lengths are in Å, total spin magnetic moments at atoms are in μ_B
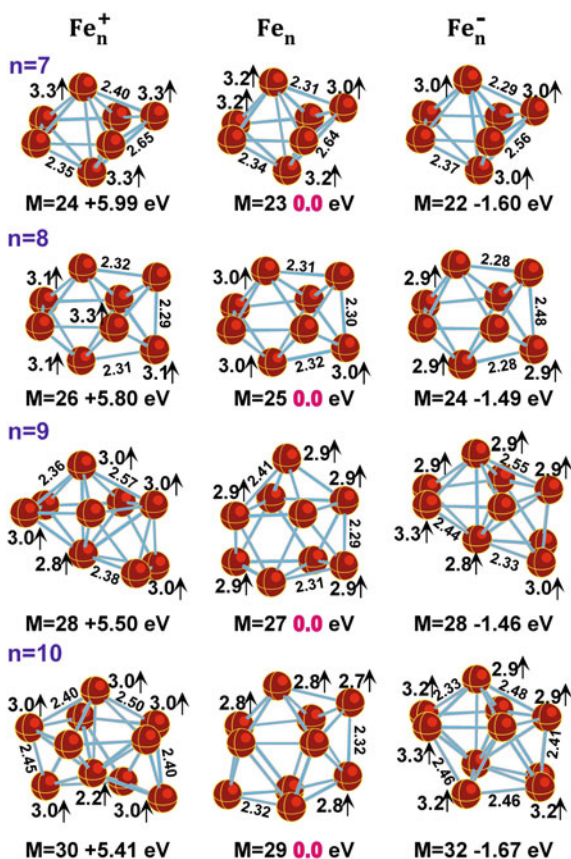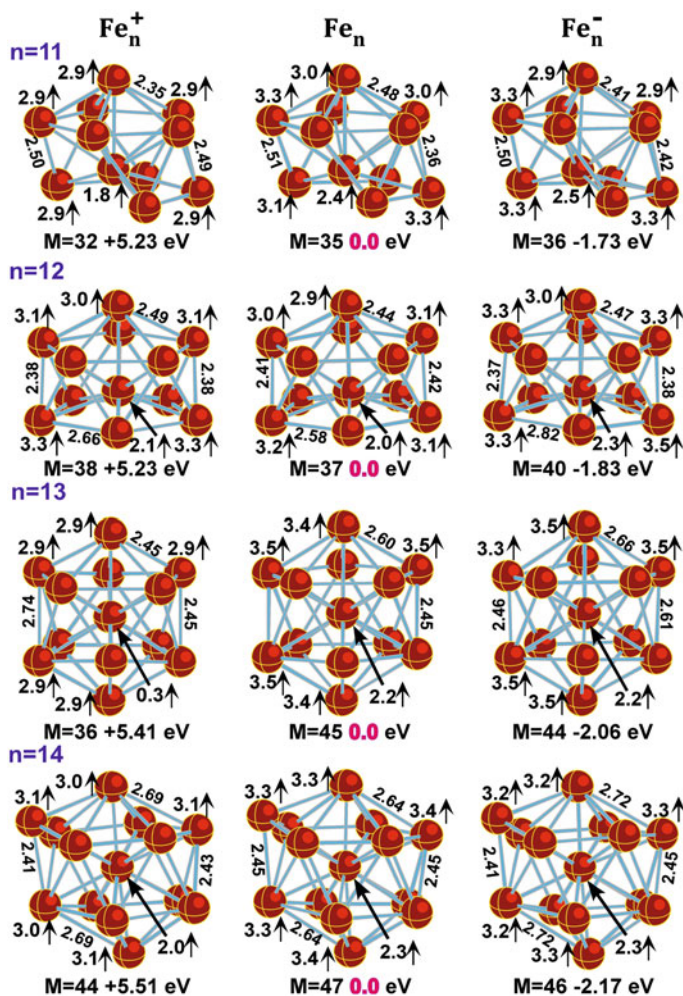
Fig. 16 Geometrical configurations of the lowest total energy isomers of Fe_n^+, Fe_n, and Fe_n^- ($n = 11$–14). Bond lengths are in Å, total spin magnetic moments at atoms are in μ_B

ring replaces the second five-member ring; from $n = 16$ to 19, the structures contain two six-member rings and the caps consisting of one to four atoms. The second core atom appears in the geometrical structure of the lowest total energy state of Fe_{20}, which consists of two five-member rings and one six-member ring in the middle capped by two single atoms.

The geometrical configurations of the lowest states in the Fe_n^+ and Fe_n^- series are similar to those of the corresponding neutral clusters except for a few cases. In the cation series, the geometrical configurations of Fe_9^+, Fe_{10}^+, and Fe_{19}^+ are different from the geometrical configurations of the corresponding neutral species. In the
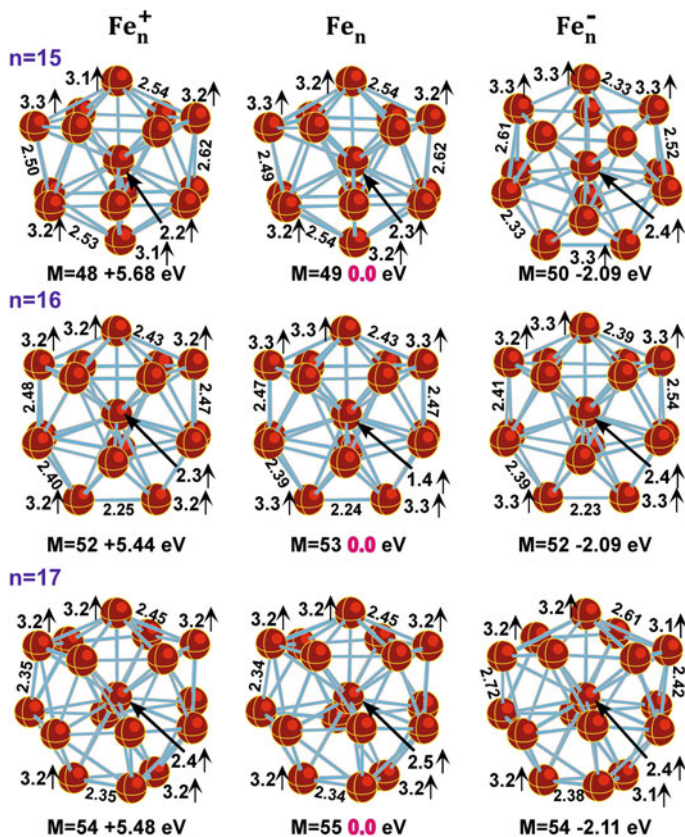
Fig. 17 Geometrical configurations of the lowest total energy isomers of Fe_n^+, Fe_n, and Fe_n^- ($n = 15$–17). Bond lengths are in Å, total spin magnetic moments at atoms are in μ_B

anion series, the difference between geometries is observed for Fe_9^-, Fe_{10}^-, and Fe_{15}^-. In all other cases, the attachment/detachment of an electron to/from a neutral cluster does not lead to a significant change in the bond lengths. This can be seen from the comparison of the bond lengths given in Figs. 15, 16, 17, 18. Typically, the bond length changes do not exceed 0.05 Å. Occasionally, some bond changes are larger by up to 0.2 Å.

Ionization Energies and Electron Affinities

After the lowest total energy states in all three Fe_n series have been found, we computed the vertical and adiabatic ionization energies of the neutral Fe_n clusters according to Eqs. 6 and 7 and compared the values obtained with experimental data in Table 10. As can be seen in the table, the adiabatic and vertical ionization energies are quite close to each other, except for $n = 9$, 10, 13, and 19. The reason for the difference between the adiabatic and vertical ionization energies for the latter n values can be related to the difference between the geometrical configurations of the corresponding
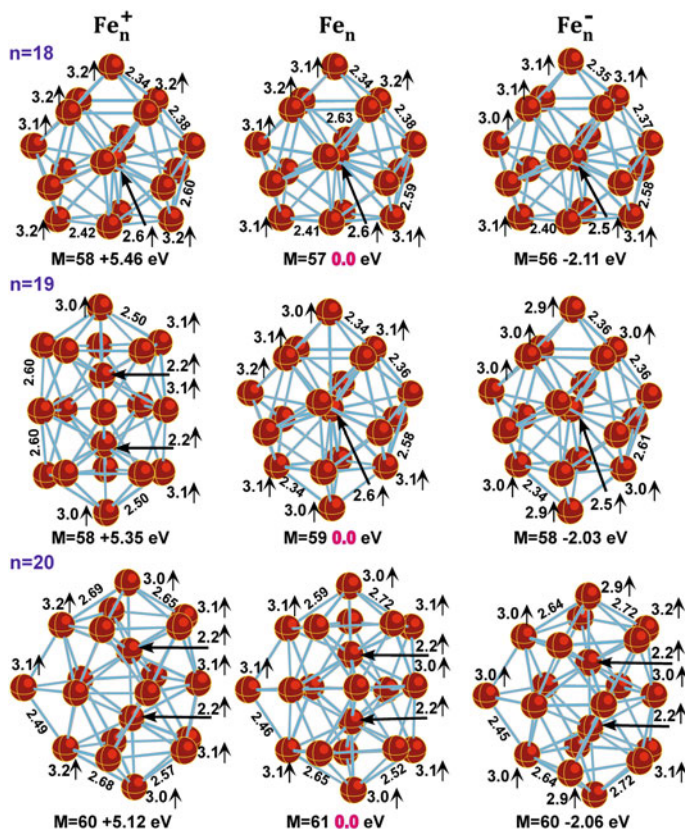
Fig. 18 Geometrical configurations of the lowest total energy isomers of Fe_n^+, Fe_n, and Fe_n^- ($n = 18$–20). Bond lengths are in Å, total spin magnetic moments at atoms are in μ_B

neutrals and cations, whereas the Fe_{13} and Fe_{13}^+ pair presents a case where the electron detachment leads to an anomalous lowering of the total spin magnetic moment. The computed adiabatic ionization energies do match the corresponding experimental values within the experimental uncertainty bars in nearly all cases.

The adiabatic electron affinities of the neutrals computed according to Eq. 5 and the vertical detachment energies of an extra electron from the Fe_n^- anions computed according to Eq. 8 are presented in Table 11 and compared to the experimental values obtained using laser photodetachment spectroscopy. The experimental data correspond to the vertical electron detachment and possess quite narrow uncertainty bars. As is can be seen from Table 11, our differences between the smallest vertical detachment energies for each n and the experimental values are within 0.2 eV.

Spin Magnetic Moments

Computed total spin magnetic moments of iron clusters are found to be quite sensitive to the method of calculations. Figure 19 compares our total spin magnetic moments

Table 10 Computed vertical ($VIE_{\pm}$) and adiabatic (IE_{ad}) ionization energies of neutral iron clusters along with experimental data

	Fe$_7$	Fe$_8$	Fe$_9$	Fe$_{10}$	Fe$_{11}$	Fe$_{12}$	Fe$_{13}$
$M = 2S + 1$	23	25	27	29	35	37	45
VIE_+	6.09	5.95	5.69	5.68	5.78	5.33	5.89
VIE_-	6.14	6.32	6.03	5.92	5.33	5.27	5.62
IE_{ad}	**5.99**	**5.80**	**5.49**	**5.19**	**5.23**	**5.23**	**5.41**
Experim.	5.76 ± 0.05	5.48 ± 0.05	5.50 ± 0.05	5.41 ± 0.05	5.45 ± 0.05	5.52 ± 0.05	5.61 ± 0.05
Experim.	5.97 ± 0.39	5.97 ± 0.39	5.44 ± 0.14	5.44 ± 0.14	5.42 ± 0.16	5.42 ± 0.16	5.76 ± 0.18
	Fe$_{14}$	Fe$_{15}$	Fe$_{16}$	Fe$_{17}$	Fe$_{18}$	Fe$_{19}$	Fe$_{20}$
$M = 2S + 1$	47	49	53	55	57	59	61
VIE_+	5.92	5.81	5.81	5.67	5.51	5.63	5.22
VIE_-	5.63	5.68	5.44	5.48	5.51	5.51	5.18
IE_{ad}	**5.51**	**5.68**	**5.44**	**5.48**	**5.46**	**5.35**	**5.12**
Experim.	5.70 ± 0.05	5.56 ± 0.05	5.63 ± 0.05	5.50 ± 0.05	5.40 ± 0.05	5.18 ± 0.05	…
Experim.	5.80 ± 0.19	5.40 ± 0.18	5.64 ± 0.06	5.57 ± 0.13	5.40 ± 0.18	5.12 ± 0.15	5.12 ± 0.15

All values are in eV

Table 11 Computed vertical extra electron detachment energies ($VDE_\pm$) of the Fe_n^- anions and adiabatic electron affinities (EA_{ad}) along with the experimental data

	Fe_7^-	Fe_8^-	Fe_9^-	Fe_{10}^-	Fe_{11}^-	Fe_{12}^-	Fe_{13}^-
$M = 2S + 1$	22	24	28	32	36	40	44
VDE_+	**1.73**	**1.73**	1.70	1.84	2.12	2.33	2.22
VDE_-	2.08	2.13	**1.50**	**1.74**	**1.76**	**1.87**	**2.12**
EA_{ad}	1.60	1.49	1.46	1.67	1.73	1.83	2.06
Experim.	1.39 ± 0.08	1.66 ± 0.08	1.75 ± 0.08	1.85 ± 0.08	2.00 ± 0.08	2.12 ± 0.08	2.20 ± 0.08
Experim.	1.50 ± 0.06	1.76 ± 0.06	1.80 ± 0.06	1.90 ± 0.06	2.03 ± 0.06	2.14 ± 0.06	2.24 ± 0.06
	Fe_{14}^-	Fe_{15}^-	Fe_{16}^-	Fe_{17}^-	Fe_{18}^-	Fe_{19}^-	Fe_{20}^-
$M = 2S + 1$	46	50	52	54	56	58	60
VDE_+	2.29	2.52	**2.20**	**2.18**	**2.16**	**2.13**	**2.03**
VDE_-	**2.22**	**2.10**	2.23	2.34	2.39	2.40	2.28
EA_{ad}	2.17	2.09	2.09	2.11	2.14	2.03	1.99
Experim.	2.23 ± 0.08	2.25 ± 0.08	2.01 ± 0.08	2.06 ± 0.08	2.14 ± 0.08	2.01 ± 0.08	2.01 ± 0.08
Experim.	2.26 ± 0.06	2.28 ± 0.06	2.09 ± 0.06	2.16 ± 0.06	2.22 ± 0.06	2.11 ± 0.06	2.10 ± 0.06

All values are in eV

Fig. 19 Comparison of the total spin magnetic moment per atom obtained using DFT, DFT-TB, and DFT-ECP methods. The DFT-ECP computations were performed for $n = 2$–17
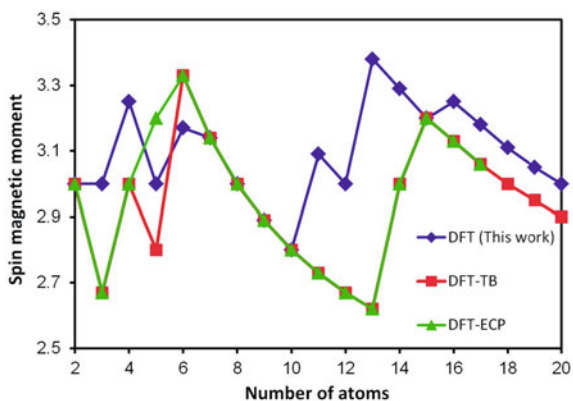
per atom with the values obtained previously using a DFT method with an effective core potential (DFT-ECP) [32] and a semiempirical DFT method with a tight-binding approximation (DFT-TB) [33].

The DFT-TB values match the DFT-ECP values except for $n = 5$, which is due to the fact that tight-binding parameters were calibrated using the DFT-ECP results. Our computed values match the DFT-ECP values only for $n = 2, 7, 8, 9, 10$ and 15. The largest difference of $0.8 \, \mu_B$ is found for $n = 13$, where the DFT value is the maximal value in the series, whereas the DFT-ECP value is the minimal one.

The dependence of the total spin magnetic moment per atom on the cluster charge is shown in Fig. 20. According to the one-electron model, the total spin magnetic moment of a singly charged cluster, whether it is positively or negatively charged, should differ from the total spin magnetic moment of its neutral parent by $\pm 1.0 \, \mu_B$. This is assuming that the geometric structures and hence the electron energy levels do not change significantly when the electron is either detached or

Fig. 20 Total spin magnetic moment per atom (in μ_B) in the $Fe_n^{0/-1/+1}$ series
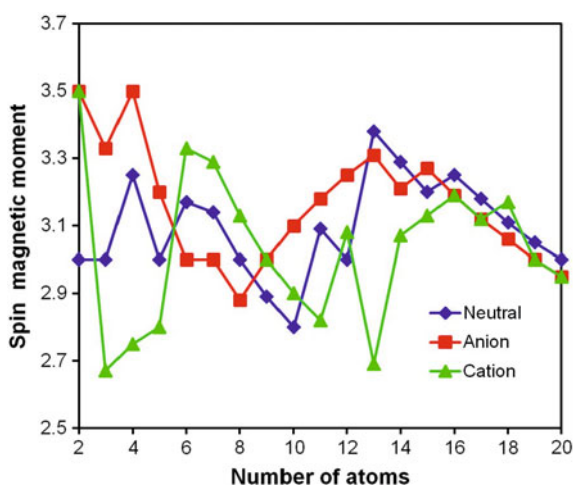
attached. A reduction in the total spin magnetic moment occurs when the electron is removed from the majority spin orbital while an enhancement in the moment occurs when the electron is removed from the minority spin orbital. Among iron clusters considered in this work, only Fe_{10}^{-} and Fe_{12}^{-} in the anion series as well as Fe_4^+, Fe_{11}^+, Fe_{13}^+, and Fe_{14}^+ in the cation series do not obey this one-electron rule. The corresponding differences are $+3 \mu_B$ (Fe_{10}^{-}), $+3 \mu_B$ (Fe_{12}^{-}), $-3 \mu_B$ (Fe_4^+), $-3 \mu_B$ (Fe_{11}^+), $-9 \mu_B$ (Fe_{13}^+), and $-3 \mu_B$ (Fe_{14}^+).

The dramatic decrease in the total spin magnetic moment of the Fe_{13}^+ cation is in agreement with the results of recent XMCD measurements [3]. Table 12 compares our total spin magnetic moments per atom to the XMCD data in the whole measurement range. As can be seen, an anomalous quenching of the total magnetic moment is observed only for Fe_{13}^+, whose total magnetic moment is $2.63 \pm 0.41 \mu_B$, whereas the neighbors Fe_{12}^+ and Fe_{14}^+ possess the total magnetic moments of $3.34 \pm 0.43 \mu_B$ and $3.62 \pm 0.50 \mu_B$, respectively. We will discuss possible reasons for the anomalous behavior of the total spin magnetic moment in Fe_{13}^+ in the next section.

Our total spin magnetic moment per atom computed for Fe_{13}^+ is $2.69 \mu_B$ and agrees well with the experimental value of $2.44 \pm 0.38 \mu_B$. Generally, our computed spin magnetic moments per atom match the experimental values within the experimental uncertainty bars. Since the orbital magnetic moment contribution to the total magnetic moment is small according to the XMCD data in Table 12, one can consider the total spin magnetic moment to be a good approximation to the total magnetic moment in iron clusters.

Thermodynamic Stability

The energy corresponding to the abstraction of one Fe atom from the neutral and charged iron clusters are computed according to Eq. 9 and are presented in Table 13 together with experimental data. Generally, our values differ by no more than 0.4 eV from the experimental values if the corresponding uncertainty bar values are accounted for, except for the Fe_8 cluster where the discrepancy is 0.79 eV. The experiment predicts Fe_{13} to be the most stable species with respect to a Fe atom abstraction among iron clusters of this size; however, we found that Fe_{15} is the most stable cluster in the series. The binding energy per atom of 3.16 eV in the largest Fe_{20} cluster is still substantially smaller than the bulk iron cohesive energy of 4.39 eV. Comparison of the energy abstraction of a Fe atom in the neutral and charged Fe_n clusters is presented in Fig. 21. As can be seen, the abstraction energy of a Fe atom is nearly independent of the charge for a given n.

In order to estimate the relative stabilities of neutral and charged iron clusters, we use the conventional formula for the second total energy differences $\Delta_2 E_{tot}(n) = E_{tot}(n + 1) - 2E_{tot}(n) + E_{tot}(n - 1)$. One can rewrite this formula as

$$\begin{aligned} \Delta_2 E_{tot}(n) &= [E_{tot}(n+1) - E_{tot}(n) - E_{tot}(1)] - [E_{tot}(n) - E_{tot}(n-1) - E_{tot}(1)] \\ &= D_0(Fe_{n+1}) - D_0(Fe_n) \end{aligned}$$

$$(11)$$

Table 12 Total spin magnetic (SMM) and total magnetic (TMM) moments per atom of the Fe_n^+ cations

	Fe_7^+	Fe_8^+	Fe_9^+	Fe_{10}^+	Fe_{11}^+	Fe_{12}^+	Fe_{13}^+
SMM (theo)	**3.29**	**3.13**	**3.0**	**2.90**	**2.82**	**3.08**	**2.69**
SMM (exper)	3.13 ± 0.46	3.19 ± 0.46	2.76 ± 0.38	3.44 ± 0.46	3.30 ± 0.42	3.41 ± 0.50	2.44 ± 0.38
TMM (exper)	3.42 ± 0.50	3.45 ± 0.46	3.35 ± 0.38	3.63 ± 0.48	3.48 ± 0.46	3.50 ± 0.51	2.63 ± 0.41
	Fe_{14}^+	Fe_{15}^+	Fe_{16}^+	Fe_{17}^+	Fe_{18}^+	Fe_{19}^+	Fe_{20}^+
SMM (theo)	**3.07**	**3.13**	**3.19**	**3.12**	**3.17**	**3.0**	**2.95**
SMM (exper)	3.49 ± 0.49	3.7 ± 0.49	3.56 ± 0.48	3.15 ± 0.42	3.47 ± 0.46	3.34 ± 0.43	3.45 ± 0.45
TMM (exper)	3.62 ± 0.50	3.88 ± 0.51	3.68 ± 0.49	3.55 ± 0.47	3.59 ± 0.47	3.61 ± 0.47	3.89 ± 0.50

All values are in μ_B

Table 13 Comparison of an Fe atom abstraction energy [$D_0(Fe_n–Fe)$] to experiment and atomization energy per atom (E_{atom})

	Fe_7	Fe_8	Fe_9	Fe_{10}	Fe_{11}	Fe_{12}	Fe_{13}
$M = 2S + 1$	23	25	27	29	35	37	45
$D_0(Fe_n–Fe)$	3.48	3.27	2.99	3.20	3.38	3.57	3.79
Exper.	3.12 ± 0.15	2.33 ± 0.15	2.92 ± 0.15	2.86 ± 0.15	3.22 ± 0.15	3.52 ± 0.15	4.32 ± 0.15
E_{atom}	2.58	2.67	2.70	2.75	2.81	2.87	2.94
	Fe_{14}	Fe_{15}	Fe_{16}	Fe_{17}	Fe_{18}	Fe_{19}	Fe_{20}
$M = 2S + 1$	47	49	53	55	57	59	61
$D_0(Fe_n–Fe)$	3.48	4.38	3.51	3.50	3.36	3.45	3.24
Exper.	3.01 ± 0.15	3.76 ± 0.15	3.38 ± 0.15	3.21 ± 0.15	3.13 ± 0.15	3.65 ± 0.15	…
E_{atom}	2.98	3.08	3.10	3.13	3.14	3.16	3.16

All values are in eV

Fig. 21 Dissociation energies of the $Fe_n^{0/-1/+1} \rightarrow Fe_{n-1}^{0/-1/+1} +$ Fe channels
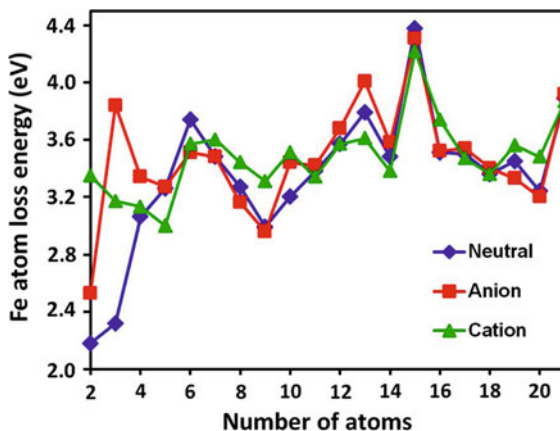
The results of computations using this equation are displayed in Fig. 22 for the neutral and charged iron clusters. Except for small n values, the behavior of the $\Delta_2 E_{tot}(n)$ function in the case of the neutral, anionic, and cationic iron clusters is similar. We note that Fe clusters containing 7, 13, 15, and 19 atoms are among the most stable ones, which agrees with experimental data on the intensity distribution of the mass spectra [34], and the experimentally obtained magic numbers match our values. However, the theory also predicts one more magic number at $n = 10$ which is lacking in the abundance spectrum. On the whole, one can anticipate that the thermodynamics of neutral and charged iron clusters can be satisfactorily described by DFT methods.

Fig. 22 Second-order differences of the $Fe_n^{0/-1/+1}$ total energies
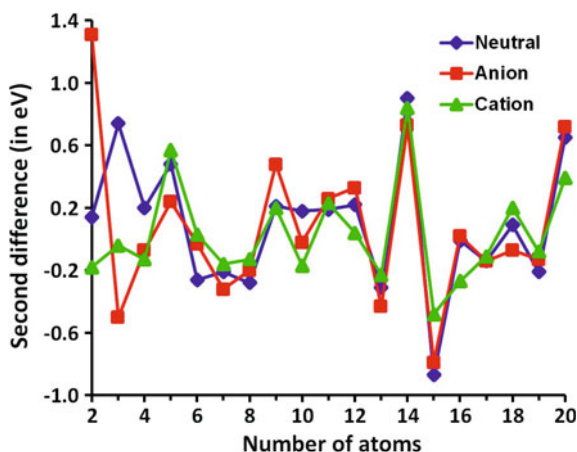
7 Anomalous Total Spin Magnetic Moment of Fe_{13}^+

The anomalous quenching of the total spin magnetic moment of Fe_{13}^+ by 9.0 μ_B with respect to the total spin magnetic moment of the neutral Fe_{13} parent could be due to the antiferromagnetic coupling between the magnetic moments of the central atom and the surface atoms. A ferrimagnetic state possessing such a coupling was found [35] to have a total magnetic moment of 34 μ_B in the *neutral* Fe_{13} cluster, whereas the total spin magnetic moment in the ferromagnetic ground state is 44 μ_B. If one accepts such an explanation, then the next question would be: why is similar quenching of the total magnetic moment not observed in the neighbors Fe_{12}^+ and Fe_{14}^+. The corresponding neutral parents possess quite similar geometric structures resulting from adding (Fe_{14}) or removing (Fe_{12}) a Fe atom to/from a nearly icosahedral geometrical configuration of Fe_{13}.

In order to explore in more detail the dependence of total energies of Fe_{13} and Fe_{13}^+ on spin flips of local spin magnetic moments on atoms we performed a search for the lowest total energy states with one or two local atom spin flips. Figure 23 shows

Fig. 23 Geometrical configurations of the lowest total energy state (G.S.) and the two antiferrimagnetic states of Fe_{13} and Fe_{13}^+. Bond lengths are in Å, the local spin magnetic moments are in μ_B. The *blue* (light) color is used for the atoms whose local spin magnetic moments are antiferromagnetically coupled to the local spin magnetic moments of atoms marked with *red* (dark) color
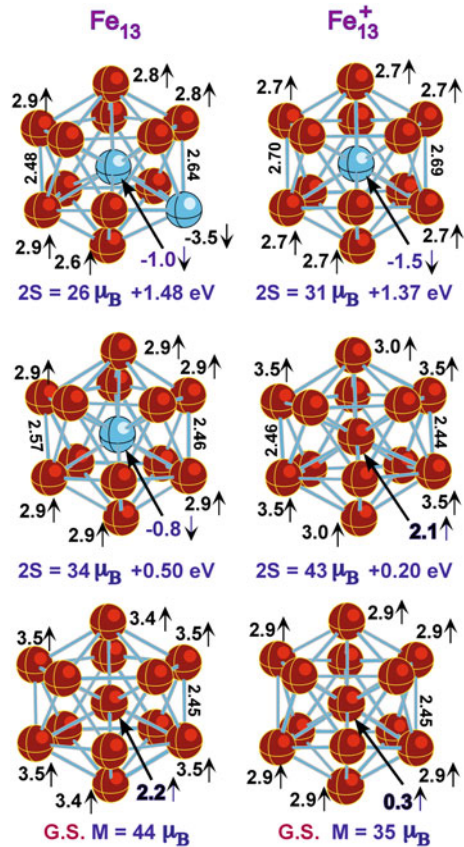
geometrical configurations of Fe_{13} and Fe_{13}^+ corresponding to the lowest total energy state and isomers corresponding to the antiferromagnetic states where the local spin magnetic moments of one or two atoms are antiferromagnetically coupled to those of the rest of the atoms. The total spin magnetic moment of 2.2 μ_B at the central atom in the neutral Fe_{13} ground state is almost quenched in the Fe_{13}^+ ground state. This is further accompanied by a reduction in the magnetic moments of the surface atom of the ionized cluster. The cation states expected on the basis of the one-electron model ($2S \rightarrow 2S \pm 1$) are higher in total energy than the cation ground state ($2S = 35$ μ_B) by 0.32 eV ($2S = 45$ μ_B) and 0.20 eV ($2S = 43$ μ_B).

In order to confirm that the quenching of the total spin magnetic moment in the Fe_{13}^+ ground state is not related to the spin flips of the local spin magnetic moments we considered the neighbor Fe_{12}–Fe_{12}^+ pair (see Fig. 24). According to the figure, no such anomaly as seen in the Fe_{13}–Fe_{13}^+ pair is observed. The lowest total energy state of the cation possesses $2S = 37$ μ_B and the state with $2S = 35$ μ_B is higher by 0.02 eV. Note that both of these states are consistent with the one-electron model. Our total spin magnetic moment per atom in Fe_{12}^+ is 3.0 μ_B, which fits the experimental value of 3.4 $\pm$ 0.5 μ_B within the experimental error bars.

Fig. 24 Geometrical configurations of the lowest total energy states (G.S.) of Fe_{12} and Fe_{12}^+ and their states where the total spin magnetic moment of the central atom is antiferromagnetically coupled to the total spin magnetic moments of the surface atoms. Bond lengths are in Å, the local spin magnetic moments are in μ_B
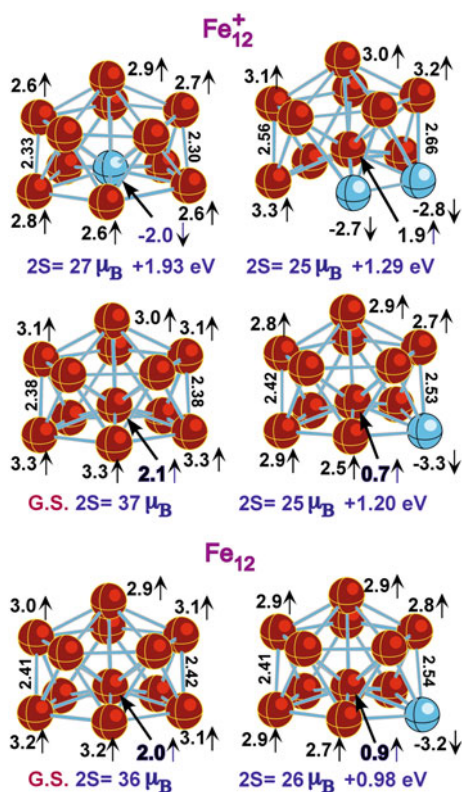
In order to gain insight into the anomalous behavior of the total magnetic moment of Fe$_{13}^+$, we analyze the NAO populations in the lowest total energy states of Fe$_{13}$ and Fe$_{13}^+$, which reflect their chemical bonding peculiarities. Table 14 presents the majority spin, minority spin and total NAO populations of Fe$_{13}$ and Fe$_{13}^+$. The total populations in the neutral Fe$_{13}$ cluster are rather typical and correspond to the promotion of a $4s$ electron into the minority $3d$-shell in the ground-state $3d^64s^2$ electronic configuration of a Fe atom (see the last column in Table 14). In Fe$_{13}^+$, the $4s$ atomic states are depleted because of their promotion not only into the minority $3d$ shells but also into the $4p$ states, which apparently are more accessible in positively charged species than in the corresponding neutrals. The net difference between the sums of the total occupations in Fe$_{13}$ and Fe$_{13}^+$ is 0.8 e instead of 1.0 e because of the small discarded populations of excited AOs.

Comparing the majority and minority spin populations, one may notice that the promotion of $4s$ majority electrons into $4p$ vacant orbitals of the surface and central atoms leads to a difference of -4.85 e between the cation and neutral majority spin populations. Note, that there are two apex and ten ring atoms in the Fe$_{13}$ geometrical structure. The deficit of 0.15 e, which is required to yield an integer number 5, comes from the neglected populations of higher excited orbitals. On the contrary, the difference between the total minority spin populations of Fe$_{13}^+$ and Fe$_{13}$ is $+4.0$ e. That is, the net change in the excess spin densities is 9 μ_B.

It is natural to ask as to why does such a significant $4s \rightarrow 4p$ promotion resulting in a large decrease in the total spin magnetic moment is realized only in Fe$_{13}^+$? The answer is related to the high T_h symmetry of this cation wave function. The bonding orbitals belonging to the T_{1u} representation of the T_h point group are composed of $4p$-orbitals and accommodate six electrons. This special set of bonding orbitals causes the Fe$_{13}^+$ cation to be thermodynamically more stable than any other cation in this size range.

In terms of the molecular orbital occupation, the valence electrons occupy all degenerate sets of the orbitals of e and t symmetry in each spin representation and the ground state of Fe$_{13}^+$ is ^{36}A$_u$. In this state, the α-spin representation contains

Table 14 Natural atomic orbital populations in the lowest total energy states of Fe$_{13}$ and Fe$_{13}^+$

Fe$_{13}$, 2S = 44 μ_B							
	Spin majority	N_{el}	Spin minority	N_{el}	Total	N_{el}
Central Fe	$3d^{5.06}4s^{0.44}4p^{0.04}$	5.54	$3d^{2.73}4s^{0.53}4p^{0.09}$	3.29	$3d^{7.79}4s^{0.91}4p^{0.13}$	8.83
Apex Fe	$3d^{4.96}4s^{0.63}4p^{0.04}$	5.63	$3d^{1.93}4s^{0.30}4p^{0.03}$	2.26	$3d^{6.89}4s^{0.93}4p^{0.07}$	7.89
Ring Fe	$3d^{4.96}4s^{0.69}4p^{0.04}$	5.69	$3d^{1.88}4s^{0.30}4p^{0.03}$	2.21	$3d^{6.84}4s^{0.98}4p^{0.07}$	7.90
Fe$_{13}^+$, 2S = 35 μ_B							
Central Fe	$3d^{4.21}4s^{0.25}4p^{1.04}$	5.49	$3d^{3.91}4s^{0.27}4p^{1.05}$	5.23	$3d^{8.13}4s^{0.58}4p^{2.09}$	10.74
Apex Fe	$3d^{4.92}4s^{0.20}4p^{0.16}$	5.28	$3d^{2.07}4s^{0.17}4p^{0.15}$	2.39	$3d^{7.00}4s^{0.37}4p^{0.31}$	7.68
Ring Fe	$3d^{4.92}4s^{0.20}4p^{0.16}$	5.28	$3d^{2.07}4s^{0.17}4p^{0.15}$	2.39	$3d^{7.00}4s^{0.37}4p^{0.31}$	7.68
$\Delta_{\text{Cat-Neutr}}$		-4.85		$+4.0$		$+0.8$

N_{el} denotes the total electron population of atomic valence orbitals. Small contributions from excited orbitals are omitted. $\Delta_{\text{Cat-Neutr}}$ is the difference between the total occupations from the top and bottom parts of the corresponding column

nine valence MOs of t_u symmetry and eight valence MOs of t_g symmetry occupied by three electrons each, whereas the β-spin representations contains five occupied valence MOs of t_u symmetry and four occupied valence MOs of t_g symmetry. Since a fully occupied $t_u - t_g$ pair corresponds to six LSOs, there are three bonding t_u MOs left in each spin representations ($9 - 8 = 1$, $5 - 4 = 1$). This makes Fe_{13}^+ unique. The states of Fe_{13}^+ and Fe_{13} with larger spin multiplicities optimized within T_h symmetry constraints contain partially occupied generate MOs sets and are subject to Jahn-Teller distortions. The ground state of Fe_{13} is also resolved by symmetry and is $^{45}A_u$ but within D_{2h} symmetry constraints. The closest state of Fe_{13} resolved within T_h symmetry constraints is $^{47}A_u$ and it is higher in total energy than the ground state by 0.28 eV.

8 Doping of Icosahedral Fe_{13} with 3d- and 4d-Atoms

Nanoscale clusters consisting of identical or different type atoms possess the properties which are generally different from those of the corresponding bulk. The physics of these clusters attracts a rapidly growing interest because of a large number of promising applications. Clusters composed of transition nd-metal and rare earth atoms present a special interest because they can possess magnetic moments which are substantially larger than the magnetic moments of the corresponding nd-metal bulk. Of particular interest are binary clusters formed by transition metal or rare earth atoms because they are considered to be precursors for binary alloys playing a crucial role in industry. A wide range of different compositions similar to that of the corresponding bulk alloys is possible, along with additional compositions which may not be realized in the bulk. In order to gain insight on how the doping can change the total spin magnetic moments of larger iron clusters which possess [36, 37] the largest total spin magnetic moments among 3d, 4d, and 5d unary clusters, we consider a ground-state Fe_{13} cluster [38]. This cluster has the smallest number of nonequivalent sites because of its near-icosahedral geometry. The nonequivalent trial geometries are shown in Fig. 25 with the Ni substitution as an example.

The geometrical structures found for the lowest total energy states of $Fe_{12}X$ (X = Al and 3d-metal atoms) are shown in Fig. 26. The states with the geometrical structures obtained from Fe_{14} with the removed central atom are appreciably higher in total energy. The optimized cage geometrical structures are similar to those shown in Fig. 25 for $Fe_{12}Ni$, except for a few cases where some cage structures converged to the icosahedral structures shown in Fig. 26. The central position is preferred in substitutions of the central Fe atom with Ti, V, Cr, and Co atoms whereas the surface position is more energetically favorable for the rest of the atoms.

No appreciable change in the bond lengths due to substitution is observed. The local spin magnetic moment of a substituent atom decreases with respect to that of the substituted iron atom except for the surface Mn atom whose local spin magnetic moment is 4.6 μ_B. For Mn, the central substitution is slightly less favorable than the

Fig. 25 Non-equivalent substitution sites of Fe_{13} and Fe_{14} with the pinned-out central atom. The results of optimizations are presented for $Fe_{12}Ni$ as an example. S denotes the total spin, the energy shifts are given with respect to the lowest total energy state with the geometrical structure corresponding to a surface Ni atom substitution
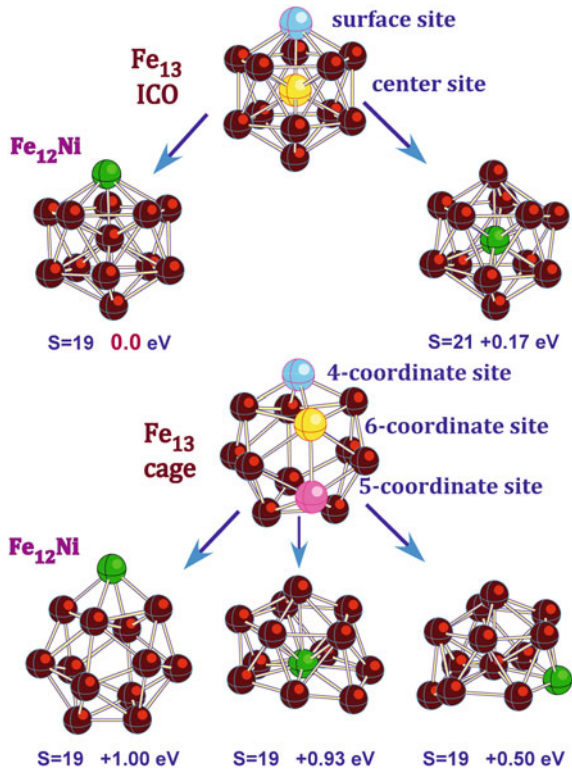
surface substitution and it results in a drastic reduction in the total spin. The Cr substitution presents the only case where the local spin magnetic moment of the substituent atom is antiferromagnetically coupled to the local spin magnetic moments of iron atoms in the $Fe_{12}X$ clusters.

Among 4d-metal atoms, the central substitution position is favorable only in $Fe_{12}Mo$ and $Fe_{12}Tc$ (3d-metal analogs are $Fe_{12}Cr$ and $Fe_{12}Mn$, respectively). The geometrical structure of the lowest total energy state of $Fe_{12}Nb$ was obtained during optimizations of a 6-coordinate shell structure in Fig. 25 where the substituent atom is located in the center of a hexagonal ring. The substituent atoms possess relatively small spin magnetic moments except for Ru, which has a total spin magnetic moment similar to the average spin magnetic moment of the iron atoms, and Gd, whose total spin magnetic moment is smaller than that of a free Gd atom by $\sim 1\,\mu_B$. Only in one case is the total spin magnetic moment of a substituent atom (Zr) coupled antiferromagnetically to the total spin magnetic moments of the iron atoms. The bond lengths between iron atoms and the 4d-substituent atoms are larger by ~ 0.2 Å than those in the case of the 3d-substituent atoms. The largest bond lengths between a substituent atom and the iron atoms are found in $Fe_{12}Gd$.

The states of all $Fe_{12}X$ with geometrical structures obtained from optimizations of cage structures (see Fig. 25) are substantially higher in total energy than the states

Fig. 26 Geometrical structures of the lowest total energy states of $Fe_{12}X$ (X = Al and 3d-metal atoms). Bond lengths are in Å, local spin magnetic moments are in μ_B
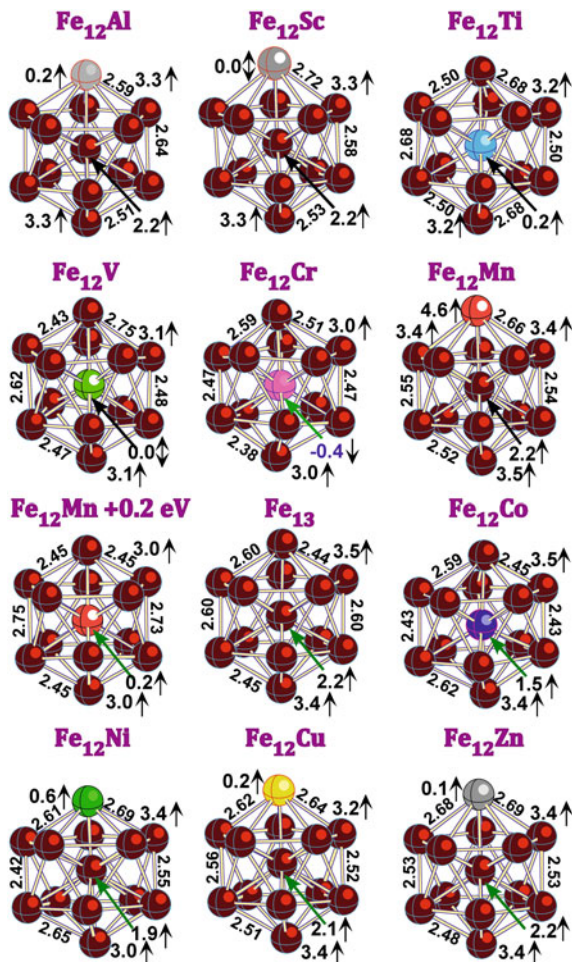
with the geometrical structures shown in Figs. 26 and 27, except for $Fe_{12}Nb$. The antiferromagnetic coupling of the local spin magnetic moments of the Cr and Zr atoms with the local spin magnetic moments of the Fe atoms in the $Fe_{12}Cr$ and $Fe_{12}Zr$ clusters is due to the somewhat higher occupation in the β-spin representation with respect to that in the α-spin representation as follows from the electronic configurations $(3d^{3.1}4s^{0.3}4p^{0.9})_\alpha(3d^{3.5}4s^{0.2}4p^{1.0})_\beta$ and $(4d^{1.0}5s^{0.3}5p^{0.2})_\alpha(4d^{1.6}5s^{0.25}5p^{0.2})_\beta$ of the Cr and Zr atoms, respectively. The reason for such distributions may be related to the following: the α-3d-subshells of iron atoms are fully occupied and these subshells are chemically inert; therefore, only β-3d-electrons can participate in the chemical bonding in the high-spin states of Fe_{13} and $Fe_{12}X$. As a consequence, the β-3d and β-4d occupations of the Cr and Zr atoms, respectively, are larger than the corresponding α-occupations in order to make stronger β-bonds.

Fig. 27 Geometrical structures of the lowest total energy states of Fe$_{12}$X (X = Gd and 4d-metal atoms). Bond lengths are in Å, local spin magnetic moments are in μ_B
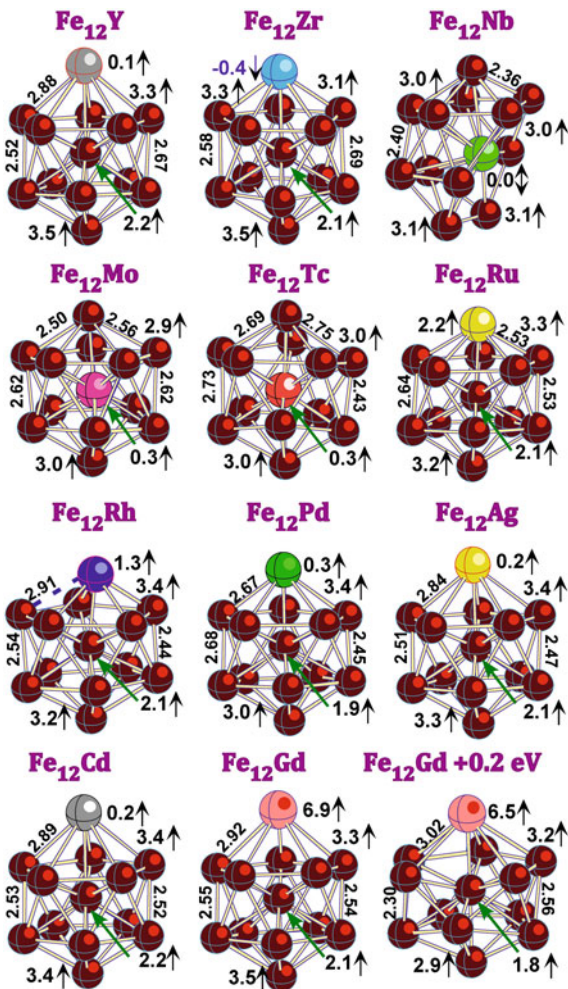
The first flip of the local spin magnetic moment of a Fe atom in Fe$_{13}$ occurs at the spin multiplicity $2S + 1 = 27$, and the difference in total energies between the corresponding ferrimagnetic state and the lowest total energy ferromagnetic state of Fe$_{13}$ is 1.48 eV. The spin multiplicities of the states corresponding to the first flip of the local spin magnetic moment on an atom and the energies computed as the differences in total energies of the corresponding ferrimagnetic and the lowest total energy states for all Fe$_{12}$X clusters considered are presented in Table 15. As can be seen, the flip spin multiplicities and the flip energies are similar to those found previously for the Fe$_{13}$ cluster in most cases. The notable exception is presented by the Fe$_{12}$Mo cluster, where the flip energy is only 0.21 eV. The first flip in the Fe$_{12}$X clusters always occurs on a Fe atom except for the clusters containing magnetic Co,

Table 15 The spin multiplicity and energy of the first flip of the local spin magnetic moment on an atom in the $Fe_{12}X$ clusters (X = Al, 3d, 4d, and Gd atoms)

$Fe_{12}X$, 3d series, and Al											
X	Sc	Ti	V	Cr	Mn	Fe	Co	Ni	Cu	Zn	Al
2S + 1, ground state	40	39	38	37	46	45	44	39	40	41	40
2S + 1, 1st flip	28	29	28	29	28	27	30	29	28	27	24
Δ^a	1.05	1.25	1.22	0.88	1.60	1.48	1.34	2.07	0.86	1.29	1.18
$Fe_{12}X$, 4d series, and Gd											
X	Y	Zr	Nb	Mo	Tc	Ru	Rh	Pd	Ag	Cd	Gd
2S + 1, ground state	40	39	38	37	36	43	42	39	40	41	47
2S + 1, 1st flip	28	29	28	29	28	29	30	29	28	27	35
Δ^a	1.11	0.61	1.03	0.69	0.98	1.56	1.44	0.67	1.21	1.27	1.11

$^a\Delta = E_{tot}$(1st flip) $- E_{tot}$(ground state). All Δ values are in eV

Ni, and Ru, along with Rh atoms (see Table 15). The first Fe flip in $Fe_{12}Gd$ occurs at a large spin multiplicity of 35.

A comparison of the total spins obtained for the $Fe_{12}X$ clusters considered is presented in Fig. 28. As may be seen, both $Fe_{12}Al$ and $Fe_{12}Sc$ clusters possess the same total spin, which is in line with the similarity of the AlO_n and ScO_n oxides noted previously [39]. The pairs of clusters in the 3d- and 4d-substituent series possess the same total spin except for the Mn–Tc, Fe–Ru, and Co–Rh pairs. The total spin of only two clusters, $Fe_{12}Gd$ and $Fe_{12}Mn$ is larger than that of Fe_{13}. However, a state of $Fe_{12}Mn$ with the geometrical structure corresponding to the center substitution is close in total energy to the one corresponding to a surface substitution. The former state has the same total spin of 17.5 as the lowest total energy state of $Fe_{12}Tc$.

A comparison of the total energies as well as the total spins obtained in our optimizations of the $Fe_{12}X$ clusters including central and surface substitutions of Fe is presented in Fig. 29 (Al and 3d-metal atoms) and Fig. 30 (Gd and 4d-metal
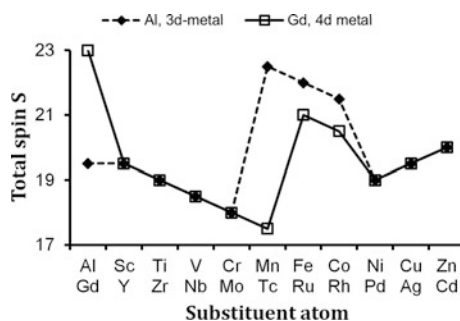
Fig. 28 Total spin of the lowest total energy states of $Fe_{12}Al$, $Fe_{12}Gd$, and $Fe_{12}X$ (X = 3d- and 4d-metal atoms)

Fig. 29 The difference in total energy of the states with the central and surface substitution (*the top panel*) and the corresponding total spin magnetic moments (*the bottom panel*) for Fe$_{12}$X (X = Al and 3d-metal atoms). The geometrical structure with the central Sc atom collapses during optimizations. Positive relative energies indicate that surface substitution is favored while negative energies indicate favorable central substitution
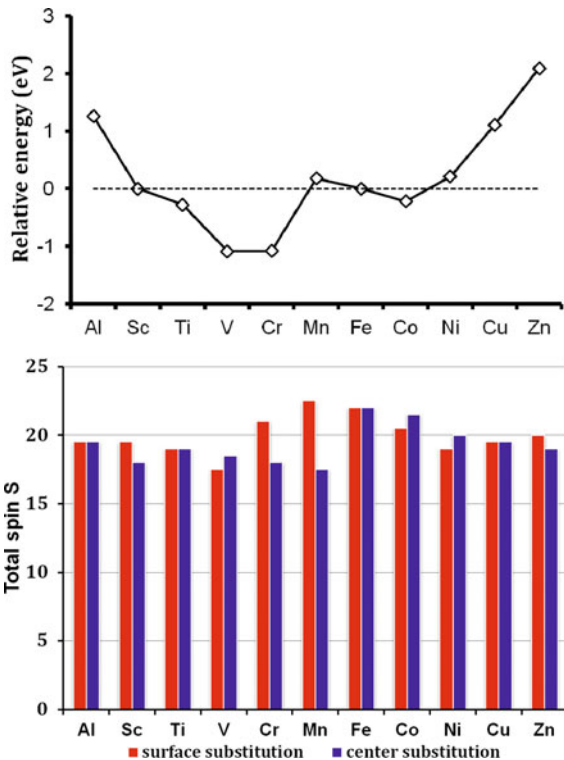
atoms). The differences in total energies that equal zero (at Sc, Gd, Y, Zr, Nb, and Cd positions in the figures) do correspond to the cases where initial geometrical structures with the center substitution collapse. The resulting geometrical structures are shown in Fig. 31.

The relative energies plotted in Figs. 29 and 30 are the differences in total energy $\Delta E = E_{tot}^{center} - E_{tot}^{surface}$ where the superscript denotes the substitution site. As can be seen in Fig. 26, the central substitution with V and Cr decreases the Fe$_{12}$V and Fe$_{12}$Cr total energies by ∼1 eV compared to those for their surface substitution. Especially strong preference for the surface substitution is found for Al and the electron-rich Cu and Zn, whereas the ΔE is small for all other members in this series. The total spin depends on the substitution site in all cases, except for Al, Ti, and Cu.

In the 4d-substituent series shown in Fig. 27, the central substitution is energetically more favorable than the surface substitution by −0.96 and −0.59 eV for Mo and Tc, respectively. The difference in total energies between the lowest total energy states with the surface and center substitution geometries grows rapidly beginning with the value of 0.64 eV for Fe$_{12}$Ru to the value of 3.8 eV for Fe$_{12}$Ag. The surface substitution in Fe$_{12}$Ru and Fe$_{12}$Rh brings a larger total energy gain with respect to that of the central substitution in Fe$_{12}$Mo and Fe$_{12}$Tc.

Fig. 30 The difference in total energy of the states with the central and surface substitution (*the top panel*) and the corresponding total spin magnetic moments (*the bottom panel*) for $Fe_{12}X$ (X = Gd and 4d-metal atoms). The geometrical structures with the central Y, Zr, Nb, Cd, and Gd atoms do collapse during optimizations. Positive relative energies indicate that surface substitution is favored while negative energies indicate favorable central substitution
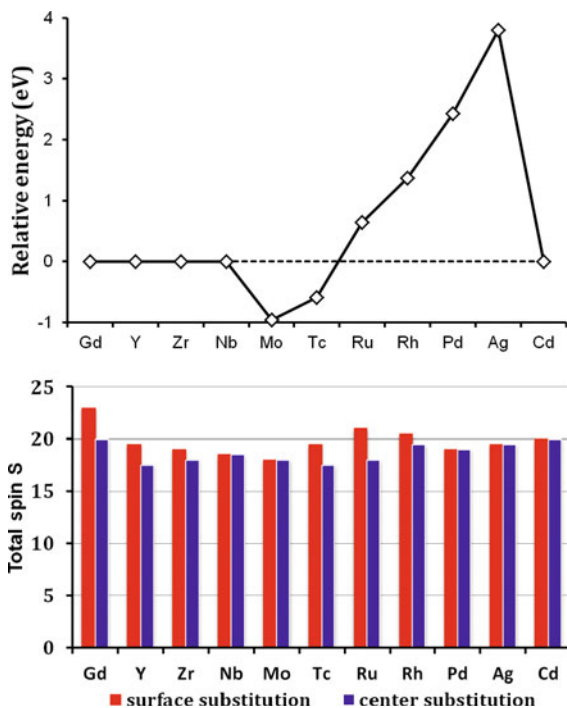
Fig. 31 Geometrical structures and total spins obtained in optimizations of geometrical structures with the central Fe atom substitution in $Fe_{12}Sc$, $Fe_{12}Y$, $Fe_{12}Zr$, $Fe_{12}Nb$, $Fe_{12}Cd$, and $Fe_{12}Gd$
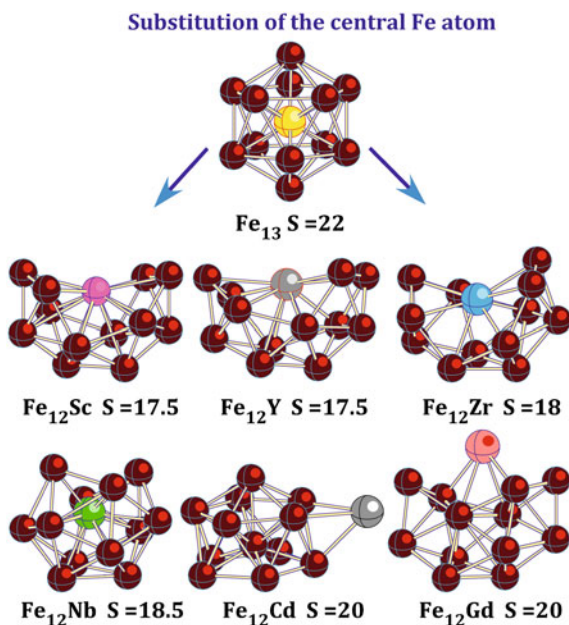
Table 16 Binding energies of X in $Fe_{12}X$ clusters (X = Al, 3d-, 4d-, and Gd atoms), binding energies of Fe–X (X = 3d atom) and atomization energies of the $Fe_{12}X$ clusters

X	Sc	Ti	V	Cr	Mn	Fe	Co	Ni	Cu	Zn	Al
3d-metal dimers											
$2S + 1$	2	1	2	3	10	7	6	5	4	5	4
Fe–X	3.19	4.10	2.86	1.17	1.57	2.18	2.42	2.51	1.56	0.38	2.00
$Fe_{12}X$, 3d series, and Al											
$2S + 1$	40	39	38	37	46	45	44	39	40	41	40
Fe_{12}–X	4.39	4.78	4.85	3.08	3.49	3.79[a]	3.90	3.65	2.69	1.40	3.91
E_{atom}	2.99	3.02	3.03	2.89	2.89	2.94	2.95	2.93	2.86	2.76	2.95
$Fe_{12}X$, 4d series, and Gd											
X	Y	Zr	Nb	Mo	Tc	Ru	Rh	Pd	Ag	Cd	Gd
$2S + 1$	40	39	38	37	36	43	42	39	40	41	47
Fe_{12}–X	4.55	5.82	5.57	4.47	5.00	5.02	4.72	3.54	2.20	1.02	3.65
E_{atom}	3.00	3.10	3.08	3.00	3.04	3.04	3.02	2.93	2.82	2.73	2.93

All values are in eV

[a]Experimental values are 4.11 ± 0.37 (see Ref. [40]) and 4.32 ± 0.15 (see Ref. [41])

The Fe_{12}–X binding energies and atomization energies of the $Fe_{12}X$ clusters are presented in Table 16 where they are compared to the Fe–X binding energies in the FeX dimers (X = Al, 3d-metal atoms) and to the Fe_{12}–Fe binding energy in the lowest total energy state of the Fe_{13} cluster. The energy of an X atom abstraction from a $Fe_{12}X$ cluster is computed as

$$D_0(Fe_{12}-X) = E_{tot}^{el}(Fe_{12}) + E_0(Fe_n) + E_{tot}(Fe) - \left[E_{tot}^{el}(Fe_{12}X) + E_0(Fe_{12}X) \right]$$
(12)

and the atomization energy of a $Fe_{12}X$ cluster is computed as

$$E_{atom}(Fe_{12}X) = \left[E_{tot}^{el}(Fe_{12}X) + E_0(Fe_{12}X) - 12E_{tot}(Fe) - E_{tot}(X) \right]/13 \quad (13)$$

In the first $Fe_{12}X$ series (X = Al and 3d-metal atoms), the Fe–X binding energy for X = Sc, Ti, V, Co and Al is larger than the Fe_{12}–Fe binding energy in the Fe_{13} cluster. The binding energies of Sc, Ti, V, Co, and Ni in the FeX dimers are larger than the Fe–Fe binding energy in the Fe_2 dimer, whereas the binding energy of Al is somewhat smaller. As expected, the atomization energies in this series possess the same trend as the Fe–X binding energies, although the differences between the atomization energies of $Fe_{12}X$ and the atomization energy of the Fe_{13} cluster are much smaller than the differences in the binding energies. The binding energies of an X atom in the $Fe_{12}X$ clusters are appreciably larger than in the corresponding dimers because of a higher coordination. Experimental measurements have been done for the Fe_{12}–Fe binding energy using mass spectrometry and the values obtained are presented in Table 16. As may be seen, our computed value compares fairly well with experimental values when the experimental uncertainty bars are taken into account.

In the second $Fe_{12}X$ series (X = Gd and 4d-metal atoms), the binding energies of all X atoms but Pd, Ag, and Cd are larger than the corresponding binding energies in the first series. The largest and smallest binding energies in both series belong to $Fe_{12}Zr$ and $Fe_{12}Cd$, respectively. Except for $Fe_{12}Ag$ and $Fe_{12}Cd$, the atomization energies in the second series are larger than the atomization energy of the Fe_{13} cluster, and they are also larger than the atomization energies of the corresponding 3d-counterparts. The $Fe_{12}Pd$ atomization energy is only marginally smaller than that of Fe_{13}. The Fe_{12}–Gd binding energy is the third largest one in the both series and is substantially higher than the Fe_{12}–Fe binding energy.

In summary, one may point out that (1) the total spin magnetic moment of all the $Fe_{12}X$ clusters is smaller than the total spin magnetic moment of the parent Fe_{13} cluster except for $Fe_{12}Mn$ and $Fe_{12}Gd$, and (2) The $Fe_{12}X$ clusters where X = Al, Sc, Ti, V, Co, Y, Zr, Nb, Mo, Tc, Ru, Rh, and Gd are more stable than the Fe_{13} cluster with respect to an atomic abstraction.

9   Doping of Iron Clusters with a Gd Atom

Clusters composed of both transition metal (TM) and lanthanide atoms present a special interest because they are expected to possess total spin magnetic moments per atom which are larger than the total spin magnetic moments per atom of the TM nanoparticles. A Gd atom with the $(4f^7 5d^1 6s^2)$ valence electron configuration possesses a large total spin magnetic moment owing to its half-filled 4f shell. The Gd bulk is ferromagnetic with the total magnetic moment of 7.83 μ_B per atom and a Curie temperature of $T_C \sim 293$ K, which is close to ambient temperature. Because Gd-containing alloys exhibit large magnetocaloric effects, they are prospective materials for fabricating magnetic refrigerators, which can operate at room temperature.

As concerns unary Gd nanoparticles, they are highly pyrophoric, spontaneously igniting immediately and quite spectacularly upon exposure to air. In order to prevent violent reactions with air, the nanoparticles can be coated with non-reactive metals, such as gold. Another way of decreasing the reactivity might be related to the fabrication of nanoparticles containing a mixture of Gd and nd-metal atoms. Such nanoparticles could possess both high magnetic moments and significantly reduced reactivity. Naturally, the best candidates of initial clusters, which have already high total magnetic moments, are iron clusters. The smallest iron cluster which contains a central atom is Fe_{13} and the largest cluster optimized above is Fe_{20}. We have additionally optimized the Fe_{21} cluster. The latter cluster with the central atom removed has been used as a shell cluster for the Gd doping.

For each $Fe_{n-1}Gd$ cluster, we tested [42] several geometric structures where a Gd atom replaces a central or surface atom in a Fe_n cluster and three cage geometrical structures. In the cages, a Gd atom substitutes for an iron atom in 4-, 5-, and 6-coordinate sites of the geometrical structure corresponding to the lowest total
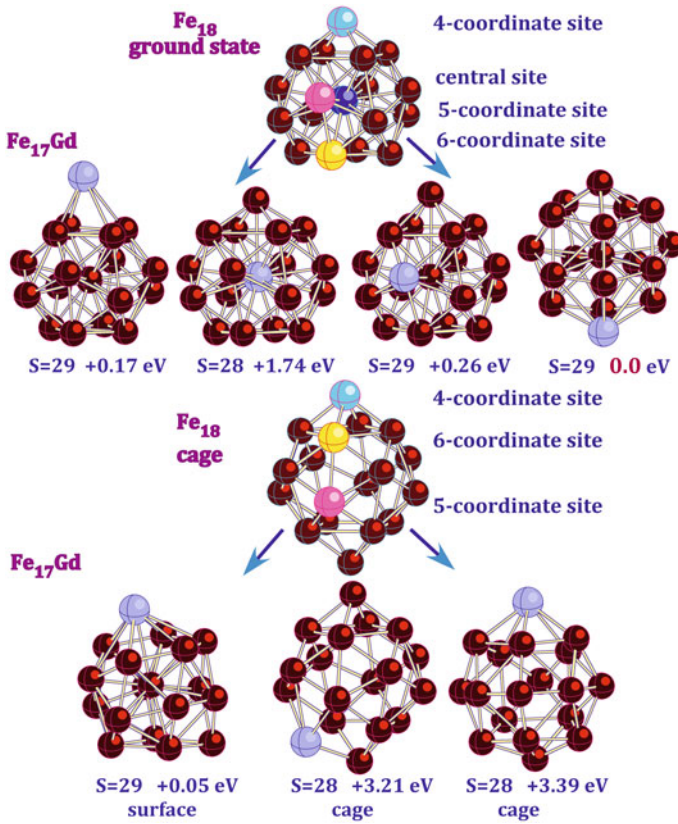
Fig. 32 Non-equivalent substitution sites for Gd in the Fe_{18} cage and non-cage geometrical structures along with the optimized $Fe_{18}Gd$ structures obtained. S denotes the total spin, the energy shifts are given with respect to the lowest total energy ($S = 29$, 0.0 eV)

energy of the Fe_{n+1} cluster with a removed central atom. As a typical example, trial geometries and the optimized structures of $Fe_{17}Gd$ are shown in Fig. 32. As may be seen, the structure of the lowest total energy state corresponds to the Gd substitution for a 6-coordinate surface Fe atom of Fe_{18}. The states with 4- and 5-coordinate substitutions are higher in total energy by 0.26 and 0.17 eV, respectively. The central substitution is energetically unfavorable and the corresponding state is higher in total energy than the lowest total energy state by 1.74 eV.

The lowest total energy states obtained for the Fe_nGd clusters for $n = 12$–15 and $n = 16$–19 are presented in Figs. 33 and 34, respectively. As may be seen, the Gd atom prefers the surface substitution for $n = 12$–18, whereas the substitution of a surface atom in Fe_{21} with one of two equivalent internal atoms removed results in the formation of a Gd–Fe_{19} dimer where the geometrical structure of the Fe_{19} moiety is different from that in the lowest energy state of the Fe_{19} cluster shown in Fig. 18. The Fe–Fe bond lengths in the Fe_nGd clusters are similar to those in the Fe_{n+1}

Fig. 33 Geometrical
structures of the lowest total
energy states of Fe$_n$Gd for
$n = 12$–15. S denotes the total
spin, bond lengths are in Å,
local spin magnetic moments
are in μ_B

Fe$_{12}$Gd S = 23   Fe$_{13}$Gd S = 24

Fe$_{14}$Gd S = 26   Fe$_{15}$Gd S = 27
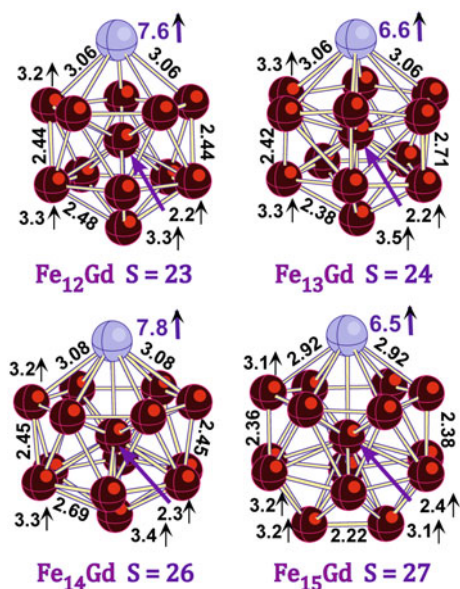
Fig. 34 Geometrical
structures of the lowest total
energy states of Fe$_n$Gd for
$n = 16$–19. Bond lengths are
in Å and local spin magnetic
moments are in μ_B, S denotes
the total spin

Fe$_{16}$Gd S = 28   Fe$_{17}$Gd S = 29

Fe$_{18}$Gd S = 30   Fe$_{19}$Gd S = 31
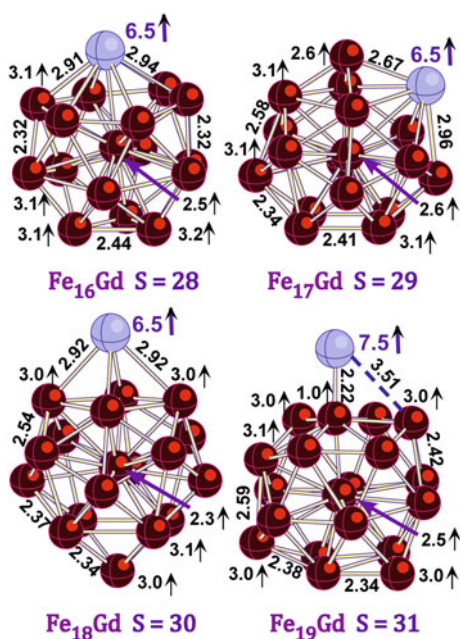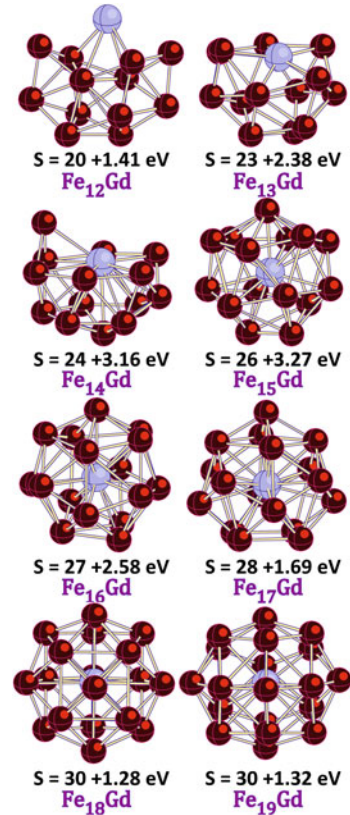
clusters and have variations from 2.2 to 2.7 Å, whereas the Fe–Gd bond lengths vary
from 2.6 to 3.1 Å, except for the Fe$_{18}$Gd cluster where R(Fe–Gd) = 2.22 Å
(see Fig. 34).

The geometrical structures and total spins obtained in optimizations of states with the central Gd substitution are shown in Fig. 35. The Gd atom breaks the iron shell and becomes a surface atom for $n = 12$–14 whereas it stays in the center of larger clusters. The total energy difference between the lowest total energy states and the states whose geometrical structures are presented in Fig. 35 decreases from 3.27 eV at $n = 15$ to 1.32 eV at $n = 19$.

Figure 36 compares the total spin obtained for the lowest total energy states of the Fe_nGd clusters (whose geometrical structures are presented in Figs. 33 and 34) and the total spin of the states corresponding to the central Gd substitution in Fig. 35 to the total spin of the bare Fe_n clusters. The total spin of a Fe_nGd cluster in its lowest total energy state is larger by one than that of the Fe_{n+1} cluster, except for $Fe_{14}Gd$ whose total spin is larger by two. In the latter case, an increase in the total spin magnetic moment per atom is $\sim 4/15 \ \mu_B$ from 3.2 μ_B in the Fe_{15} cluster to 3.47 μ_B in the $Fe_{14}Gd$ cluster. The Fe_nGd clusters with the central Gd atom ($n = 15$–19) possess the same total spin as the Fe_{n+1} clusters, except for the $Fe_{18}Gd$ cluster, where the total spin magnetic moment per atom has an increase of 0.11 μ_B with respect to that of the Fe_{19} cluster.

Fig. 35 Geometrical structures of $Fe_{12}Gd$–$Fe_{19}Gd$ obtained in optimizations beginning with the trial structures where a Gd atom substitutes for the central atom in the structures presented in Figs. 16, 17, and 18. S denotes the total spin; the total energy shifts are given relative to the lowest total energy states presented in Figs. 33 and 34

S = 20 +1.41 eV
$Fe_{12}Gd$

S = 23 +2.38 eV
$Fe_{13}Gd$

S = 24 +3.16 eV
$Fe_{14}Gd$

S = 26 +3.27 eV
$Fe_{15}Gd$

S = 27 +2.58 eV
$Fe_{16}Gd$

S = 28 +1.69 eV
$Fe_{17}Gd$

S = 30 +1.28 eV
$Fe_{18}Gd$

S = 30 +1.32 eV
$Fe_{19}Gd$

Fig. 36 Total spin of the Fe_n and $Fe_{n-1}Gd$ clusters for $n = 13–20$: (*a*) bare Fe_n; (*b*) the lowest total energy $Fe_{n-1}Gd$; (*c*) with the central substituted Gd atom
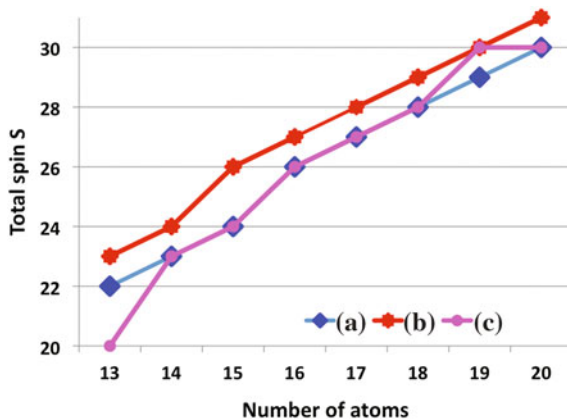
As may be seen from Figs. 33 and 34, the total spin magnetic moment of Gd is substantially larger than the total spin magnetic moment of Fe atoms, and it varies from the maximal value of 7.8 μ_B in the $Fe_{14}Gd$ cluster to the minimal value of 6.5 μ_B in the $Fe_{15}Gd$, $Fe_{17}Gd$, and $Fe_{18}Gd$ clusters. The $Fe_{14}Gd$ cluster presents the only case where the difference of $\sim 4 \, \mu_B$ between the total spin magnetic moments of the Gd and iron atoms results in the same difference between the total spin magnetic moments of the $Fe_{14}Gd$ and Fe_{14} clusters. In all other cases, the increase in the local spin magnetic moment due to the Gd substitution is partially compensated by a small decrease in the Fe local spin magnetic moments and the increase in the total spin magnetic moment of the substituted cluster is 2 μ_B.

In order to gain insight into the relative thermodynamic stability of the Fe_n and $Fe_{n-1}Gd$ clusters when n ranges from 13 to 20, we compare the Fe_n–Fe, $Fe_{n-1}Gd$–Fe, and $Fe_{n-2}Gd$–Fe binding energies as well as the binding energies per atom in the Fe_n and $Fe_{n-1}Gd$ clusters. The energy D_0 of an X atom abstraction from a cluster is defined as

$$D_0(Fe_n-Fe) = E_{tot}^{el}(Fe_{n-1}) + E_0(Fe_{n-1}) + E_{tot}(Fe) - \left[E_{tot}^{el}(Fe_n) + E_0(Fe_n)\right] \quad (14)$$

$$D_0(Fe_nGd-X) = E_{tot}^{el}(Fe_{n-1}X) + E_0(Fe_{n-1}X) + E_{tot}(X) \\ - \left[E_{tot}^{el}(Fe_nGd) + E_0(Fe_nGd)\right] \quad (15)$$

where E_{tot}^{el} is the Born-Oppenheimer total energy, X = Fe or Gd, and E_0 denotes the zero point vibrational energies computed in the harmonic approximation. The binding energies E_b per atom is computed as

$$E_b(Fe_nX) = [E_{tot}^{el}(Fe_nX) + E_0(Fe_nX) - nE_{tot}(Fe) - E_{tot}(X)]/(n+1) \quad (16)$$

As it follows from Table 17, the $Fe_{n-1}Gd$–Fe binding energy is somewhat smaller than the Fe_n–Fe binding energy at a given n, except for $n = 14$ and 19, whereas the $Fe_{n-1}Gd$–Gd binding energies are smaller than the $Fe_{n-1}Gd$–Fe

Table 17 Comparison of the binding energy of a Fe atom in the Fe_n and $Fe_{n-1}Gd$ clusters with the binding energy of a Gd atom in the $Fe_{n-1}Gd$ cluster along with the binding energy per atom in the Fe_n and $Fe_{n-1}Gd$ series

n	13	14	15	16	17	18	19	20
Binding energy of a single atom								
$D_0(Fe_{n-1}Gd–Fe)$	…	3.57	4.16	3.39	3.34	3.19	4.04	2.78
$D_0(Fe_{n-1}Gd–Gd)$	3.65	3.43	4.11	3.14	2.95	2.64	3.05	2.38
Binding energy per atom								
$E_b(Fe_n)$	2.94	2.98	3.08	3.10	3.13	3.14	3.16	3.16
$E_b(Fe_{n-1}Gd)$	2.93	2.98	3.06	3.08	3.09	3.10	3.13	3.12

All values are in eV

binding energies for all n values. The behavior of binding energies in all three series is similar; namely, the D_0 energy decreases beginning with $n = 15$ and have a bump at $n = 19$.

The binding energies E_b per atom in the $Fe_{n-1}Gd$ clusters are smaller by up to 0.04 eV than the corresponding binding energies in the Fe_n clusters. This indicates that a single Gd-substitution destabilizes the iron cluster. An indirect confirmation of the destabilization provides the expelling of the Gd atom to the surface in the geometrical configurations of the lowest total energy states of the clusters shown in Figs. 33 and 34.

On the whole, one may summarize the main conclusions with respect to modifications of total spin magnetic moments of iron clusters by a single Gd-substituent as follows: (1) a total spin magnetic moment of a Fe_nGd cluster is higher by 2 μ_B compared to that of the Fe_{n+1} cluster for a given n value, except for $Fe_{14}Gd$ whose total spin magnetic moment is larger by 4 μ_B than the total spin magnetic moment of the Fe_{15} cluster; (2) the local spin magnetic moments of iron atoms in the substituted Fe_nGd clusters match those in non-substituted Fe_{n+1} clusters within 0.1 μ_B, whereas a local spin magnetic moment of the Gd atom varies from the maximal value of 7.8 μ_B in the $Fe_{14}Gd$ cluster to the minimal value of 6.5 μ_B in the $Fe_{15}Gd$, $Fe_{17}Gd$, and $Fe_{18}Gd$ clusters.

10 Iron Oxide Isomers of $(FeO)_{12}$ and Superexchange Mechanism in $(FeO)_2$

Iron oxide clusters have been the subject of numerous experimental and theoretical studies because of their importance in technological applications, including those described in Sects. 3 and 4. The geometrical and electronic structure of $(FeO)_n$ clusters have been previously studied [43, 44] for $n = 2$–10, 12 and it was found that geometrical configurations of the clusters do not mimic the bulk FeO lattice. Instead, the cage-like geometrical configurations, called drums and towers, have been found to be the preferred cluster configurations. The ground-state geometrical structure of Fe_{12} is an icosahedron with one removed vertex. Therefore, the

geometrical structure of the lowest total energy state of $(FeO)_{12}$ can correspond to oxygen chemisorption on the surface of Fe_{12} or to the formation of cage structures.

The ground state of Fe_{12} is ferromagnetic with the spin multiplicity of 37 which corresponds to the total spin magnetic moment of 36 μ_B; however, oxidation can result in ferrimagnetic states or can raise the spin multiplicity of Fe_{12}; therefore, one should optimize each trial geometrical configurations in a wide $2S + 1$ range. Optimizations of $(FeO)_{12}$ geometrical structures have been performed [45] in the range of $1 \leq n \leq 45$ with the set of trial geometrical structure presented in Fig. 37.

Total energies of ferrimagnetic states are found to be generally lower than the total energies of ferromagnetic states as may be observed in Fig. 38. There are four lowest total energy states with $2S + 1 = 3, 9, 15,$ and 23, which are nearly degenerate in total energy. It is interesting to note that there is only a small change in the total energy values when the spin multiplicity decreases from $2S + 1 = 45$ to $2S + 1 = 1$. The majority of total energy values is enclosed within a quite narrow interval, and the total energy variation is within 2.35 eV over the whole range of different structures and spin multiplicities. When moving to lower spin multiplicities, the cluster geometries were changing the shape they had in the initial states with $2S + 1 = 37$. Eventually, all seven series from A to F ended up at low spin multiplicities with two structure types: chemisorbed $Fe_{12}O_{12}$ and T_h-type cage $(FeO)_{12}$. The reason why there is no exact convergence to these two states at

Fig. 37 Trial geometrical configurations of $Fe_{12}O_{12}$ used when starting optimizations from the high spin multiplicity side and the optimized configurations obtained for the corresponding states with $2S + 1 = 37$
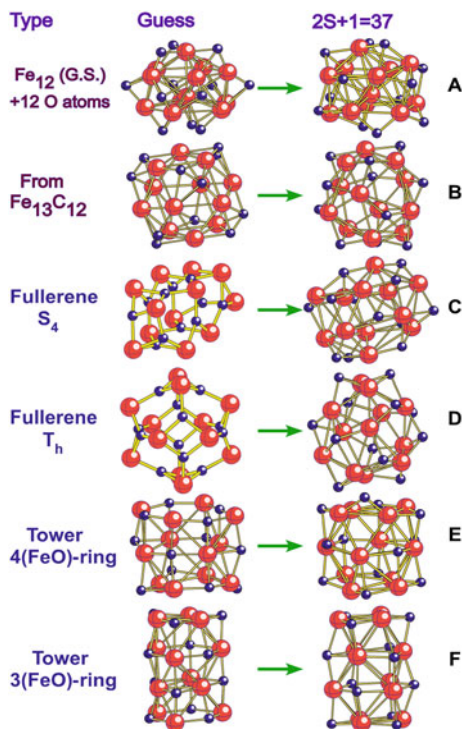
Fig. 38 Total energy (in a. u.) as a function of spin multiplicity for the clusters labeled A–F in Fig. 37. The cluster A with a Fe core has the lowest energy structure corresponding to spin multiplicity $2S + 1 = 3$
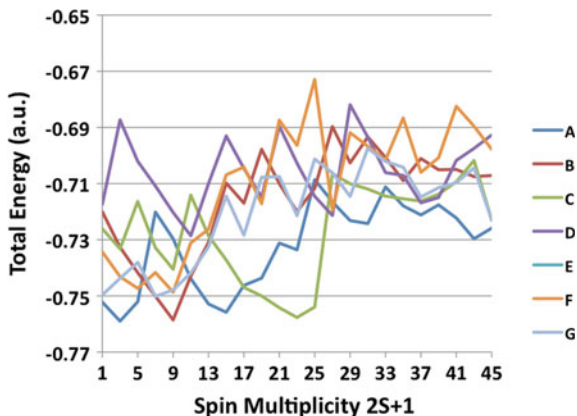
$2S + 1 = 1$ in Fig. 38 is related with a large number of possible local spin flips in ferrimagnetic states which possess slightly different total energies.

The geometrical structures and total spin magnetic moments of atoms for these two types of clusters are presented in Fig. 39 for their lowest total energy states, all of which are ferrimagnetic. As may be seen, the $Fe_{12}O_{12}$ triplet state is only marginally below the nonet state of $(FeO)_{12}$. It is worth noting that the symmetric cage structure of a bare Fe_{12} cluster, which corresponds to the geometrical configuration of the ground-state Fe_{13} cluster without the central atom, does not correspond to the lowest total energy excited state of Fe_{12} as can be seen from Fig. 40.

Figure 41 visualizes geometrical changes caused by oxidation of Fe_{12}, where all structures are presented on the same scale. As is seen, the $(FeO)_{12}$ cage formation results in a larger cluster size increase than in the case of surface chemisorption.

Comparison of the local spin magnetic moments of the $Fe_{12}O_{12}$ and $(FeO)_{12}$ clusters in Fig. 39 with those of Fe_{12} in Fig. 40 shows that the sizes of the local spin magnetic moments are quite similar in both oxidized and bare iron clusters. This assumes that a local spin magnetic moment flipping results in about the same occupation of α- and β-spin representation in the inverse order $\alpha \rightarrow \beta$ and $\beta \rightarrow \alpha$. That is, the oxygen valence orbitals do form similar bonds with the iron valence orbitals independent of the direction of the local spin magnetic moment on iron atoms.

The total effective valence electronic configuration of oxygen atoms corresponds on average to $(2s^{1.75}2p^{5.0})$ with nearly the same occupation of α- and β-AOs. In the majority of ferrimagnetic states of $Fe_{12}O_{12}$ and $(FeO)_{12}$, oxygen atoms possess small excess spin densities which are mostly around ± 0.1 e and in a few cases increase up to 0.4 e. In the ferromagnetic states, the total effective valence electronic configurations of oxygen atoms on average correspond to $(2s^{1.70-1.77}2p^{4.80-5.00})$ and oxygen atoms possess excessive spin majority densities of 0.2–0.3 e. In bare Fe_{12}, the difference between total energies of the antiferromagnetic singlet state and the ground $2S + 1 = 37$ state is 1.30 eV. In $Fe_{12}O_{12}$ and $(FeO)_{12}$, the order of total energies is inverted and the difference between total energies of the lowest total

**Fig. 39** The lowest total energy isomers of $Fe_{12}O_{12}$. M denotes the multiplicity $2S + 1$, bond lengths are in Å, and the local spin magnetic moments are in μ_B
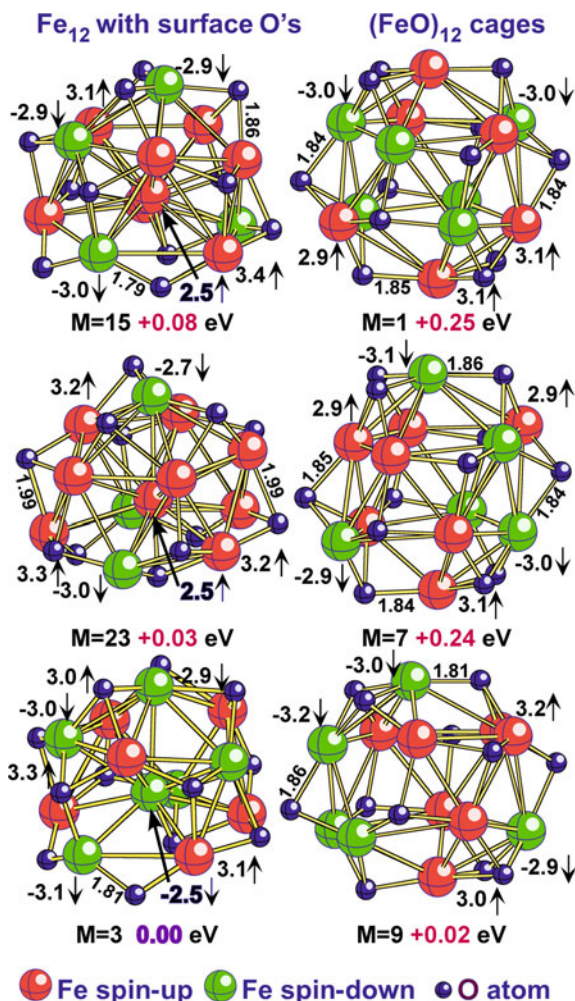

energy ferromagnetic $2S + 1 = 37$ and ferrimagnetic triplet states is -1.03 eV. The total energy decreases in all series when moving from ferromagnetic to ferrimagnetic states.

In order to gain insight as to why oxidation of Fe_{12} leads to ferrimagnetic lowest total energy states, we analyze the bonding patterns in Fe_2O_2 whose ground state is found to be an antiferromagnetic singlet. The states $^1B_1(C_{2v})$ and $^7B_{2u}(D_{2h})$ in Fig. 42 are found to have the same total energies as the corresponding states obtained in the unconstrained optimizations. Note, that the formal symmetry of the singlet state geometrical configuration is also D_{2h} as for the septet state. However, the singlet wave function symmetry reduces to C_{2v} because the iron atoms are non-equivalent due to the antiferromagnetic coupling of their total spin magnetic moments.

Fig. 40 The lowest total energy isomers of Fe$_{12}$. $M = 2S + 1$, bond lengths are in Å, and local spin magnetic moments are in μ_B
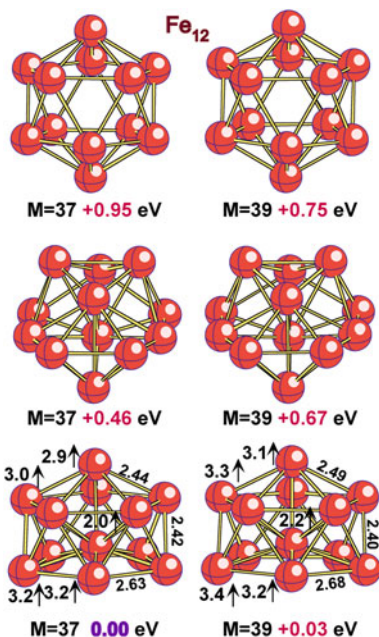
Fig. 41 Comparison of geometrical structures of Fe$_{12}$ before and after oxidation
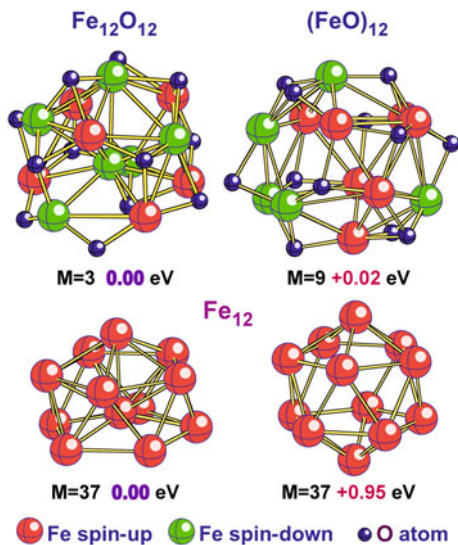
Comparison of the NAO populations shows that the total electronic effective atomic configurations are quite similar in both $^1B_1$ and $^7B_{2u}$ states. The α- and β-AO populations in these states are also similar after the α ⇔ β inversion of the Fe occupation in the $^1B_1$ state. This inversion is responsible for the different bonding

Fig. 42 Sketch of chemical
bonding in the
antiferromagnetic singlet and
ferromagnetic septet states of
Fe_2O_2
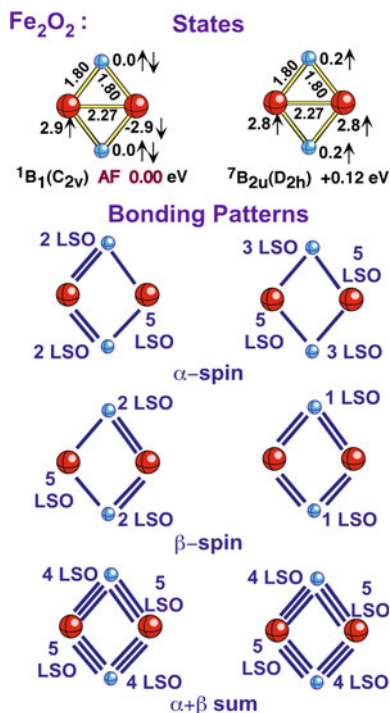
and LSO patterns, which are schematically shown in Fig. 42, in the $^1B_1$ and $^7B_{2u}$ states. In the $^1B_1$ state, the Fe_I effective electronic α-configuration is $(4s^{0.13}3d^{1.91}4p^{0.09})$ and corresponds to the formation of a single LSO and two bonding orbitals of Fe_I with both oxygen atoms, whereas the α-configuration $(4s^{0.15}3d^{4.75}4p^{0.12})$ of Fe_{II} corresponds to two single bonds of Fe_{II} and four LSOs. The bonding and LSO patterns in the β-spin representation present the mirror image of the α-patterns. Both oxygens possess two LSOs in each spin representation.

On the contrary, the bonding patterns in different spin representations are asymmetric in the $^7B_{2u}$ state. There are four single Fe–O and sixteen LSOs in the α-spin representations and four Fe = O double bonds and 2 LSOs in the β-spin representation. The total α + β bonding and LSO patterns are the same in both the $^1B_1$ and $^7B_{2u}$ states. The reason for the singlet state being lower in total energy than the septet state by 0.12 eV can be related to the larger number of α-LSOs in the septet state. The mutual (Pauli) repulsion of a larger number of LSOs is to be responsible for the total energy increase.

In summary, one can conclude that there is no appreciable difference in total energy between the states whose geometrical configurations correspond either to the absorption of oxygen atoms on the surface of the ground-state Fe_{12} cluster or to the formation of hollow $(FeO)_{12}$ cages. Unlike carbon chemisorption on the Fe_{13} surface considered in the next Section, no formation of O_2 dimers on the Fe_{12} surface was observed. Oxidation of the ground-state Fe_{12} cluster almost completely

quenches its total spin magnetic moment and the lowest total energy state of $Fe_{12}O_{12}$ is a triplet. The lowest total energy state with a cage geometrical configuration is a nonet and this state is only marginally higher in total energy than the $Fe_{12}O_{12}$ triplet.

11   Interaction of Iron Clusters with Carbon Atoms and Carbon Monoxide

Here, we extend consideration of interactions of a single carbon atom and a single CO molecule with iron clusters to interactions of a large number of carbon atoms or a larger iron cluster size. First, we compare interactions of three C atoms and three CO molecules with a ground-state Fe_4 cluster [46]. The optimized geometrical structures of the lowest total energy states of the neutral and singly positively and negatively charged Fe_4C_3 and $Fe_4(CO)_3$ clusters are presented in Fig. 43. In the Fe_4C_3 series, two carbon atoms prefer to form a dimer independent of charge and the total spin is somewhat quenched with respect to that of the corresponding Fe_4 species.

None of the carbon monoxide molecules dissociate on the iron cluster independent of the cluster charge, however, they quench the total spin of Fe_4 even to a
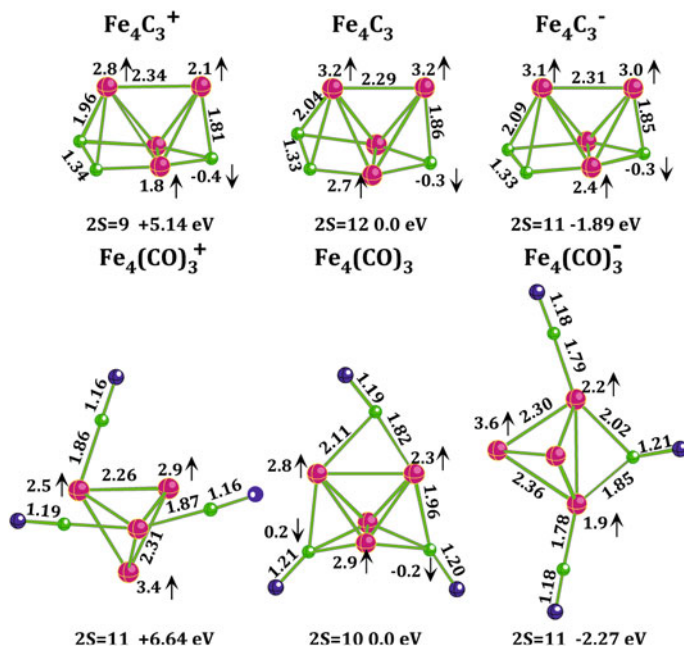

Fig. 43 Structures of the ground states of $Fe_4C_3^{+/0/-}$ and $Fe_4(CO)_3^{+/0/-}$

larger extent than carbon atoms. The Boudouard disproportionation reaction $Fe_4(CO)_3 + 3CO \rightarrow Fe_4C_3 + 3CO_2$ is only slightly endothermic by +0.17 eV. Since interactions of CO feedstock with $Fe_4C_m(CO)_n$ should eliminate oxygen via the Boudouard reaction, we consider [47] the trends in rearrangements of carbon atoms in the Fe_4C_n clusters, $n = 7$–15. Figure 44 shows isomers of Fe_4C_7, $Fe_4C_7^-$, and $Fe_4C_7^+$. As may be seen in the figure, the lowest energy isomers are nonplanar and contain a ring formed by C_3, C_4, and two iron atoms. The corresponding AF isomers have similar geometrical structures and are placed in total energy by ~ 0.5 eV above, while an isomer of Fe_4C_7 in which C_4 is replaced by a C_3 triangle plus a C atom is significantly higher. Attachment of two carbon chains decreases the spin multiplicity of Fe_4 and Fe_4^-, whereas it does not change the spin multiplicity of Fe_4^+. Similar behavior of the spin multiplicities is found for carbon attachments in Fe_4C_n for $n > 7$.

The geometrical structures of the ground states of Fe_4C_8 and its ions have similar rings as those in the ground states of Fe_4C_7, where the C_3 ring is replaced by a C_4 ring. The spin multiplicity of Fe_4C_8 and $Fe_4C_8^-$ are the same as in Fe_4C_7 and $Fe_4C_7^-$, respectively, whereas the ground state of the $Fe_4C_8^+$ cation is ferrimagnetic and its spin multiplicity is $2S + 1 = 5$. This trend continues in the Fe_4C_9 series. The
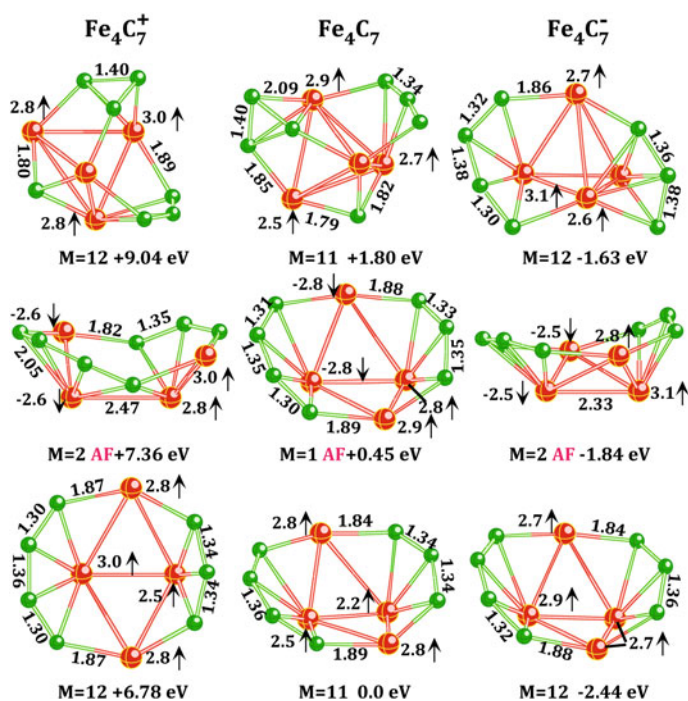
Fig. 44 Bond lengths are in Å and local spin magnetic moments are in μ_B, M is the spin multiplicity $2S + 1$. "AF" denotes a state where local spin magnetic moments are coupled antiferromagnetically

geometrical structure of the lowest total energy state of neutral Fe_4C_9 is presented in Fig. 45 and possesses a chair-type topology.

In order to form Fe_4C_{10}, an additional carbon atom attaches to the C_5 chain of Fe_4C_{11}, whereas the attachment of the next carbon atom leads to the formation of a C_{11} ring attached to a Fe_3 face in Fe_4C_{11}. Note, that a state of Fe_4C_{10} with a geometrical structure where a C_{10} ring is attached to a Fe_3 face is higher in total energy by +1.86 eV than the isomer shown in Fig. 45. In the lowest total energy state of Fe_4C_{16}, the geometrical structure contains a carbon C_{16} ring attached to a Fe_3 face.
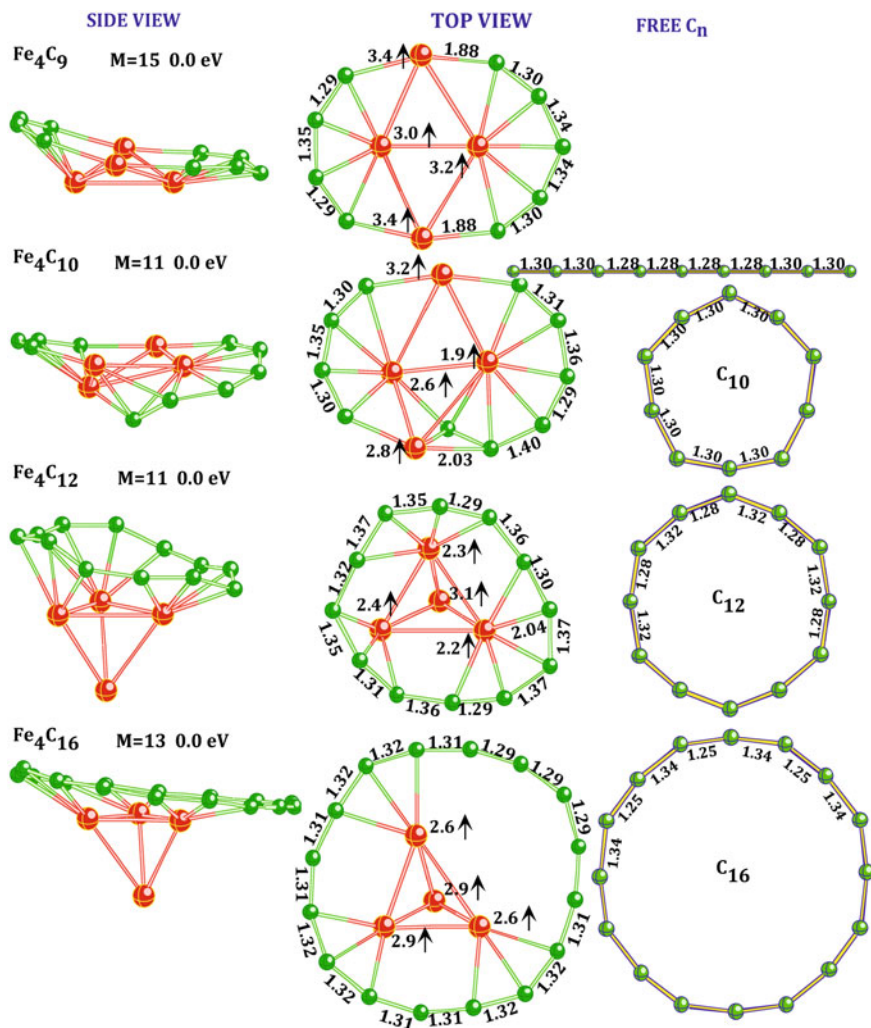
Fig. 45 Geometrical structures of the ground states of neutral Fe_4C_n and C_n. Bond lengths are in Å and local spin magnetic moments are in μ_B, M is the spin multiplicity $2S + 1$

The dependence of total energies of Fe_4C_n on a spin multiplicity is rather weak. Thus, the difference in total energies of Fe_4C_7 isomers when moving from the lowest $2S + 1 = 13$ state to the lowest $2S + 1 = 1$ state is 1.00 eV, that is, the same as in the bare iron cluster Fe_4 [48]. An even smaller difference of 0.5 eV is found for the Fe_4C_{12} series.

Figure 45 also shows the ground states of the corresponding neutral C_n species optimized at the same level of theory. In agreement with experiment, we found that the ground-state C_n are linear for $n = 3$–9 and have ring structures of C_{2v}, C_{2h}, or C_s symmetry for $n = 10$–20. In accordance with the geometrical shape change in C_n at $n = 10$, the carbon atoms form dimers, trimers, tetramers and pentamers in Fe_4C_n for $n = 4$–9, a tetramer and a hexamer in intermediate Fe_4C_{10}, and rings beginning with $n = 11$.

As the next step in studying chemisorptions of carbon by iron clusters, we considered [49] a larger Fe_{13} cluster with slightly distorted I_h symmetry in its ground state because it possesses practically equivalent faces. In order to trace the chemisorption patterns, we started with a single carbon atom and added carbon atoms one by one until their total number reached 20, which is the number of triangular faces in the Fe_{13} cluster.

The geometrical configurations corresponding to the $Fe_{13}C_n$ states with different chemisorbed carbon topologies are presented in Fig. 46 for $n = 0$–6. The pattern symbol denotes the type of bonded carbon groups and/or single atoms on the iron cluster surface. For example, "211" means that there is one C_2 dimer and two single C atoms. The bond lengths shown for species with $n = 0$–3 are rather typical for the rest of the clusters: the Fe–Fe, Fe–C and C–C bond lengths are in the range of 2.4–2.8, 1.8–2.0, and 1.35–1.45 Å, respectively.

The first carbon atom attaches to the center of one of the 20 faces of Fe_{13} and the second and third carbon atoms attach in such a way as to form a carbon dimer and trimer, respectively. The $2S + 1 = 41$ state of $Fe_{13}C_2$ with two separated C atoms is above by 1.17 eV, whereas the $2S + 1 = 39$ states of $Fe_{13}C_3$ with a carbon dimer and a single atom and three separated C atoms are above by 0.37 and 0.74 eV, respectively. One might extrapolate that the next carbon atom attaches in such a way as to form a 4-atom chain, but it is not so. The lowest energy state of $Fe_{13}C_4$ corresponds to a "dimer + 2 singles" configuration of carbon atoms which followed in total energy by the state whose carbon pattern is "22", whereas the state with a 4-member chain is above by 1.09 eV. A rather large separation in total energy of the "211" and "22" states can be related to a higher bonding ability of surface iron atoms of Fe_{13} which are not involved in bonding with previously chemisorbed carbon species. Thus, one can conclude that there is competition between the formation of a C–C bond with a chemisorbed carbon species and the bonding to iron atoms.

Let us consider in detail why the C_2 dimer formation is energetically preferable over the chemisorption of two separated carbon atoms. The formation energy of a C_2 dimer, when the dimer is formed by adding a carbon atom to $Fe_{13}C$, is estimated as the decay energy of the lowest total energy state of $Fe_{13}C_2$ (see Fig. 46) to $Fe_{13}C + C$. The value of 7.14 eV obtained in this way can be compared to the value of 6.50 eV for
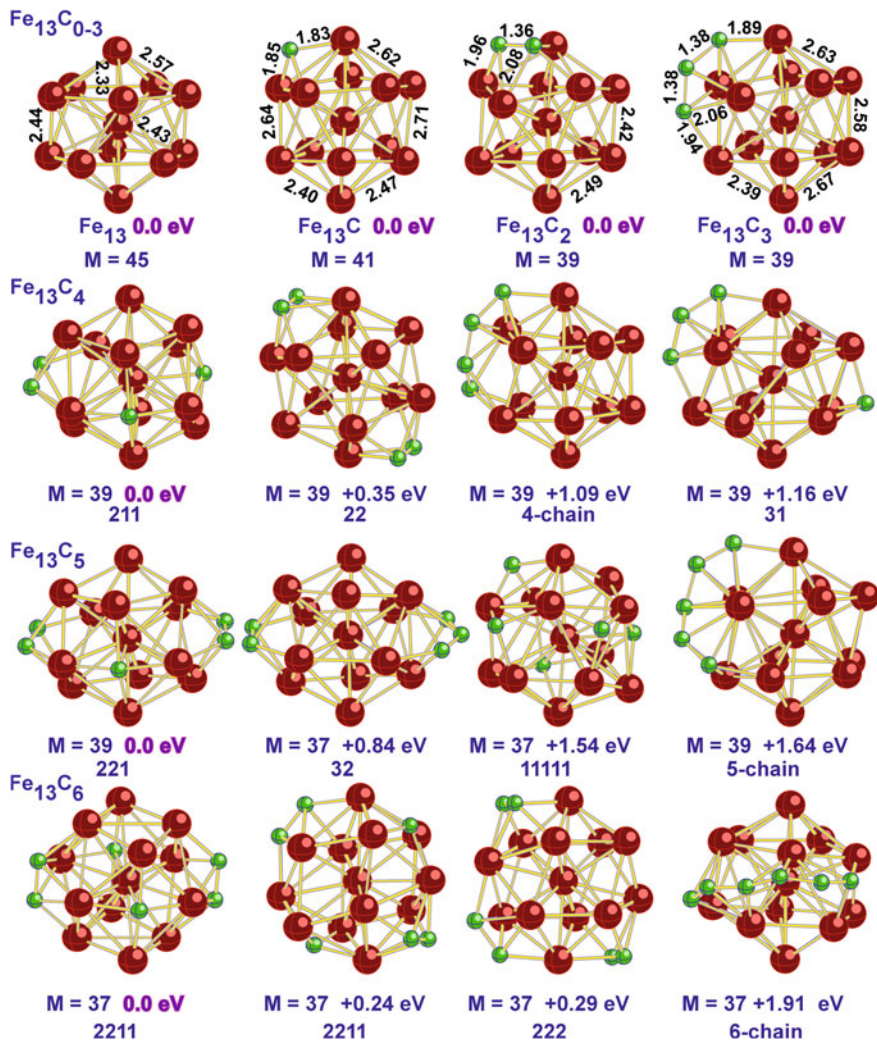
Fig. 46 Geometrical configurations corresponding to the lowest total energy and selected excited states of $Fe_{13}C_n$ for $n = 0$–6. M denotes the multiplicity $2S + 1$, bond lengths are in Å. The notation "$n_i n_j \ldots$" denotes the carbon chemisorption pattern, which corresponds to the separated carbon groups with n_i, n_j, … connected carbon atoms

the gas phase $C_2 \rightarrow 2C$ dissociation. Note that our computed energy for a single C atom attachment to a bare Fe_{13} cluster is 6.68 eV. The dissociation energy for the $Fe_{13}C_2 \rightarrow C_2$ channel is 7.32 eV, thus making the formation energy of a C_2 dimer on the iron cluster to be 14.46 eV compared to $\sim 2 * 6.68$ eV = 13.36 eV for the separate attachment of 2 carbon atoms. The latter value is smaller by 0.07 eV than the difference of 1.17 eV in total energies of the $Fe_{13}C_2$ ground and $Fe_{13}C_2$ (11) isomer

states; that is, there is almost no interaction between 2 carbon atoms placed on the cluster surface opposite to each other.

Assuming that the chemisorption energy of a single carbon atom in the lowest total energy state of $Fe_{13}C_4$ (211) is the same as in $Fe_{13}C$, i.e., 6.68 eV, one can estimate the fragmentation energy for $Fe_{13}C_4$ (211) $\rightarrow$ $Fe_{13}C_2$ (2) + 2C as $\sim$13.36 eV while the fragmentation energy for $Fe_{13}C_4$ (4) $\rightarrow$ $Fe_{13}C_2$ (2) + 2C is 12.43 eV. The smaller energy value in the second case can be related to a weaker bonding of the C_4 chain since the C–C and Fe–C bonding energies are quite similar.

Geometrical structures of the selected states of $Fe_{13}C_n$ with n ranging from 7 to 14 are shown in Figs. 47 and 48. When increasing the number of carbon atoms to 12, one observes the formation of an octahedron composed of C_2, with Fe_{13} being endohedral.

As may be seen in Figs. 46, 47, 48, the difference between total energies of the lowest total energy states and the states of isomers of $Fe_{13}C_n$ containing carbon chains grows as n increases. The "322221" isomer state of $Fe_{13}C_{12}$, (see Fig. 48) is close in total energy to the lowest energy "222222" state. This implies that the next structural pattern would be the formation of carbon trimers up to an octahedron composed of the trimers at $n = 18$. Indeed, our search confirmed that the most energetically preferable geometry trend is the gradual formation of carbon trimers (by adding carbon atoms to the dimers of the ground-state $Fe_{13}C_{12}$ cluster).

For $Fe_{13}C_{16}$, we have also optimized a structure composed of two C_8 placed on Fe_{13} one over another (see Fig. 49). As may be seen seen, the top eight carbon atoms retain the 8-member ring shape, whereas adding one more atom transforms this carbon structure to a cap containing hexagons and pentagons. However, adding two atoms conserves the top 8-member ring in the "CNT" isomer of $Fe_{13}C_{18}$ (see Fig. 50). Note, that the state whose geometry is presented by the carbon ring encircling the Fe_{13} cluster is higher in total energy by 4.97 eV than the lowest energy state, whereas the state with the geometry of a chain broken into two pieces "8-10" is higher by 4.67 eV. This means that the energy gain due to formation of a C–C bond in the ring exceeds the sum of the binding energies of four end atoms of the 8-member and 10-member carbon chains by 0.3 eV.

The state of a $Fe_{13}C_{18}$ isomer with a "433332" carbon pattern is higher in total energy than the "333333" state by only 0.04 eV (see Fig. 50), which assumes that carbon tetramers could continue the series of "six dimers" and "six trimers". However, only $Fe_{13}C_{19}$ follows this assumption. The lowest energy state found (see Fig. 51) for $Fe_{13}C_{20}$ using initial random distributions of carbon atoms has a "53332211" type, i.e., it contains a carbon pentamer, three carbon tetramers, three carbon dimers, and two single carbon atoms. The state whose geometry contains two carbon tetramers is higher in total energy by 0.42 eV, the state whose geometry is presented by a 20-member carbon ring wrapped around the iron cluster is higher by 1.65 eV, and the state whose geometry contains a C_{20} bowl is higher by 2.62 eV. Note that the iron particle geometry in the lowest energy state of $Fe_{13}C_{20}$ is strongly distorted, whereas it is not so for higher energy isomers.
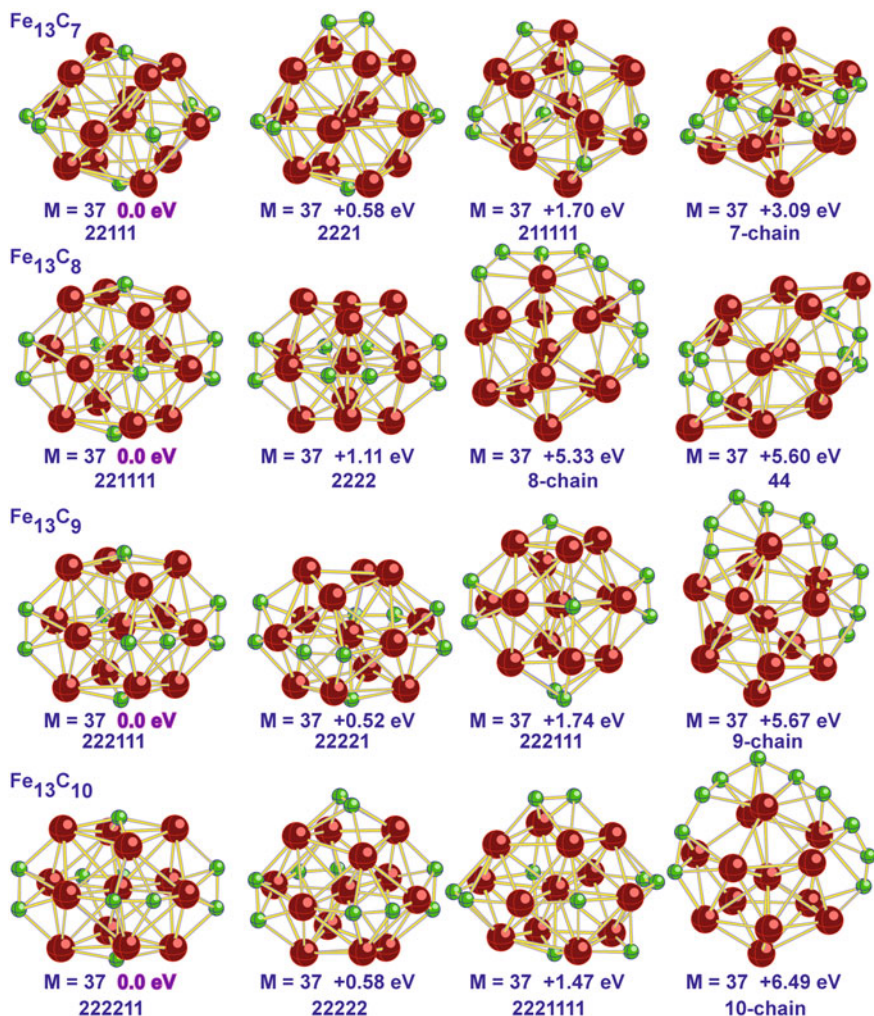
Fig. 47 Geometrical configurations corresponding to the lowest total energy and selected excited states of $Fe_{13}C_n$ for $n = 7$–10. "n-chain" denotes a chain consisting of n connected carbon atoms

Spin Dependence

In order to gain insight into how carbon chemisorption is related to the spin multiplicity, we performed optimizations of the Fe_{13} and $Fe_{13}C_8$ clusters in the range of spin multiplicities $2S + 1$ from 1 to 47. The relative total energies ΔE_{tot} computed with respect to the total energies of the corresponding lowest energy states are presented in Fig. 52.

For clarity, the curves for $0 \leq (2S + 1) \leq 23$ are presented in the lower panel and $24 \leq (2S + 1) \leq 47$ in the upper panel. As may be seen, the minimum energy for the Fe_{13} cluster occurs for $2S + 1 = 45$, while the minimum for $Fe_{13}C_8$ is at $2S + 1 = 37$.
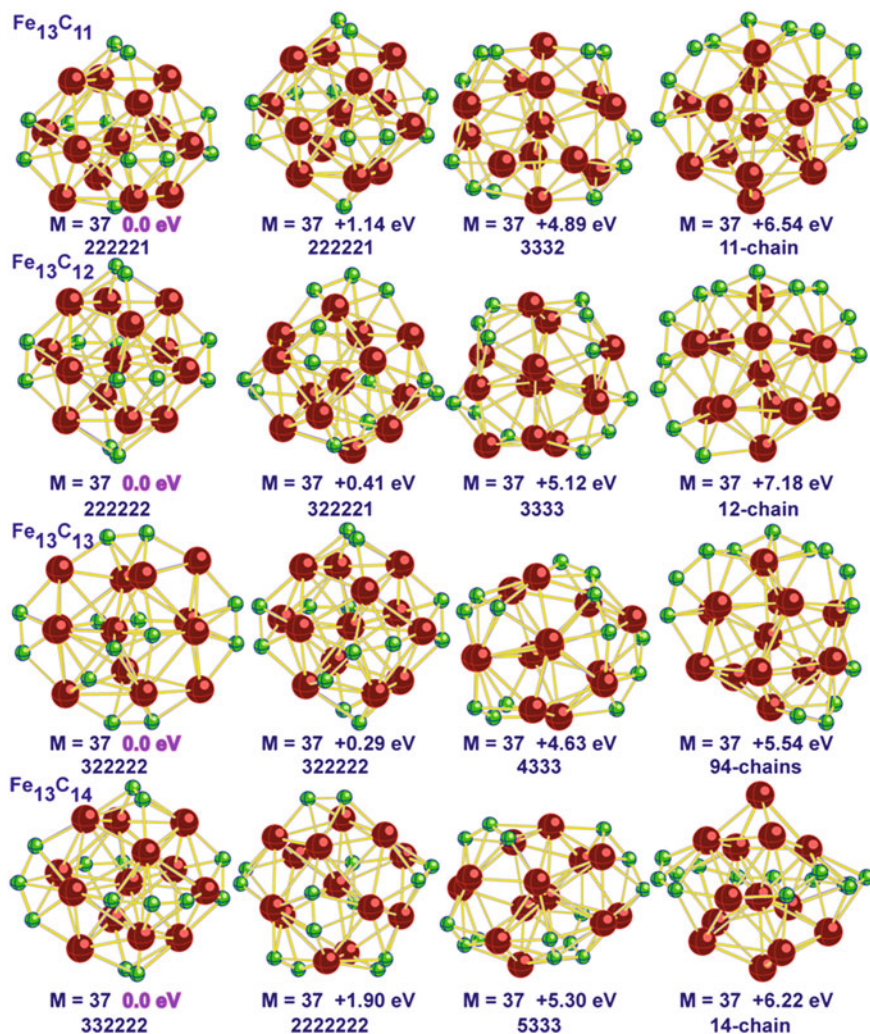
Fig. 48 Geometrical configurations corresponding to the lowest total energy and selected excited states of $Fe_{13}C_n$ for $n = 11–14$

As one moves down in spin multiplicities, there is a rather fast rise in ΔE_{tot} when moving to $2S + 1 = 33$ for both cases. Both series show small oscillations around the value of 1.5 eV for smaller spin multiplicities. The largest ΔE_{tot} values correspond to $2S + 1 = 25$ and 19 for both Fe_{13} and $Fe_{13}C_8$, which are the spin multiplicities at which the local magnetic moment of one iron atom flips. In terms of the excess spin density at this atom, it means that the populations of the spin-down and spin-up atomic orbitals are reversed. The average electronic configuration of a Fe atom in Fe_{13}, except for the central atom with $3d^{8.0}4s^{1.0}$, is $3d^{6.8}4s^{0.8}$ and corresponds to a practically inert $3d^{4.9}$ subshell and a valence $4s^{0.4}$ component in
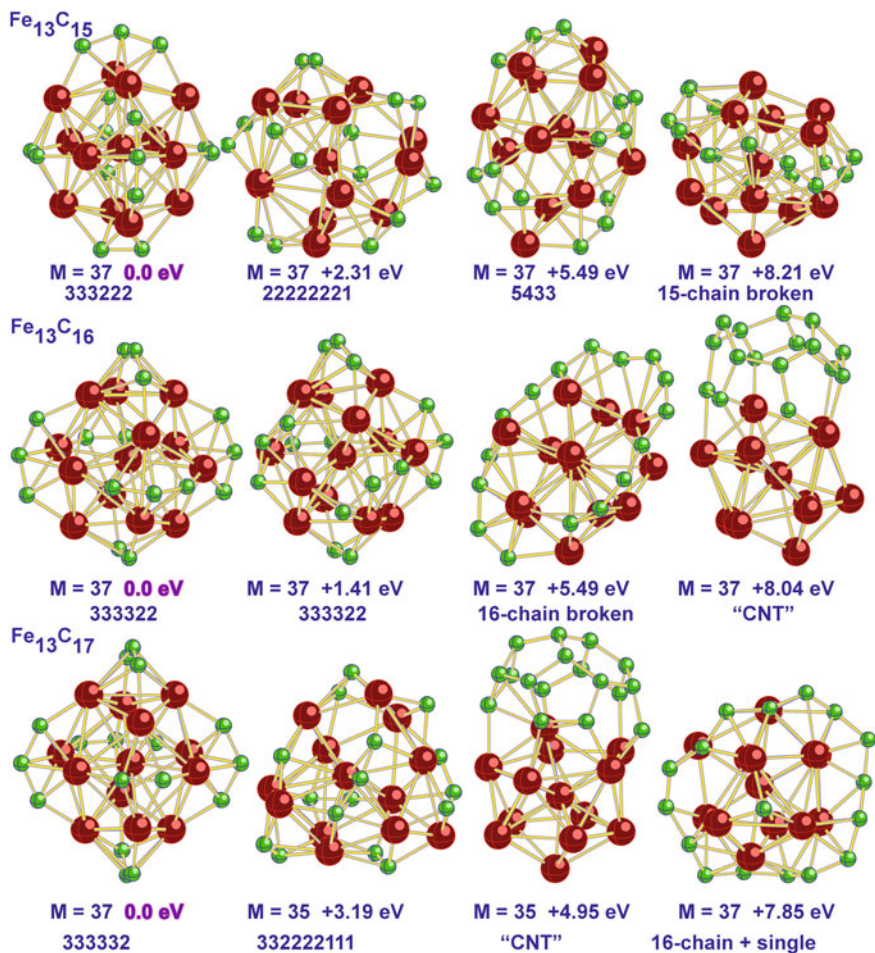
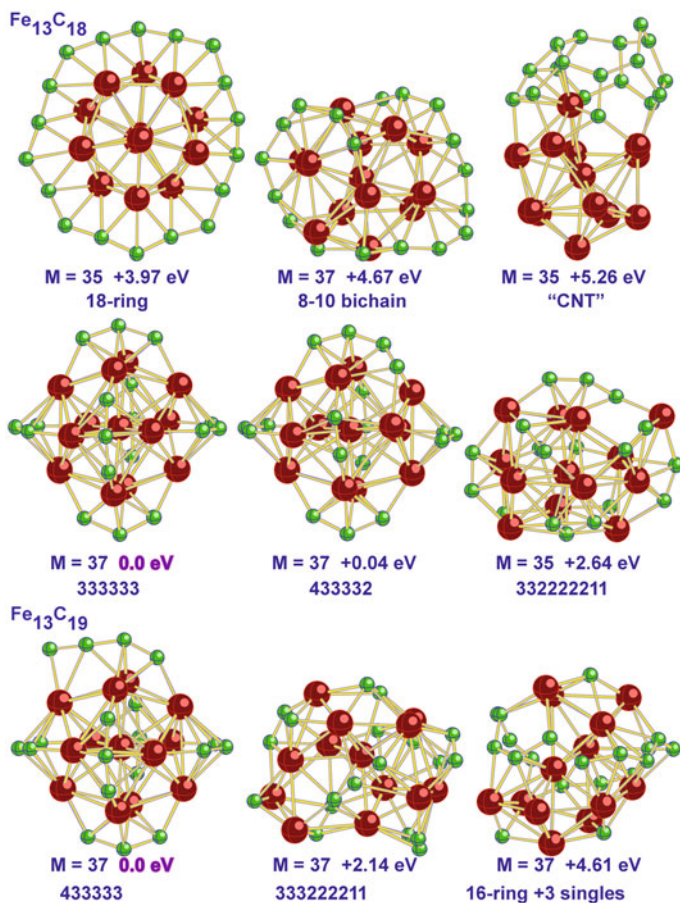**Fig. 49** Geometrical configurations corresponding to the lowest total energy and selected excited states of $Fe_{13}C_n$ for $n = 12$–17. "CNT" denotes a structure resembling the cap of a SWCNT

one spin representation and the valence $3d^{1.8}4s^{0.4}$ population in the second spin representation. The corresponding excess spin density is 3.1 e.

The flipping of local spin magnetic moments leads to the change in the valence interactions and to a higher total energy of the corresponding cluster state. Other flipping points also show a small increase in total energy with respect to their neighbors, but to a lesser extent than in the $2S + 1 = 25$ and 19 cases. As one moves to higher spin multiplicities from the respective minima of Fe_{13} and $Fe_{13}C_8$, ΔE_{tot} grows rapidly in the both series. Since the ΔE_{tot} behavior is nearly the same as in the Fe_{13} and $Fe_{13}C_8$ series, one can conclude that the binding capability of Fe_{13} does not nearly depend on the spin multiplicity when $2S + 1 < 35$.

Fig. 50 Geometrical configurations corresponding to the lowest total energy and selected excited states of $Fe_{13}C_{18}$ and $Fe_{13}C_{19}$

In order to gain insight on the nature of the total magnetic moment quenching due to carbon chemisorption, we analyze changes in the Fe NAO populations due to the chemisorption. In the ground state of Fe_{13}, the effective electronic configuration of an outer Fe atom is $3d^{6.84}4s^{0.98} = [3d^{4.96}4s^{0.69}]\alpha\ [3d^{1.89}4s^{0.30}]\beta$ and the central atom has an effective electronic configuration of $[3d^{4.93}4s^{0.44}]\alpha\ [3d^{2.68}4s^{0.47}]\beta$. That is, the α $3d$-subshell is chemically inert and the bonding is due to the $4s$ and $3d\beta$ electrons which corresponds to the valence of a Fe atom of ~ 3. The effective electronic configurations of carbon atoms correspond to an sp^3-hybridization of the valence AOs with the total charge transfer of $\sim 2.5\ e$ from iron atoms. Since the $4s$-population of iron atoms in the bare Fe_{13} cluster is $\sim 1\ e$, the effective electronic configurations of iron atoms in $Fe_{13}C_8$ correspond to a transfer of $\sim 0.3\ e$ to the carbon atoms and the promotion of $\sim 0.4\ e$ into the Fe $4p$-states. The
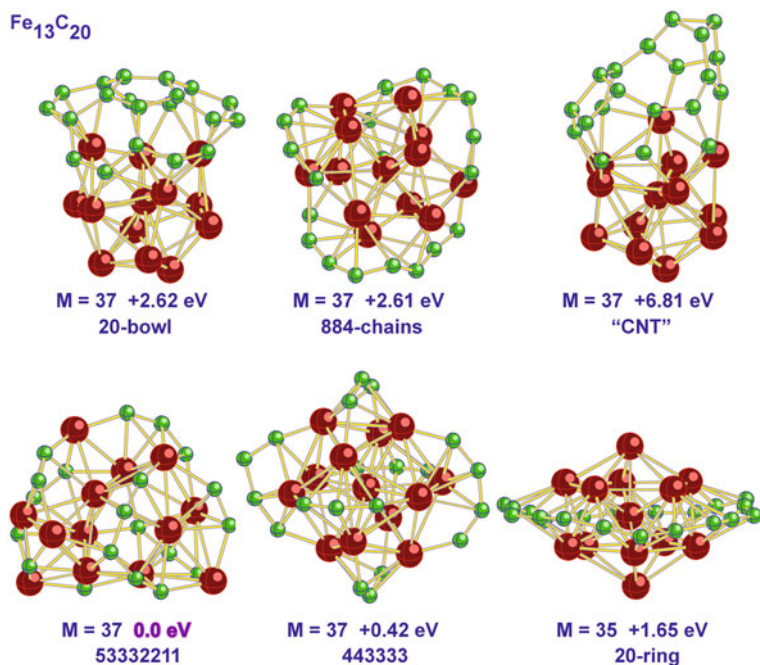
Fig. 51 Isomers of $Fe_{13}C_{20}$

Fig. 52 The relative energies of Fe_{13} and $Fe_{13}C_8$ (2222) as functions of the spin multiplicity. The number in the front of the *arrow* sets correspond to the number of the spin-down local magnetic moments on iron atoms at the given spin multiplicity
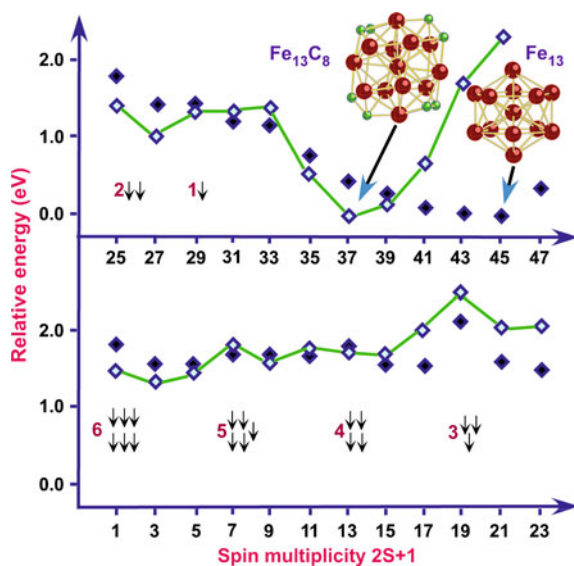
populations of the Fe $4s$ and $4p$ NAOs in the α- and β-spin representations are nearly the same, which means that the total magnetic moment of the cluster is defined by the sum of the differences between $3d\alpha$ and $3d\beta$ populations. The average difference is ∼2.7 e, which results in the total magnetic moment of ∼13 × 2.7 μ_B = 35 μ_B and the corresponding state has the spin multiplicity of 35 or 37. Note also that the $3d\alpha$ populations of iron atoms are somewhat smaller than the $3d\alpha$ populations in the bare Fe_{13} cluster, which means that this shell participates in the bonding. Depletion of the Fe $4s$ electrons and the decrease in the Fe $3d\alpha$ population by approximately the same amount as in the $Fe_{13}C_8$ isomers is typical for other $Fe_{13}C_n$ clusters which explains why their lowest total energy states possess the same spin multiplicity of 37 or, occasionally, 35.

Spin contamination was found to be rather small in ferromagnetic states of FeO_n (see Sect. 3), whereas it was found to be large in antiferromagnetic low-spin states. The same trend is observed for the Fe_{13} and $Fe_{13}C_8$ clusters. The computed $<S^2>$ value of the Fe_{13} ground state is 506.334, while the projected value is 506.004, and the exact $S(S+1)$ value is 506. That is, the spin contamination is only 0.07 %. The spin contamination does not increase substantially due to carbon chemisorption. The computed $<S^2>$ value of the $Fe_{13}C_8$ lowest total energy state with $2S+1 = 37$ is 342.478, while the projected value is 342.012, and the exact value is 342, i.e., the corresponding spin contamination is 0.14 %. In the antiferromagnetic states of Fe_{13} and $Fe_{13}C_8$, the spin contamination is substantially higher.

Thermodynamic Properties

In order to estimate the thermodynamic stability of $Fe_{13}C_n$, the energies of decay through various channels have been computed according to Eqs. (17) and (18):

$$E_{diss} = E^{el}_{tot}(A) + E_0(A) - \Sigma_i \left[E^{el}_{tot}(B_i) + E_0(B_i) \right] \qquad (17)$$

where $A = C_n$ ($n = 2–20$) or $Fe_{13}C_n$ ($n = 1–10$) and E_0 stands for the harmonic zero vibrational point energies. Since frequency calculations for larger n proved to be impractical, the difference of electronic total energies was used for $Fe_{13}C_n$ with $n = 11–20$:

$$E_{diss} = E^{el}_{tot}(A) - \Sigma_i E^{el}_{tot}(B_i) \qquad (18)$$

We consider first the energetics of a single carbon atom abstraction from the ground states of C_n and $Fe_{13}C_n$ and the full carbon stripping off a $Fe_{13}C_n$ cluster [the channel $Fe_{13}C_n \rightarrow Fe_{13} + C_n$ (g. s.)]. As follows from Fig. 53, the $C_n \rightarrow C_{n-1} + C$ abstraction energy curve as a function of n possesses a saw-tooth shape with the prominent peaks at $n = 10$, 14, and 18.

These n values correspond to the most stable cumulene structures defined by the relationship $n = 4k + 2$ [50]. The $Fe_{13}C_n \rightarrow Fe_{13}C_{n-1} + C$ energies show slow variations around 7 eV and decrease to 6 eV at $n = 18–20$. The $C_n \rightarrow C_{n-1} + C$ energies possess much larger fluctuations: from 8.4 eV at $n = 18$ to 5.4 eV at $n = 19$ and 6.5 eV at $n = 20$. The $Fe_{13}C_n \rightarrow Fe_{13} + C_n$ decay energies exceed 9 eV for
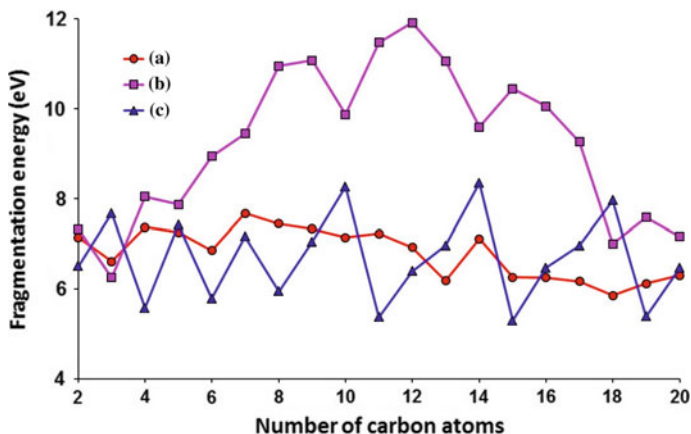
Fig. 53 Fragmentation energies through the channels: (*a*) $Fe_{13}C_n \rightarrow Fe_{13}C_n + C$; (*b*) $Fe_{13}C_n \rightarrow Fe_{13} + C_n$; (*c*) $C_n \rightarrow C_{n-1} + C$

$n = 7–17$ and drop to ~ 7 eV at $n = 20$. The absolute maximum of 11.9 eV corresponds to $n = 12$ which is in line with the experimental observation [51] of the prominent features of $Fe_nO_m^+$ species when the stoichiometric ratio is close to 1:1.

Figure 54 presents the energies of partial removal of carbon from $Fe_{13}C_n$ according to the decay channels $Fe_{13}C_n \rightarrow Fe_{13}C_{n-k} + C_k$, $k = 2–7$, where the corresponding species are in the lowest energy states. As may be seen, curve (b) corresponding to the abstraction of a C_3 trimer is below all other curves for n up to $n = 18$. This curve is closely followed by curve (a), which corresponds to
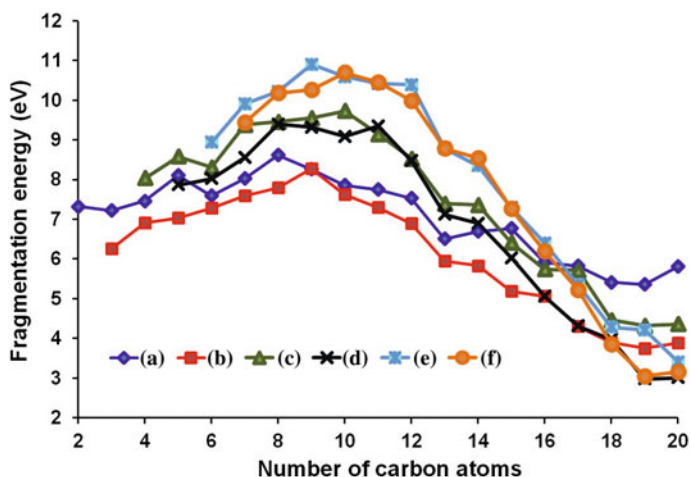
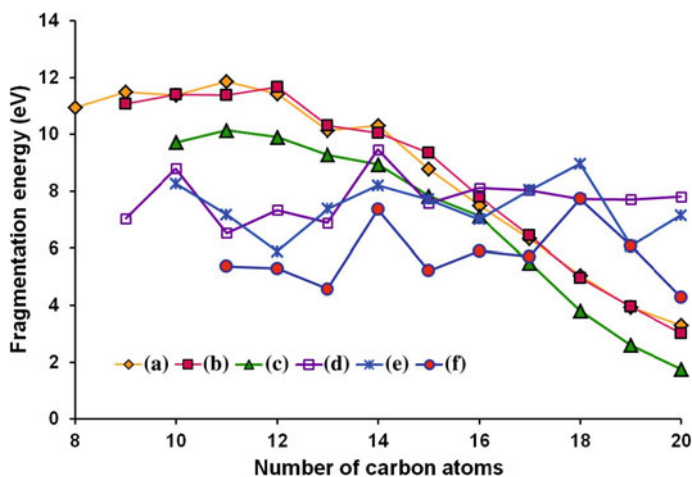**Fig. 54** Fragmentation energies of $Fe_{13}C_n \rightarrow Fe_{13}C_{n-k} + C_k$: (*a*) $k = 2$; (*b*) $k = 3$; (*c*) $k = 4$; (*d*) $k = 5$; (*e*) $k = 6$; (*f*) $k = 7$

abstraction of a C_2 dimer, by $n = 15$. All curves show a similar behavior: they possess maximal values at $n = 8\text{--}12$ and approach the values between 3.2 and 4.4 eV at $n = 20$, except for the $Fe_{13}C_n \rightarrow Fe_{13}C_{n-2} + C_2$ channel, where the n = 20 value is 5.81 eV.

Comparison of fragmentation energies for the $Fe_{13}C_n \rightarrow Fe_{13}C_{n-k} + C_k$ and $C_n \rightarrow C_{n-k} + C_k$ channels for $k = 8\text{--}10$ is presented in Fig. 55. As is seen, the behavior of the $Fe_{13}C_n$ decay curves is similar to that in Fig. 54. The curve maxima are shifted to larger n and the smallest energy of 1.76 eV is observed for the $Fe_{13}C_{20} \rightarrow Fe_{13}C_{10} + C_{10}$ channel. The $C_n \rightarrow C_{n-k} + C_k$ curves possess spikes at the cumulene values of n and they have no monotonic decrease at larger n.

The smallest value of 4.29 eV in the C_n decay series belongs to the $C_{20} \rightarrow C_{10} + C_{10}$ channel, which is to be related with the high stability of C_{10} possessing a cumulene structure. The same is true for the $Fe_{13}C_{20} \rightarrow Fe_{13}C_{10} + C_{10}$ channel. The energy decrease in the $Fe_{13}C_n \rightarrow Fe_{13}C_{n-k} + C_k$ channels is related to the decreasing stability of $Fe_{13}C_n$ at larger n. The behavior of dissociation energies for $n > 10$ is rather similar for all $Fe_{13}C_n \rightarrow Fe_{13}C_{n-k} + C_k$ channels. As is seen from Fig. 56, the energies decrease nearly monotonically as n increases. At $n = 20$, the smallest dissociation energy of 3.42 eV belongs to the $Fe_{13}C_{20} \rightarrow Fe_{13}C_9 + C_{11}$ channel and the largest dissociation energy of 7.16 eV belongs to the channel $Fe_{13}C_{20} \rightarrow Fe_{13} + C_{20}$.

Now we compare atomization energies of the carbon species chemisorbed on Fe_{13} in the lowest total energy states of $Fe_{13}C_n$ with atomization energies of the ground-state C_n species in order to gain insight in the carbon binding capability of Fe_{13} for $n = 1\text{--}20$. These atomization energies are displayed in Table 18 where the second column presents the content of carbon chemisorbed on Fe_{13}, and the third column shows the corresponding fragmentation channels. Column **4** presents the

Fig. 55 Fragmentation energies of $Fe_{13}C_n \rightarrow Fe_{13}C_{n-k} + C_k$: (*a*) $k = 8$; (*b*) $k = 9$; (*c*) $k = 10$; and fragmentation energies of $C_n \rightarrow C_{n-k} + C_k$: (*d*) $k = 8$; (*e*) $k = 9$; (*f*) $k = 10$
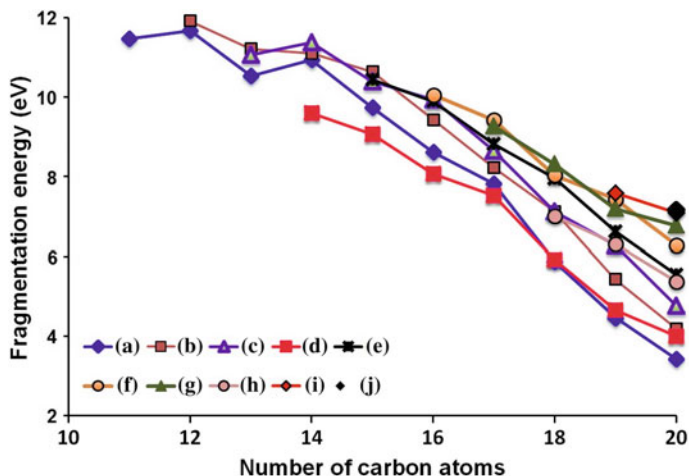
Fig. 56 Fragmentation energies of $Fe_{13}C_n \rightarrow Fe_{13}C_{n-k} + C_k$: (*a*) $k = 11$; (*b*) $k = 12$; (*c*) $k = 13$; (*d*) $k = 14$; (*e*) $k = 15$; (*f*) $k = 16$; (*g*) $k = 17$; (*h*) $k = 18$; (*i*) $k = 19$; (*j*) $k = 19$

fragmentation energies D_0 or D_e, i.e., computed with taking into account the $Fe_{13}C_n$ ZPVEs for $n \leq 10$ (D_0) and without the ZPVEs for larger n (D_e). The ZPVE contribution is expected to be around 0.15 eV.

The next column presents atomization energies of carbon species in the right-hand side of the fragmentation channels in column **3** and column **6** contains the sum of fragmentation and atomization energies from columns **4** and **5**. Column **7** presents the atomization energies of the gas-phase C_n species.

As may be seen, the binding energy of carbon species to Fe_{13} reaches a local maximum at $n = 12$ and decreases at larger n except for $Fe_{13}C_{20}$. The sum $\Delta E_{tot}(Fe_{13}C_n \rightarrow Fe_{13} + \sum C_i) + \Delta E_{tot}(\sum C_i \rightarrow nC)$ values presented in column **6** have to be compared to the $\Delta E_{tot}(C_n \rightarrow nC)$ atomization energies given in column **7**. Comparison shows that atomization energies of carbon chemisorbed on Fe_{13} are larger by approximately 10 eV, which can be related to the catalytic strength of this particle. Two bottom lines of the table show the data computed for 2 isomers of $Fe_{13}C_{20}$, which are nearly degenerate in total energy. The energy of the $Fe_{13}C_{20} \rightarrow Fe_{13} + C_5 + 3C_3 + 2C_2 + 2C$ fragmentation channel is larger than that of the $Fe_{13}C_{20} \rightarrow Fe_{13} + 2C_4 + 4C_3$ channel by +13.65 eV which is nearly the same as the difference in the corresponding carbon atomization energies taken with the opposite sign. This causes the total atomization energies in column **6** to practically match each other. That is, there is a competition for a carbon atom between binding to the iron particle with or without the formation of a C–C bond at low carbon coverage. When the binding capability of the catalyst surface is exhausted, further adding of carbon atoms should likely lead to the formation of such carbon structures whose atomization energies are the largest possible ones. Our energy estimates from Table 18 can be used for obtaining parameters in different models of the CNT growth on iron catalysts.

Table 18 Carbon atomization energies for the lowest total energy states of $Fe_{13}C_n$ and C_n^a

n	Carbon pattern	Channel	Channel D_0/D_e	Carbon atomization energies		
				Product C_i	Total	C_n^b
1	**2**	**3**	**4**	**5**	**6**	**7**
1	1	$Fe_{13}C \rightarrow Fe_{13} + C$	6.68	…	6.68	…
2	2	$Fe_{13}C_2 \rightarrow Fe_{13} + C_2$	7.32	6.50	13.82	6.50
3	3	$Fe_{13}C_3 \rightarrow Fe_{13} + C_3$	6.25	14.17	20.42	14.17
4	211	$Fe_{13}C_4 \rightarrow Fe_{13} + C_2 + 2C$	21.28	6.50	27.78	19.74
5	221	$Fe_{13}C_5 \rightarrow Fe_{13} + 2C_2 + C$	22.02	13.00	35.02	27.16
6	2211	$Fe_{13}C_6 \rightarrow Fe_{13} + 2C_2 + 2C$	28.88	13.00	41.88	32.94
7	22111	$Fe_{13}C_7 \rightarrow Fe_{13} + 2C_2 + 3C$	36.55	13.00	49.55	40.10
8	221111	$Fe_{13}C_8 \rightarrow Fe_{13} + 2C_2 + 4C$	43.99	13.00	56.99	46.03
9	222111	$Fe_{13}C_9 \rightarrow Fe_{13} + 3C_2 + 3C$	44.42	19.51	63.92	53.07
10	222211	$Fe_{13}C_{10} \rightarrow Fe_{13} + 4C_2 + 2C$	45.21	26.01	71.21	61.33
11	222221	$Fe_{13}C_{11} \rightarrow Fe_{13} + 5C_2 + C$	46.54	32.51	79.04	66.74
12	222222	$Fe_{13}C_{12} \rightarrow Fe_{13} + 6C_2$	46.85	39.01	85.86	73.13
13	322222	$Fe_{13}C_{13} \rightarrow Fe_{13} + C_3 + 5C_2$	45.26	46.67	91.93	80.09
14	332222	$Fe_{13}C_{14} \rightarrow Fe_{13} + 2C_3 + 4C_2$	44.49	54.34	98.83	88.43
15	333222	$Fe_{13}C_{15} \rightarrow Fe_{13} + 3C_3 + 3C_2$	43.08	62.02	105.10	93.71
16	333322	$Fe_{13}C_{16} \rightarrow Fe_{13} + 4C_3 + 2C_2$	41.55	69.69	111.24	100.17
17	333332	$Fe_{13}C_{17} \rightarrow Fe_{13} + 5C_3 + C_2$	39.94	77.36	117.30	107.13
18	333333	$Fe_{13}C_{18} \rightarrow Fe_{13} + 6C_3$	38.01	85.03	123.04	115.10
19	433333	$Fe_{13}C_{19} \rightarrow Fe_{13} + C_4 + 5C_3$	38.44	90.60	129.04	120.48
20	443333	$Fe_{13}C_{20} \rightarrow Fe_{13} + 2C_4 + 4C_3$	39.05	97.65	136.70	126.95

[a]All energy values are in eV. The ZPVEs are accounted for up to $n = 10$ for $Fe_{13}C_n$

[b]The $C_n \rightarrow nC$ energies. Bold numbers **1, 2, 3 … 7** in the head are given for the reference purpose

12 Summary

Iron nanoparticles and their interactions with different environmental agents remain a hot topic of both experimental and theoretical studies. One of the major difficulties in the technological application of iron particles is ensuring their protection from oxidation while also preserving their highly magnetic properties. It is, however, difficult to find substances which do not weaken the magnetic properties of iron particles and which do not destroy the particle's integrity. For example, the coating of iron particles with gold or silica causes the weakening of the total magnetic moments of the coated nanoparticles, whereas magnesium coatings lead to segregation of magnesium and iron particles. Chemisorption of oxygen by iron particles decreases the total spin magnetic moment of the particles; therefore, oxide coatings are to be expected to generally reduce the total magnetic moments of the particles. On the contrary, carbon chemisorption does not result in a substantial quenching of

the total spin magnetic moments of iron clusters, but under some conditions and sizes of iron nanoparticles, the formation of iron carbide FeC_x could be expected. Coating iron particles with semiconductor materials can bring materials suitable for fabrication of optomagnetic sensors since changes in the total magnetic moment would influence the wavelengths of emitted light photons. Fe clusters are promising for the fabrication of new permanent nanomagnets in addition to the Fe-Nb-B permanent magnet invented in 1984 which possess a high coercivity. Iron nanoparticles are used in biomedical applications, where they help laboratory diagnostics and drug delivery. The iron-containing nanoparticles can also be used as contrast agents and for tumor therapy.

References

1. I.M.L. Billas, A. Châtelain, W.A. de Heer, Magnetism from the atom to the bulk in iron, cobalt, and nickel clusters. Science **265**, 1682–1684 (1994)
2. X. Xu, S. Yin, R. Moro, A. Liang, J. Bowlan, W.A. de Heer, Metastability of free cobalt and iron clusters: a possible precursor to bulk ferromagnetism. Phys. Rev. Lett. **107**, 057203 (2011)
3. M. Niemeyer, K. Hirsch, V. Zamudio-Bayer, A. Langenberg, M. Vogel, M. Kossick, C. Ebrecht, K. Egashira, A. Terasaki, T. Möller, B.V. Issendorff, J.T. Lau, Spin coupling and orbital angular momentum quenching in free iron clusters. Phys. Rev. Lett. **108**, 057201 (2012)
4. T. Oda, A. Pasquarello, R. Car, Fully unconstrained approach to noncollinear magnetism: application to small Fe clusters. Phys. Rev. Lett. **80**, 3622–3625 (1998)
5. D. Hobbs, G. Kresse, J. Hafner, Fully unconstrained noncollinear magnetism within the projector augmented-wave method. Phys. Rev. B **62**, 11556–11570 (2000)
6. D.R. Roy, R. Robles, S.N. Khanna, Magnetic moment and local moment alignment in anionic and/or oxidized Fen clusters. J. Chem. Phys. **132**, 194305 (2010)
7. G. Rollmann, P. Entel, S. Sahoo, Competing structural and magnetic effects in small iron clusters. Comput. Mater. Sci. **35**, 275–278 (2006)
8. B.H. Weiller, P.S. Bechthold, E.K. Parks, L.G. Pobo, S.J. Riley, The reactions of iron clusters with water. J. Chem. Phys. **91**, 4714–4727 (1989)
9. A.E. Reed, L.A. Curtiss, F. Weinhold, Intermolecular interactions from a natural bond orbital, donor-acceptor viewpoint. Chem. Rev. **88**, 899–926 (1988)
10. G.L. Gutsev, C.W. Bauschlicher Jr, Chemical bonding, electron affinity, and ionization energies of the homonuclear 3d-metal dimers. J. Phys. Chem. A **107**, 4755–4767 (2003)
11. G.L. Gutsev, C.W. Bauschlicher Jr, Electron affinities, ionization energies, and fragmentation energies of Fe_n clusters ($n = 2$–6): a density functional theory study. J. Phys. Chem. A **107**, 7013–7023 (2003)
12. S. Berski, G.L. Gutsev, M. Mochena, J. Andrés, Toward understanding the electron density distribution in magnetic clusters. Insight from the ELF and AIM analyses of ground-state Fe_4. J. Phys. Chem. A **108**, 6025 (2004)
13. G.L. Gutsev, S.N. Khanna, B.K. Rao, P. Jena, Electronic structure and properties of FeO_n and FeO_n^- clusters. J. Phys. Chem. **103**, 5812–5822 (1999)
14. G.L. Gutsev, S.N. Khanna, B.K. Rao, P. Jena, FeO_4: a unique example of a closed-shell cluster mimicking a superhalogen. Phys. Rev. A **59**, 3681–3684 (1999)
15. G.L. Gutsev, C.W. Bauschlicher Jr, L. Andrews, 3d-metal monocarbonyls MCO, MCO^+, and MCO^- (M = Sc to Cu): comparative bond strengths and catalytic ability to produce CO_2 in reactions with CO. Chem. Phys. **290**, 47–58 (2003)

16. G.L. Gutsev, C.A. Weatherford, K. Pradhan, P. Jena, Structure and spectroscopic properties of iron oxides with the high content of oxygen: FeO_n and FeO_n^- ($n = 5–12$). J. Phys. Chem. A **114**, 9014–9021 (2010)

17. M. Velegrakis, C. Mihesan, M. Jadraque, Collision-induced dissociation studies on $Fe(O_2)_n^+$ (n = 1–6) clusters: application of a new technique based on crossed molecular beams. J. Phys. Chem. **117**, 2891–2898 (2013)

18. J.M. Wittbrodt, H.B. Schlegel, Some reasons not to use spin projected density functional theory. J. Chem. Phys. **105**, 6574–6577 (1996)

19. G.L. Gutsev, C.A. Weatherford, L.G. Gutsev, B.R. Ramachandran, Structure and properties of the Fluorine-Rich FeF_n^- anions. J. Comp. Chem. to be submitted

20. G.L. Gutsev, C.W. Bauschlicher Jr, Electron affinities, ionization energies, and fragmentation energies of Fe_n clusters ($n = 2–6$): a density functional theory study. J. Phys. Chem. A **107**, 7013–7023 (2003)

21. L.-S. Wang, H.-S. Cheng, J. Fan, Photoelectron spectroscopy of size-selected transition metal clusters: Fe_n^-, $n = 3–24$. J. Chem. Phys. **102**, 9480–9493 (1995)

22. E.A. Rohlfing, D.M. Cox, A. Kaldor, K.H. Johnson, Photoionization spectra and electronic structure of small iron clusters. J. Chem. Phys. **81**, 3846–3851 (1984)

23. G.L. Gutsev, C.W. Bauschlicher Jr, Interactions of carbon atoms with neutral and charged Fe_n clusters ($n = 2–6$). Chem. Phys. **291**, 27–40 (2003)

24. G.L. Gutsev, C.W. Bauschlicher Jr, L. Andrews, Similarities and differences in the structure of 3d-metal monocarbides and monoxides. Theor. Chem. Acc. **109**, 298–308 (2003)

25. G.L. Gutsev, C.W. Bauschlicher Jr, H.-J. Zhai, L.S. Wang, Structure of Fe_nO and Fe_nO^- clusters (n = 2–6) from photoelectron spectroscopy and density functional theory studies. J. Chem. Phys. **119**, 11135–11145 (2003)

26. G.L. Gutsev, M.D. Mochena, C.W. Bauschlicher Jr, Dissociative and associative attachment of OH to iron clusters. Chem. Phys. Lett. **407**, 180–185 (2005)

27. P. Nikolaev, M.J. Bronikowski, R.K. Bradley, F. Rohmund, D.T. Colbert, K.A. Smith, R.E. Smalley, Gas-phase catalytic growth of single-walled carbon nanotubes from carbon monoxide. Chem. Phys. Lett. **313**, 91–97 (1999)

28. G.L. Gutsev, C.W. Bauschlicher Jr, L. Andrews, Structure of neutral and charged Fe_nCO clusters ($n = 1–6$) and energetics of the $Fe_nCO + CO \rightarrow Fe_nC + CO_2$ reaction. J. Chem. Phys. **119**, 3681–3690 (2003)

29. F. Boccuzzi, A. Chiorino, FTIR study of CO oxidation on Au/TiO2 at 90 K and room temperature. An insight into the nature of the reaction centers. J. Phys. Chem. B **104**, 5414–5416 (2000)

30. G.L. Gutsev, C.W. Bauschlicher Jr, Oxidation of carbon monoxide on small iron clusters. Chem. Phys. Lett. **380**, 435–443 (2003)

31. G.L. Gutsev, C.A. Weatherford, P. Jena, E. Johnson, B.R. Ramachandran, Structure and properties of Fe_n, Fe_n^-, and Fe_n^+ clusters, $n = 7–20$. J. Phys. Chem. A **116**, 10218–10228 (2012)

32. O. Diéguez, M.M.G. Alemany, C. Rey, Pablo Ordejón, L.J. Gallego, Density-functional calculations of the structures, binding energies, and magnetic moments of Fe clusters with 2 to 17 atoms. Phys. Rev. B **63**, 205407 (2001)

33. C. Köhler, G. Seifert, T. Frauenheim, Density functional based calculations for Fe_n ($n \leq 32$). Chem. Phys. **309**, 23–31 (2005)

34. M. Sakurai, K. Watanabe, K. Sumiyama, K. Suzuki, Magic numbers in transition metal (Fe, Ti, Zr, Nb, and Ta) clusters observed by time-of-flight mass spectrometry. J. Chem. Phys. **111**, 235–238 (1999)

35. P. Bobadova-Parvanova, K.A. Jackson, S. Srinivas, M. Horoi, Density-functional investigations of the spin ordering in Fe_{13} clusters. Phys. Rev. B **66**, 195402 (2002)

36. Y. Sun, R. Fournier, M. Zhang, Structural and electronic properties of 13-atom 4d transition metal clusters. Phys. Rev. A **79**, 043202 (2009)

37. M.J. Piotrowski, P. Piquini, J.L.F. Da Silva, Density functional theory investigation of 3d, 4d, and 5d 13-atom metal clusters. Phys. Rev. B **81**, 155446 (2010)

38. G.L. Gutsev, L.E. Johnson, K.G. Belay, C.A. Weatherford, L.G. Gutsev, B.R. Ramachandran, Structure and magnetic properties of $Fe_{12}X$ clusters. Chem. Phys. **430**, 62–68 (2014)

39. G.L. Gutsev, C.A. Weatherford, K. Pradhan, P. Jena, Density functional study of neutral and anionic AlO_n and ScO_n with high oxygen content. J. Comp. Chem. **32**, 2974–2982 (2011)

40. C.X. Su, P.B. Armentrout, Collision induced dissociation of Fe_n^+ ($n = 2$–19) with Xe: bond energies, geometric structures, and dissociation pathways. J. Chem. Phys. **97**, 4072–4083 (1992)

41. P.B. Armentrout, Reactions and thermochemistry of small transition metal cluster ions. Annu. Rev. Phys. Chem. **52**, 423–461 (2001)

42. G.L. Gutsev, L.E. Johnson, K.G. Belay, C.A. Weatherford, L.G. Gutsev, B.R. Ramachandran, Structure and magnetic properties of Fe_nGd clusters, $n = 12$–19. Eur. Phys. J. D **68**, 81–90 (2014)

43. N.O. Jones, B.V. Reddy, F. Rasouli, S.N. Khanna, Structural growth in iron oxide clusters: rings, towers, and hollow drums. Phys. Rev. B **72**, 165411 (2005)

44. M. Ju, J. Lv, X.-Y. Kuang, L.-P. Ding, C. Lu, J.-J. Wang, Y.-Y. Jin, G. Maroulis, Systematic theoretical investigation of geometries, stabilities and magnetic properties of iron oxide clusters $(FeO)_n^\mu$ ($n = 1$–8, $\mu = 0, \pm 1$): insights and perspectives. RSC Adv. **5**, 6560–6570 (2015)

45. G.L. Gutsev, C.A. Weatherford, P. Jena, E. Johnson, B.R. Ramachandran, Competition between surface chemisorption and cage formation in $Fe_{12}O_{12}$ clusters. Chem. Phys. Lett. **556**, 211–216 (2013)

46. G.L. Gutsev, M.D. Mochena, C.W. Bauschlicher Jr, Structure and properties of Fe_4 with different coverage by C and CO. J. Phys. Chem. A **108**, 11409–11418 (2004)

47. G.L. Gutsev, M.D. Mochena, C.W. Bauschlicher Jr, All-electron DFT Modeling of SWCNT growth initiation by iron catalysts. Lect. Notes Comput. Sci. **3993**, 128–135 (2006)

48. G.L. Gutsev, Key role of antiferrimagnetic states in remagnetization of iron clusters. Phys. Rev. B **65**, 132417 (2002)

49. G.L. Gutsev, C.A. Weatherford, P. Jena, E. Johnson, B.R. Ramachandran, Structural patterns in carbon chemisorption on an icosahedral iron cluster. J. Phys. Chem. C **116**, 7050–7061 (2012)

50. R. Hoffman, Extended Hückel theory-V: cumulenes, polyenes, polyacetylenes and C_n. Tetrahedron **22**, 521–538 (1966)

51. K.S. Molek, C. Anfuso-Cleary, M.A. Duncan, Photodissociation of iron oxide cluster cations. J. Phys. Chem. A **112**, 9238–9247 (2008)